

A Discontinuous Galerkin Method for Diffusion Flames

Embedded in a low-Mach solver framework

Zur Erlangung des akademischen Grades Doktor-Ingenieur (Dr.-Ing.)

Vorgelegte Dissertation von Juan Francisco Gutiérrez Jorquera aus Santiago, Chile

Tag der Einreichung: 25. August 2022, Tag der Prüfung: 25. August 2022

Erstreferent: Prof. Dr.-Ing Martin Oberlack

Koreferent: Gutachter 2

Darmstadt



TECHNISCHE
UNIVERSITÄT
DARMSTADT

Fachbereich Maschinenbau
Fachgebiet für
Strömungsdynamik

A Discontinuous Galerkin Method for Diffusion Flames
Embedded in a low-Mach solver framework

Vorgelegte Dissertation von Juan Francisco Gutiérrez Jorquera

Erstreferent: Prof. Dr.-Ing Martin Oberlack
Koreferent: Gutachter 2

Tag der Einreichung: 25. August 2022
Tag der Prüfung: 25. August 2022

Darmstadt

Bitte zitieren Sie dieses Dokument als:
URN: urn:nbn:de:tuda-tuprints-1234
URL: <http://tuprints.ulb.tu-darmstadt.de/12345>
DOI: <https://doi.org/10.25534/tuprints-1234>

Dieses Dokument wird bereitgestellt von tuprints,
E-Publishing-Service der TU Darmstadt
<http://tuprints.ulb.tu-darmstadt.de>
tuprints@ulb.tu-darmstadt.de

Die Veröffentlichung steht unter folgender Creative Commons Lizenz:
Namensnennung 4.0 International
<https://creativecommons.org/licenses/by/4.0/>
This work is licensed under a Creative Commons License:
Attribution 4.0 International
<https://creativecommons.org/licenses/by/4.0/>

Dedication

Erklärungen laut Promotionsordnung

§8 Abs. 1 lit. c PromO

Ich versichere hiermit, dass die elektronische Version meiner Dissertation mit der schriftlichen Version übereinstimmt.

§8 Abs. 1 lit. d PromO

Ich versichere hiermit, dass zu einem vorherigen Zeitpunkt noch keine Promotion versucht wurde. In diesem Fall sind nähere Angaben über Zeitpunkt, Hochschule, Dissertationsthema und Ergebnis dieses Versuchs mitzuteilen.

§9 Abs. 1 PromO

Ich versichere hiermit, dass die vorliegende Dissertation selbstständig und nur unter Verwendung der angegebenen Quellen verfasst wurde.

§9 Abs. 2 PromO

Die Arbeit hat bisher noch nicht zu Prüfungszwecken gedient.

Darmstadt, 25. August 2022

J. Gutiérrez-Jorquera



Abstract

Abstract



Zusammenfassung

Zusammenfassung



Acknowledgements

Acknowledgements

Contents

List of Figures	xv
List of Tables	xvii
1 Introduction	1
1.1 Introduction and state of the art.	1
1.1.1 Combustion	1
2 Governing equations	5
2.1 The low-Mach number equations for reactive flows	5
2.1.1 The reactive Navier–Stokes equations	5
2.1.2 The unsteady non-dimensional low-Mach equations	9
2.2 The flame sheet approximation	12
2.3 Boundary conditions	14
3 Numerical methods	15
3.1 The Discontinuous Galerkin method	15
3.1.1 Spatial discretization	15
3.1.2 Discretization for a DG Method	16
3.1.3 Temporal discretization	21
3.2 Computational methodology	23
3.2.1 Dogleg Method	24
3.2.2 Termination criterion	26
3.2.3 Solver safeguard	26
3.2.4 Homotopy method	26
3.2.5 Initialization of combustion applications	28
4 Results	31
4.1 Single-component isothermal cases	31
4.1.1 Transpiring Channel?	31
4.1.2 Taylor-Green vortex	32
4.1.3 Backward-facing step	33
4.2 Single-component non-isothermal cases	34
4.2.1 Heated backward-facing step	34
4.2.2 Couette flow with vertical temperature gradient	37
4.2.3 Differentially heated cavity problem	41
4.2.4 Poiseuille–Rayleigh–Bénard instability in a channel	45
4.2.5 Flow around a heated cylinder	47
4.3 Multi-component non-isothermal cases	50
4.3.1 CoFlowing flame?	51

4.3.2 Counterflow diffusion flame	51
4.3.3 Chambered diffusion flame	54
4.4 Conclusions	55
5 Conclusion	59
Curriculum vitae	61

List of Figures

2.1	Temperature and fuel mass fraction profiles calculated in the center-line of a counter-flow flame configuration using finite chemistry (black) and the flame sheet approximation (green).	14
3.1	Behaviour of the homotopy method for the differentially heated cavity test case. The homotopy parameter h_p in this case is the Reynolds number.	27
3.2	Temperature profile calculated in the center-line of a counter-flow flame configuration for different smoothing parameters σ	29
4.1	Schematic representation of the backward-facing step. Both primary and secondary vortices are shown. Sketch is not to scale.	34
4.2	Structured mesh used in all calculations.	34
4.3	Detachment and reattachment lengths of the primary (left figure) and secondary (right figure) recirculation zones after the backward-facing step. Solid lines correspond to the results obtained with BoSSS and the marks to the reference solution (biswasBackwardFacingStepFlows2004).	35
4.4	Temperature profile (top) and streamlines (bottom) corresponding to the backward-facing Step configuration for $Re = 400$ and an expansion ratio of two.	36
4.5	Local friction factor and local Nusselt number along the bottom wall for $Re = 700$ and an expansion ratio of two. The solid lines corresponds to our solution and the marks to the reference henninkLowMachNumberFlow2022	36
4.6	bla	36
4.7	Schematic representation of the couette flow with temperature difference test case.	37
4.8	Convergence study of the differentially heated cavity problem for $Ra = 10^3$	39
4.9	Schematic representation of the differentially heated cavity problem.	41
4.10	Streamlines of the heated cavity configuration with $\epsilon = 0.6$	44
4.11	Profiles of the x-velocity component along the vertical line $x = 0.5$. Solid lines represents our solution and the marks the benchmark solution. vierendeelsBenchmarkSolutionsNatural2003	47
4.12	Profiles of the y-velocity component along the horizontal line $y = 0.5$. Solid lines represents our solution and marks the benchmark solution. vierendeelsBenchmarkSolutionsNatural2003	47
4.13	Temperature profiles for the differentially heated square cavity along different vertical levels. Solid lines represent our solution and marks the benchmark solution. vierendeelsBenchmarkSolutionsNatural2003	47
4.14	Nusselt numbers calculated with Equation (4.23) at the hot wall (Nu_h) and the cold wall (Nu_c) for different number of cells and polynomial order k . The reference values vierendeelsBenchmarkSolutionsNatural2003 are shown with dashed lines.	48
4.15	Convergence study of the differentially heated cavity problem for $Ra = 10^3$	49
4.16	Coflowing Flame.	52

4.17 Schematic representation of the counterflow configuration.	53
4.18 Convergence history of the diffusion flame in the counterflow configuration, with a maximum strain value of 165.1s^{-1}	54
4.19 Comparison of the axial velocity calculated with <i>BoSSS</i> and the one-dimensional approximation.	55
4.20 Comparison of temperature and mass fraction fields obtained with <i>BoSSS</i> and the one-dimensional approximation.	56
4.21 Calculated temperature and velocity fields (top picture) and reaction rate (sec- ond picture) of the counter diffusion flame configuration, case (a). The unit of the temperature is K and of the reaction rate $\text{kmol m}^{-3} \text{s}^{-1}$	57
4.22 Schematic representation of the chambered diffusion flame configuration. . .	57
4.23 Convergence study for the chambered diffusion flame configuration.	58
5.1 Schematic representation of the backward-facing step. Both primary and sec- ondary vortices are shown. Sketch is not to scale.	59



List of Tables

- 2.1 Base parameters used in the one-step combustion model by **fernandez-tarrazoSimpleOnestepChem**
- 4.1 Solution of the Couette flow with vertical temperature gradient. Viscosity and heat conductivity are calculated with a Power-Law. 38
- 4.2 Runtime comparison of the DG-SIMPLE algorithm (**kleinHighorderDiscontinuousGalerkin2016**) and the present solver (XNSEC) for the Couette flow with vertical temperature gradient configuration 41
- 4.3 Differentially heated cavity: Results of Nusselt number and Thermodynamic pressure 43





1 Introduction

hmm

1.1 Introduction and state of the art.

1.1.1 Combustion

Premixed Flames(???)

Non-Premixed Flames

Droplet(?)

High order discretization methods is a topic which has been gaining increasing attention in the last decades. An important exponent of them is the Discontinuous Galerkin (DG) method **cockburnDevelopmentDiscontinuousGalerkin2000**. The DG method was initially developed and utilized for solving hyperbolic conservation laws, especially in the field of computational fluid dynamics (CFD), and has recently gained increased attention for incompressible CFD problems for structured and unstructured grids. Two main advantages stand out when compared with traditional methods such as the Finite Volume Method (FVM) or the Finite Difference Method (FDM): First, DG offers an arbitrary order of error convergence due to the polynomial local approximation of the solution field. A polynomial approximation of degree p provides a numerical discretization error of the order $\mathcal{O}(h^{p+1})$ for sufficiently smooth solutions, where h is a characteristic grid length. Secondly, regardless of the desired order of accuracy, any given cell of the grid only requires information from its immediate neighbours, allowing for efficient parallelization with minimal communication overhead. In contrast, more traditional schemes, such as the FVM, are usually limited to $\mathcal{O}(h^N)$ accuracy, with $N \leq 2$ for unstructured grids. Even for structured grids N is practically limited to low values due to the increasing stencil size for increasing N . Advantageously the DG method offers the locality of low-order schemes and the accuracy per degree of freedom of spectral schemes.

In the context of CFD solvers, an important distinction is that between pressure-based and density-based solvers. Historically, pressure-based solvers have been used for incompressible flows, i.e. flows with divergence-free velocity fields. On the other hand, density-based (also called fully compressible) solvers should, in theory, be able to solve flows in all Mach number ranges. However, in practice, as the Mach number approaches zero, density-based solvers experience efficiency and accuracy problems. These issues are mainly attributed to the acoustic effects in the flow, which tends to generate very stiff systems. None of these approaches are directly applicable to flows with varying density in the low-Mach limit. **henninkPressurebasedSolverLowMach2021** It is possible, however, to extend existing incompressible and compressible codes so that they are capable of dealing with low Mach numbers. **keshtibanCompressibleFlowSolvers2003** In this work a extension from a incompressible solver is presented.

There are numerous works in which the DG method has been used within the context of incompressible flows. **shahbaziHighorderDiscontinuousGalerkin2007**; **kummerBoSSSDiscontinuousGalerkin2011**; **kleinSIMPLEBasedDiscontinuous2013**; **rhebergenSpaceTimeDiscontinuous2013** However, there are not many publications in which the flow problem at low Mach numbers is addressed using a pressure-based solver. In the work by Klein et al. **kleinHighorderDiscontinuousGalerkin2016** the low-Mach equations are solved in a DG Framework making use of a SIMPLE type scheme. The solution of a time-step involves an iterative process that requires multiple matrix assemblies and solutions. The obtained systems of equations are solved by means of fixed-point iterations, where relaxation factors are necessary to obtain convergence of the computations. In the work of Hennink et al. **henninkPressurebasedSolverLowMach2021** a pressure-based solver for low-mach flows is presented. They solve the mass flux instead of the velocity as the primitive variable.

High order methods are very attractive for complex reacting fluid dynamical systems, where usually a high numerical resolution is necessary. Particularly for combustion problems, where large amounts of heat are released in rather small zones within the flow, the high number of elements required to resolve the resulting steep gradients could result in prohibitive calculation times even for simple problems. In particular the study of so-called diffusion flames – also known as non-premixed flames – requires special consideration. In a diffusion flame, the reactants are initially spatially separated. For this kind of system, mixing plays a crucial role because reactants need to be brought together to the flame zone in order to maintain combustion. Many practical applications of diffusion flames consider deflagration flames, **poinotTheoreticalNumericalCombustion2005** which are characterized by a small characteristic velocity compared to the speed of sound. The low-Mach approximation of the Navier–Stokes equations is often chosen for describing this kind of system. This approximation allows for the calculation of non-constant density flows (such as temperature dependent density), while neglecting acoustic effects, thus dramatically reducing the required temporal resolution. **mullerLowMachNumberAsymptoticsNavierStokes1998**

In addition to the compressibility effects mentioned above, the need to accurately and efficiently represent the chemical reactions governing the combustion problem poses a major challenge. Generally speaking, to study the combustion process a detailed chemistry description is preferable. However, this is often impractical as it can be very intensive computationally speaking. Stauch et al. investigated systems with detailed mechanism for methanol combustion, where 23 chemical species and 166 elementary reactions are involved, **stauchDetailedNumericalSimulation2006** and for n-heptane with 62 chemical species and 572 elementary reactions, and with detailed transport processes **stauchAutoignitionSingleNheptane2007**. Because of their high complexity the mentioned works are restricted to simple one- or two-dimensional configurations, and to a small number of grid elements. If one is interested in more complex geometries or more complicated flow systems, the use of detailed kinetics can be prohibitive. Simplified kinetic models have been developed to overcome this difficulty. In the work of Westbrook et al. **westbrookSimplifiedReactionMechanisms1981** a one-step kinetic model is presented, where combustion is expressed as a single chemical reaction with a reaction rate given by an Arrhenius-type expression with constant parameters. Multi-step chemical reaction models have also been developed, such as the four-step mechanism for methane combustion by Peters, **petersNumericalAsymptoticAnalysis1985** or the three-step mechanism by Peters and Williams. **petersAsymptoticStructureStoichiometric1987** Furthermore, extensions of one-step models exist, such as the one presented by Fernandez-Tarrazo et al. **fernandez-tarrazoSimpleOnestepChemistry2006** for hydrocarbon combustion with air,

where kinetic parameters are correlated to the equivalence ratio in order to better describe characteristic flame properties for premixed and non-premixed flames.

In the last decades several numerical investigations related to diffusion flames have been carried out. Burke and Schumann were the first ones to investigate the structure of diffusion flames by studying the flame jet problem. **burkeDiffusionFlames1928** By assuming an infinitely fast chemical reaction they managed to predict flame properties fairly accurately. In the work of Smooke et al. **smookeNumericalSolutionTwoDimensional1986** a numerical simulation for a two-dimensional axisymmetric laminar diffusion jet with detailed chemistry was conducted and solved with Newton-type methods. In order to obtain adequate initial estimates for this problem, the solution of the problem for an infinitely fast chemistry was solved first. This idea was used in several works such as that by Keyes and Smooke **keyesFlameSheetStarting1987** for a counter diffusion flame, by Smooke **smookeNumericalModelingAxisymmetric1992** for a Tsuji-counterflow configuration and in the work by Dobbins et al. **dobbinsFullyImplicitCompact2010** for an axisymmetric laminar jet diffusion flame with time dependent boundary conditions. In the work of Paxion **paxionDevelopmentParallelUnstructured2001** unstructured multigrid solver for laminar flames with detailed chemistry is presented. A Krylov-Newton method was used for solving several flame configurations. A two-dimensional counter diffusion flame was calculated, and its results were compared with the one-dimensional self-similar solution of the equations.

The DG method has also been used for simulations of combustion, mainly within a fully compressible framework. In the work from Johnson et al. **johnsonConservativeDiscontinuousGalerkin2020** the compressible Navier–Stokes equations are solved using a nodal DG scheme for combustion with complex chemistry and transport parameters. An hp-adaptive method is also presented, and shown to be useful for solving the ordinary differential equations used for describing the unsteady behaviour of the system. Similarly in the work from Lv and Ihme **lvHighorderDiscontinuousGalerkin2017** a DG solver for multi-component chemically reacting flows, which solves the fully compressible Navier-Stokes equation, is presented. A hybrid-flux formulation is used, where a conservative Riemann solver is used for shock treatment, and a double-flux formulation is used in smooth regions. They show its applicability for non-reacting and reacting flows, particularly for systems characterized by high Mach numbers. On the other hand, the solution of combustion problems using the DG method in an incompressible framework is a topic that has not received much attention in the literature. This fact is the motivation of the present paper.

The system of equations obtained from the discretization of highly nonlinear systems can be very difficult to solve. Fixed-point iteration schemes have been used as a linearization strategy, as done by Klein et al. **kleinHighorderDiscontinuousGalerkin2016** A major drawback of this approach is the highly problem dependent choice of under-relaxation factors. A much more robust strategy is the use of Newton type methods. **shadidInexactNewtonMethod1997**; **pawlowskiGlobalizationTechniquesNewton2006** Here, a problem-dependent factor is not needed. There is however a trade-off, because the Jacobian matrix has to be calculated, which can be computationally expensive. This approach has been used for combustion problems in numerous works. Karaa et al. **karaaPreconditionedMultigridSimulation2003** studied the axisymmetric laminar jet diffusion flame and investigated the behaviour of a multi-grid solver when using different pre-conditioners with a damped Newton algorithm. Shen et al. **shenNewtonMethodSteady2006a** investigated the use and efficiency of a Newton method coupled with the Bi-CGSTAB method for an axisymmetric laminar jet flame. They concluded that, in terms of computational cost, the steady-state solution is more efficiently obtained

by directly solving the steady formulation of the equations, than by solving the transient Navier-Stokes equations until the steady state is reached.

It is well known that the Newton method shows the property of having quadratic convergence sufficiently close to the solution **deuflhardNewtonMethodsNonlinear2011**. However, if the initial solution guess is not adequate, the method converge to a solution slowly, or may not even converge at all. For some highly nonlinear problems this is a significant issue. The so-called globalized Newton methods are used to overcome this problem by effectively increasing the area of convergence of the method. A popular globalized Newton method is the Newton-Dogleg method, **pawlowskiInexactNewtonDogleg2008** which is based on a trust-region technique.

In the present work, a steady low-Mach pressure-based solver for the simulation of temperature dependent non-reactive and reactive flows using the Discontinuous Galerkin method is presented. To the best of our knowledge, this is the first time that a pressure-based solver is used together with the DG method for solving the reactive low-Mach equations using the Newton-Dogleg method in a fully coupled manner. We focus in this study on two-dimensional configurations, but the ideas presented could be extended to three-dimensional systems. The one-step combustion model presented by Fernandez-Tarrazo et al. **fernandez-tarrazoSimpleOnestepChemistry2006** is used for describing the chemical reactions. In the present work we consider only methane combustion, but the one-step model could be used for other hydrocarbons as well. We choose this chemical model to obtain physically correct results for a wide range of applications, while avoiding the use of complex chemistry models. The discrete system of equations is solved by a globalized Newton method, by means of the Dogleg approach. In addition to the Newton-Dogleg method, a homotopy strategy is presented, which was found to be useful for obtaining solutions of steady state calculations of highly nonlinear problems. In order to find appropriate initial values for Newton's method in combustion applications, the concept of flame sheet estimates (i.e. the solution for infinitely fast chemistry) is used. Several benchmark cases are presented that allow us to validate our implementation. First we solve the differentially heated cavity problem, with which we intend to validate our implementation of the low-Mach solver for non-constant density flows using the fully coupled solver. Later two flame configurations are calculated, namely the counter-diffusion flame and the chambered diffusion flame. **(matalonDiffusionFlamesChamber1980)**

In the following, we consider a two-dimensional system. However, the methods shown in this work could be also used for three-dimensional problems.

They were first derived by Rehm and Baum (**rehmEquationsMotionThermally1978**). A rigorous extension to combustion problems was done by Majda and Sethian (**majdaDerivationNumericalSolution19**

2 Governing equations

In this work we present the methodology used to simulate reactive fluids in the low-Mach regime using the DG method. In this chapter we intend to show the governing equations, which will be discretized in the following chapters. First, in Section 2.1 the equations for a flow in the low-Mach regime with finite reaction velocity are shown. A brief derivation of the set of low-Mach equations is presented, which should also serve as a way of showing and justifying the assumptions made in this work. We restricted ourselves to a one-step chemical model, but the algorithm presented could also be used for more complex chemistry models. Subsequently, in Section 2.2 the governing equations are shown for the case of assuming an irreversible chemical model with an infinite reaction rate. This case is often called the Burke–Schumann limit. These equations are used as part of the algorithm to solve the finite reaction rate case.

2.1 The low-Mach number equations for reactive flows

Combustion processes can be modeled by a system of nonlinear partial differential equations, namely the balance equations for total mass, momentum, energy, and mass of individual species (usually expressed in terms of mass fractions). This system needs to be solved together with an equation of state and expressions for the transport properties as well as for the chemical reaction rates. The derivation of the governing equations for a reacting flow system can be found in the literature. (see, for example, (keeChemicallyReactingFlow2003), (poinotTheoreticalNumericalCombustion2005)). In the following pages, the main ideas regarding the derivation of equations are presented. For a more detailed explanation, we refer to the cited works and the references therein.

2.1.1 The reactive Navier–Stokes equations

Throughout this work, variables with a hat sign, e.g. $\hat{\rho}$ represent dimensional variables, while those without it are nondimensional. We start the derivation of the low-Mach number equations with the Navier–Stokes equations, the energy equation (in its temperature form), and the species transport equations. Let us consider a reacting fluid mixture composed of N species. Let $\hat{\mathbf{x}} = (\hat{x}, \hat{y}, \hat{z})$ and \hat{t} be the spatial vector and time. The primitive variables are the velocity field $\hat{\mathbf{u}} = (\hat{u}, \hat{v}, \hat{w})$, the pressure \hat{p} , the temperature \hat{T} , and the mass fractions Y_k of the N total

species. The set of governing equations to be solved is

$$\frac{\partial \hat{\rho}}{\partial t} + \hat{\nabla} \cdot (\hat{\rho} \hat{\mathbf{u}}) = 0, \quad (2.1a)$$

$$\frac{\partial \hat{\rho} \hat{\mathbf{u}}}{\partial t} + \hat{\nabla} \cdot (\hat{\rho} \hat{\mathbf{u}} \otimes \hat{\mathbf{u}}) = -\hat{\nabla} \hat{p} - \hat{\nabla} \cdot \hat{\boldsymbol{\tau}} - \hat{\rho} \hat{\mathbf{g}}, \quad (2.1b)$$

$$\hat{\rho} \hat{c}_p \frac{\partial \hat{T}}{\partial t} + \hat{\rho} \hat{c}_p \hat{\mathbf{u}} \cdot \hat{\nabla} \hat{T} = \frac{D \hat{p}}{D t} - \hat{\nabla} \cdot \hat{\mathbf{q}} + \hat{\boldsymbol{\tau}} : \hat{\nabla} \hat{\mathbf{u}} + \hat{\omega}_T \quad (2.1c)$$

$$\frac{\partial \hat{\rho} Y_k}{\partial t} + \hat{\nabla} \cdot (\hat{\rho} \hat{\mathbf{u}} Y_k) = -\hat{\nabla} \cdot \hat{\mathbf{j}}_k + \hat{\omega}_k \quad (k = 1, \dots, N) \quad (2.1d)$$

This results in (in the general case) $N + 5$ differential equations to be solved. In these equations, $\hat{\rho}$ is the density of the mixture and $\hat{\mathbf{g}}$ is the acceleration of gravity. $\hat{\boldsymbol{\tau}}$, $\hat{\mathbf{q}}$ and $\hat{\mathbf{j}}_k$ are the viscous tensor, the heat flux vector and the molecular mass flux vector of species k , respectively. Additionally, $\hat{\omega}_T$ is the heat release due to combustion and $\hat{\omega}_k$ is the reaction rate of species k . To close the system, expressions must be defined to link these variables with the primitive variables. They will be briefly shown and commented upon in the following paragraphs.

Equation of state

Assuming that the fluid behaves ideally, the density can be calculated as

$$\hat{\rho} = \frac{\hat{p} \hat{W}_{\text{avg}}}{\hat{\mathcal{R}} \hat{T}}. \quad (2.2)$$

Here, $\hat{\mathcal{R}}$ is the universal gas constant of gases, and \hat{W}_{avg} is the average molecular weight of the fluid, defined as

$$\hat{W}_{\text{avg}} = \left(\sum_{k=1}^N \frac{Y_k}{\hat{W}_k} \right)^{-1} \quad (2.3)$$

with \hat{W}_k as the molecular weight of species k . For an ideal mixture, the specific heat capacity can be calculated as weighted averages of the specific heats of the species,

$$\hat{c}_p = \sum_{k=1}^N Y_k \hat{c}_{p,k}, \quad (2.4)$$

where $\hat{c}_{p,k}$ corresponds to the specific heat capacity of the component k . The temperature dependence of $\hat{c}_{p,k}$ can be accounted for by using NASA polynomials (**mcbrideNASAThermodynamicData1993**).

$$\hat{c}_{p,k} = \left(\hat{a}_1 + \hat{a}_2 \hat{T} + \hat{a}_3 \hat{T}^2 + \hat{a}_4 \hat{T}^3 + \hat{a}_5 \hat{T}^4 \right) \frac{\hat{\mathcal{R}}}{\hat{W}_k} \quad (2.5)$$

where \hat{a}_1 , \hat{a}_2 , \hat{a}_3 , \hat{a}_4 and \hat{a}_5 are numerical coefficients supplied by the NASA database.

Transport models

The viscous tensor $\hat{\boldsymbol{\tau}}$ is defined for a Newtonian fluid as

$$\hat{\boldsymbol{\tau}} = -\hat{\mu} \left(\hat{\nabla} \hat{\mathbf{u}} + (\hat{\nabla} \hat{\mathbf{u}})^T \right) + \left(\frac{2}{3} \hat{\mu} - \hat{\kappa} \right) (\hat{\nabla} \cdot \hat{\mathbf{u}}) \mathbf{I} \quad (2.6)$$

Here, $\hat{\mu}$ is the dynamic viscosity of the fluid, which is generally specific to the fluids and depends on its temperature and pressure. Furthermore, $\hat{\kappa}$ corresponds to the bulk viscosity, which is usually negligible for fluids at low pressures (**birdTransportPhenomena1960**). $\hat{\kappa}$ will be taken equal to zero in the rest of this work.

The heat flux vector $\hat{\mathbf{q}}$ is given by Fourier's law of heat conduction,

$$\hat{\mathbf{q}} = \hat{\lambda} \hat{\nabla} \hat{T}. \quad (2.7)$$

Here $\hat{\lambda}$ corresponds to thermal conductivity, which, similar to the viscosity, is dependent on the particular fluid under study and its temperature and pressure.

The molecular mass flux vector $\hat{\mathbf{j}}_k$ of species k is defined as $\hat{\mathbf{j}}_k = \hat{\rho} \hat{\mathbf{U}}_k$. Here $\hat{\mathbf{U}}_k$ is the diffusion velocity of the component k . In general, $\hat{\mathbf{U}}_k$ can be obtained by solving the Maxwell-Stefan equations.

$$\nabla X_p = \sum_{k=1}^N \frac{X_p X_k}{D_{pk}} (\mathbf{U}_k - \mathbf{U}_p) \quad p = 1, \dots, N. \quad (2.8)$$

Here $D_{pk} = D_{kp}$ is the binary mass diffusion coefficient of species p in species k . X_p is the mole fraction of species k and is related to the mass fraction of k as $X_k = Y_k \hat{W} / \hat{W}_k$. The solution of the system (2.8) is often a difficult and costly task (**williamsCombustionTheoryFundamental2000; poinsoTheoreticalNumericalCombustion2005**), and often simplifications are made. It can be shown that for binary mixtures ($N = 2$) and for mixtures containing multiple species ($N > 2$) where all diffusion coefficients are equal, the system (2.8) reduces exactly to the well-known Fick's law.

$$\hat{\mathbf{j}}_k = -\hat{\rho} \hat{D}_k \nabla Y_k \quad (2.9)$$

This expression is only exact in the cases mentioned above. For a system where the heat capacities of each species are different, this expression is inconsistent. The variable \hat{D}_k corresponds in this case to the diffusion coefficient of species k in the mixture. An issue regarding the global mass conservation can be pointed out here. Recall that by definition the sum of the the mass fractions must always be one ($\sum_k^N Y_k = 1$). This is only true for the solution of Equation (2.1) if exact expressions for the diffusion velocities are used (**poinsoTheoreticalNumericalCombustion2005**). If some inexact expression is used (as for example Fick's law), the constraint for the sum of the mass fractions will not be fulfilled. This problem can be surpassed by solving the global mass conservation (continuity) equation Equation (2.1a) and only the equations for the first $N - 1$ species Equation (2.1d). Therefore, all inconsistencies that originated from not using an exact species diffusion model are absorbed by Y_N . As pointed out in **poinsoTheoreticalNumericalCombustion2005**, this simplification should only be used if all $N - 1$ species are strongly diluted in species N , such as the case of a flame in air, where the mass fraction of nitrogen is large. It can also be noted that this approach reduces in one the number of differential equations needed to be solved.

The temperature dependence of viscosity can be modeled by Sutherland's law (**sutherlandLIIViscosityGases**)

$$\hat{\mu}(\hat{T}) = \hat{\mu}_{\text{suth}} \left(\frac{\hat{T}}{\hat{T}_{\text{suth}}} \right)^{1.5} \frac{\hat{T}_{\text{suth}} + \hat{S}}{\hat{T} + \hat{S}}. \quad (2.10)$$

Here $\hat{\mu}_{\text{suth}}$ is the viscosity evaluated at a reference temperature \hat{T}_{suth} , and \hat{S} is a material dependent parameter. In all calculations in this work the value of \hat{S} for air is used, $\hat{S} = 110.5$ K. Expressions for determining the thermal conductivity and diffusion coefficients as function of temperature can be obtained using similar expressions, as will be shown later in Section 2.1.2

Chemical model

Consider a system composed of N species where M chemical reactions take place. Chemical reactions can be written in generalized form as follows.

$$\sum_{k=1}^N \nu'_{kj} \mathcal{M}_k \rightleftharpoons \sum_{k=1}^N \nu''_{kj} \mathcal{M}_k \quad \text{for} \quad j = 1, \dots, M \quad (2.11)$$

where ν'_{jk} and ν''_{jk} are the molar stoichiometric coefficients of species k in the chemical reaction j , and \mathcal{M}_j represents the chemical component k .

The reaction rate of species k is $\hat{\omega}_k$, which accounts for the total amount of species k that appear or disappear due to M chemical reactions (c.f. Equations (2.11)). Its given by

$$\hat{\omega}_k = \hat{W}_k \sum_{j=1}^M \nu_{jk} \hat{Q}_j. \quad (2.12)$$

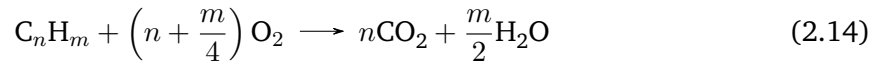
Here $\nu_{kj} = \nu''_{kj} - \nu'_{kj}$, and \hat{Q}_j is the rate of progress of the reaction j . They are usually modeled using Arrhenius-type expressions, as will be shown later.

The heat release $\hat{\omega}_T$ that appears in the energy equation is related to the reaction rates according to

$$\hat{\omega}_T = - \sum_{k=1}^N \hat{h}_k \hat{\omega}_k = - \sum_{k=1}^N \Delta \hat{h}_k^0 \hat{\omega}_k - \sum_{k=1}^N \hat{h}_{ks} \hat{\omega}_k \quad (2.13)$$

Here, the specific enthalpy of k -th species \hat{h}_k is written in terms of its formation enthalpy \hat{h}_k^0 and a sensible enthalpy $\hat{h}_{ks} = \int_0^{\hat{T}} \hat{c}_{p,k} d\hat{T}$. The second term on the right-hand side of Equation (2.13) is usually small and is exactly zero for a mixture where all the heat capacities of each component are equal (**poinsofTheoreticalNumericalCombustion2005**). It will be neglected in the rest of the analysis.

In this work, we use the one-step kinetic model for the combustion of hydrocarbons presented in **fernandez-tarrazoSimpleOnestepChemistry2006**. The chemical reaction is represented by a single ($M = 1$) exothermic global irreversible expression as



The rate of progress of the global reaction is modeled by an Arrhenius-type expression

$$\hat{Q} = \hat{B} e^{-\hat{T}_a/\hat{T}} \left(\frac{\hat{\rho} Y_F}{\hat{W}_F} \right)^a \left(\frac{\hat{\rho} Y_O}{\hat{W}_O} \right)^b. \quad (2.15)$$

Here, the subscripts F and O refer to fuel and oxidizer, respectively. The parameter \hat{B} corresponds to the pre-exponential factor, \hat{T}_a is the activation temperature, and a and b are reaction orders. For a one-step reaction model, the reaction rate of the k -th component (Equation (2.12)) is

$$\hat{\omega}_k = \nu_k \hat{W}_k \hat{Q}. \quad (2.16)$$

\hat{B} (cm ³ /(mol s))	\hat{T}_{a0} (K)	\hat{Q}_0 (MJ kmol ⁻¹)	a	b
6.9×10^{14}	15 900	802.4	1	1

Table 2.1: Base parameters used in the one-step combustion model by fernandez-tarrazoSimpleOnestepChemistry2006

With this definition, the heat release $\hat{\omega}_T$ (Equation (2.13)) is

$$\hat{\omega}_T = -\hat{W}_F \hat{\omega}_F \hat{Q}^m. \quad (2.17)$$

Here is \hat{Q}^m the molar heat of reaction of the one-step reaction. \hat{W}_F and $\hat{\omega}_F$ are the molar mass of the fuel species and the reaction rate of the fuel species.

Within the model from (fernandez-tarrazoSimpleOnestepChemistry2006), several parameters are adjusted to represent characteristic features of premixed flames and diffusion flames. The parameters \hat{T}_a and \hat{Q} are defined as functions of the local equivalence ratio ϕ , which is, in turn, defined in terms of the local mass fractions of fuel Y_F and oxidizer Y_O as

$$\phi = \frac{sY_F^0}{Y_O^0} \frac{sY_F - Y_O + Y_O^0}{s(Y_F^0 - Y_F) + Y_O}, \quad (2.18)$$

where Y_F^0 and Y_O^0 are the mass fractions of the fuel and oxidizer flows in their corresponding feed streams, and s is the mass stoichiometric ratio, defined as $s = \nu_O \hat{W}_O / \nu_F \hat{W}_F$. The activation energy and molar heat release depend on ϕ as

$$\hat{T}_a(\phi) = \begin{cases} (1 + 8.250(\phi - 0.64)^2) \hat{T}_{a0} & \text{if } \phi \leq 0.64, \\ \hat{T}_{a0} & \text{if } 0.64 \leq \phi \leq 1.07, \\ (1 + 4.443(\phi - 1.07)^2) \hat{T}_{a0} & \text{if } \phi \geq 1.07, \end{cases} \quad (2.19)$$

$$\hat{Q}(\phi) = \begin{cases} \hat{Q}_0 & \text{if } \phi \leq 1 \\ (1 - \alpha(\phi - 1)) \hat{Q}_0 & \text{if } \phi > 1, \end{cases} \quad (2.20)$$

The parameter α is a constant that depends on the hydrocarbon being considered. In particular $\alpha = 0.21$ for the combustion of methane.

2.1.2 The unsteady non-dimensional low-Mach equations

In the present work, we use the low-Mach number equation approximation of the governing equations. The derivation of the equations can be found in (rehmEquationsMotionThermally1978; majdaDerivationNumericalSolution1985; mullerLowMachNumberAsymptoticsNavierStokes1998a). We refer to these references for a detailed explanation on how the set of equations is derived. In the following, we restrict ourselves to show and comment on the main consequences of the low-Mach limit.

The low-Mach number limit approximation of the governing equations is used for flows where the Mach number (defined as $Ma = \hat{u}_{\text{ref}}/\hat{c}$, where \hat{u}_{ref} is a characteristic flow velocity and \hat{c} the speed of sound) is small, which is usually the case in typical laminar combustion systems. (dobbinsFullyImplicitCompact2010). The low-Mach equations are obtained by

using standard asymptotic methods. One of the main results of the analysis is that for flows with a small Mach number, the pressure can be decomposed as

$$\hat{p}(\hat{\mathbf{x}}, \hat{t}) = \hat{p}_0(\hat{t}) + \hat{p}_2(\hat{\mathbf{x}}, \hat{t}). \quad (2.21)$$

The spatially uniform term $\hat{p}_0(\hat{t})$ is called thermodynamic pressure, and only appears in the equation of state. It is constant in space, but can change in time. For an open system, the thermodynamic pressure is constant and equal to the ambient pressure, while for a closed system (e.g. a system completely bounded by walls) it changes in order to ensure mass conservation. On the other hand, the perturbational term $\hat{p}_2(\hat{\mathbf{x}}, \hat{t})$ appears only in the momentum equations and plays a role similar to that of the pressure in the classical incompressible formulation. This perturbational term satisfies $\hat{p}_2/\hat{p} \sim \mathcal{O}(\text{Ma})^2$, (**dobbinsFullyImplicitCompact2010; nonakaConservativeThermodynamicallyConsistent2018**) showing that under these assumptions, the equation of state is satisfied only to $\mathcal{O}(\text{Ma}^2)$ (cf. Equation (2.2))

Effectively, the low-Mach limit of the Navier-Stokes equations allows for the calculation of systems where big density variations due to temperature differences are present, thus not restricting ourselves to approximations such as the Boussinesq approximation for buoyancy-driven flow. In addition, this approximation truncates the mechanism of pressure wave propagation which is a natural feature of the compressible Navier-Stokes equations. In doing this, we are no longer restricted to choosing small timesteps to be able to resolve wave phenomena, and the maximum allowed timestep is greatly increased. From now on we will drop the sub-index of the hydrodynamic pressure \hat{p}_2 and we will refer to it simply as \hat{p} , further emphasizing the similarity in its role to the pressure of the incompressible formula.

In this work we use a non-dimensional formulation of the governing equations. We define the non-dimensional quantities.

$$\begin{aligned} \rho &= \frac{\hat{\rho}}{\hat{\rho}_{\text{ref}}}, & p &= \frac{\hat{p}}{\hat{p}_{\text{ref}}}, & \mathbf{u} &= \frac{\hat{\mathbf{u}}}{\hat{u}_{\text{ref}}}, & T &= \frac{\hat{T}}{\hat{T}_{\text{ref}}}, & c_p &= \frac{\hat{c}_p}{\hat{c}_{p,\text{ref}}}, & W_k &= \frac{\hat{W}_k}{\hat{W}_{\text{ref}}} \\ \mu &= \frac{\hat{\mu}}{\hat{\mu}_{\text{ref}}}, & D_k &= \frac{\hat{D}_k}{\hat{D}_{k,\text{ref}}}, & k &= \frac{\hat{k}}{\hat{k}_{\text{ref}}}, & \nabla &= \frac{\hat{\nabla}}{\hat{L}_{\text{ref}}}, & t &= \frac{\hat{t}}{\hat{t}_{\text{ref}}}, & \mathbf{g} &= \frac{\hat{\mathbf{g}}}{\hat{g}_{\text{ref}}}, & Q &= \frac{\hat{Q}}{\hat{Q}_0} \end{aligned}$$

Here \hat{u}_{ref} , \hat{L}_{ref} , \hat{p}_{ref} , \hat{t}_{ref} , and \hat{T}_{ref} are the reference velocity, length, pressure, time, and temperature, respectively, and are equal to some characteristic value for the particular configuration studied. Furthermore, \hat{g}_{ref} is the magnitude of the gravitational acceleration and \hat{W}_{ref} is the reference molecular weight. The reference transport properties $\hat{\mu}_{\text{ref}}$, \hat{k}_{ref} , $\hat{D}_{k,\text{ref}}$ and the reference heat capacity of the mixture and $\hat{c}_{p,\text{ref}}$ are evaluated at the reference temperature \hat{T}_{ref} . Similarly, the reference density must satisfy the equation of state, thus $\hat{\rho}_{\text{ref}} = \hat{p}_{\text{ref}}/(\hat{R}\hat{T}_{\text{ref}}\hat{W}_{\text{ref}})$. By introducing these definitions into the governing equations (Equations (2.1a) to (2.1d)) the reactive set of non-dimensional low-Mach number equations is obtained. The system of differential equations to be solved reads as follows.

$$\frac{\partial \rho}{\partial t} + \nabla \cdot (\rho \mathbf{u}) = 0, \quad (2.22a)$$

$$\frac{\partial \rho \mathbf{u}}{\partial t} + \nabla \cdot (\rho \mathbf{u} \otimes \mathbf{u}) = -\nabla p + \frac{1}{\text{Re}} \nabla \cdot \mu \left(\nabla \mathbf{u} + \nabla \mathbf{u}^T - \frac{2}{3} (\nabla \cdot \mathbf{u}) \mathbf{I} \right) - \frac{1}{\text{Fr}^2} \rho \mathbf{g}, \quad (2.22b)$$

$$\frac{\partial \rho T}{\partial t} + \nabla \cdot (\rho \mathbf{u} T) = \frac{1}{\text{Re Pr}} \nabla \cdot \left(\frac{k}{c_p} \nabla T \right) + \text{H Da} \frac{Q}{c_p}, \quad (2.22c)$$

$$\frac{\partial \rho Y_k}{\partial t} + \nabla \cdot (\rho \mathbf{u} Y_k) = \frac{1}{\text{Re Pr Le}_k} \nabla \cdot (\rho D \nabla Y_k) + \text{Da} \nu_k W_k Q. \quad (k = 1, \dots, N-1) \quad (2.22d)$$

Note that we assumed that the spatial gradients of the mixture heat capacity are small, allowing us to introduce it in the derivative of the diffusive term of Equation (2.22c). Furthermore, using the fact that the sum of the mass fractions must always be one, the mass fraction of the last species N can be calculated with

$$Y_N = 1 - \sum_{k=1}^{N-1} Y_k. \quad (2.23)$$

The N -th component mass fraction Y_N is calculated using Equation (2.23). This system is solved for the primitive variables velocity $\mathbf{u} = (u_x, u_y)$, pressure p , temperature T and mass fractions $\mathbf{Y} = (Y_1, \dots, Y_N)$. We note that the form of the low-Mach equations is very similar to the Navier-Stokes equations. The greatest difference is in the decomposition of the pressure, as mentioned above. This similarity is beneficial, as it allows the use of similar techniques to solve the PDE system to those used for the completely incompressible case (**keshtibanCompressibleFlowSolvers2003**).

Six non-dimensional factors arise from the non-dimensionalization process:

$$\begin{aligned} \text{Re} &= \frac{\hat{\rho}_{\text{ref}} \hat{u}_{\text{ref}} \hat{L}_{\text{ref}}}{\hat{\mu}_{\text{ref}}}, & \text{Fr} &= \frac{\hat{u}_{\text{ref}}}{\sqrt{\hat{g}_{\text{ref}} \hat{L}_{\text{ref}}}}, & \text{Pr} &= \frac{\hat{c}_{p,\text{ref}} \hat{\mu}_{\text{ref}}}{\hat{k}_{\text{ref}}}, \\ \text{Le}_k &= \frac{\hat{k}_{\text{ref}}}{\hat{\rho}_{\text{ref}} \hat{D}_{k,\text{ref}} \hat{c}_{p,\text{ref}}}, & \text{Da} &= \frac{\hat{B} \hat{L}_{\text{ref}} \hat{\rho}_{\text{ref}}}{\hat{M}_{\text{ref}} \hat{u}_{\text{ref}}}, & \text{H} &= \frac{\hat{Q}_0}{\hat{c}_{p,\text{ref}} \hat{T}_{\text{ref}}} \end{aligned}$$

The first three equations define the Reynolds, Froude and Prandtl number respectively. Le_k is the Lewis number of species k . Finally Da and H are the Damköhler number and the non-dimensional heat release respectively. The non-dimensional progress of the global reaction reads as follows.

$$\mathcal{Q}(T, \mathbf{Y}) = \left(\frac{\rho Y_F}{M_F} \right) \left(\frac{\rho Y_O}{M_O} \right) \exp \left(\frac{-T_a}{T} \right), \quad (2.24)$$

where $T_a = \hat{T}_a / \hat{T}_{\text{ref}}$. Furthermore, the non-dimensional heat release is

$$Q(\phi) = \begin{cases} 1 & \text{if } \phi \leq 1 \\ (1 - \alpha(\phi - 1)) & \text{if } \phi > 1, \end{cases} \quad (2.25)$$

with ϕ evaluated according to Equation (2.18). In the low-Mach limit, the ideal gas equation depends on the thermodynamic pressure, temperature and mass fractions. It reads in its non-dimensional form

$$\rho(p_0, T, \mathbf{Y}) = \frac{p_0}{T \sum_{k=1}^N \frac{Y_k}{W_k}}. \quad (2.26)$$

As mentioned above, the thermodynamic pressure of a closed system is a parameter that has to be determined (for an open system is equal to the atmospheric pressure). Defining the initial mass of the fluid inside the closed system as m_0 , and by integrating Equation (2.26) on the whole domain Ω , one obtains

$$p_0(T, \mathbf{Y}) = \frac{m_0}{\int_{\Omega} \frac{W_{\text{avg}}}{T} dV}, \quad (2.27)$$

Similarly, the non-dimensional specific heat capacity of the mixture c_p is calculated as

$$c_p(T, \mathbf{Y}) = \sum_{k=1}^N Y_k c_{p,\alpha}(T), \quad (2.28)$$

and the non-dimensional viscosity as

$$\mu(T) = T^{\frac{3}{2}} \frac{1 + \hat{S}}{\hat{T}_{\text{ref}} T + \hat{S}}. \quad (2.29)$$

As mentioned before, the model for the transport parameters can be simplified by assuming constant values for the Prandtl and Lewis numbers. (**smokeFormulationPremixedNonpremixed1991**) and we can write $\mu(T) = k/c_p(T) = \rho D_k(T)$.

2.2 The flame sheet approximation

Here we introduce the concept of the flame sheet approximation, which is used in our solution algorithm for solving the finite reaction rate system given by Equations (2.1a), (2.1b), (2.22c) and (2.22d). We follow the ideas proposed in the work from **keyesFlameSheetStarting1987**. Assuming that all species have the same constant heat capacity c_p and mass diffusion coefficient $D_k = D$, that the Lewis number is unity for all species, and that combustion can be described by a single-step chemical reaction, it is possible to obtain an equation for a scalar without source terms, taking a linear combination of the energy Equation (2.22c) and mass fraction Equation (2.22d). A commonly used scalar is the mixture fraction z , which per definition is equal to unity in the fuel feed stream, and equal to zero in the oxidizer feed stream. Thus, the system of Equations (2.1a), (2.1b), (2.22c) and (2.22d) can be simplified to solving the low-Mach Navier-Stokes equations together with an equation for the passive scalar z :

$$\frac{\partial \rho}{\partial t} + \nabla \cdot (\rho \mathbf{u}) = 0, \quad (2.30a)$$

$$\frac{\partial \rho \mathbf{u}}{\partial t} + \nabla \cdot (\rho \mathbf{u} \otimes \mathbf{u}) = -\nabla p + \frac{1}{\text{Re}} \nabla \cdot \mu \left(\nabla \mathbf{u} + \nabla \mathbf{u}^T - \frac{2}{3} (\nabla \cdot \mathbf{u}) \mathbf{I} \right) - \frac{1}{\text{Fr}^2} \rho \mathbf{g}, \quad (2.30b)$$

$$\frac{\partial \rho z}{\partial t} + \nabla \cdot (\rho \mathbf{u} z) = \frac{1}{\text{Re Pr}} \nabla \cdot (\rho D \nabla z), \quad (2.30c)$$

which are solved together with the equation of state and expressions for the transport parameters. Note that the system is not closed, because ρ , μ and ρD are still functions of temperature and mass fractions. These fields can be related to the mixture fraction using the concept of the Burke-Schumann flame structure. (**burkeDiffusionFlames1928**) In the case of an infinitely fast chemical reaction, fuel and oxidizer cannot co-exist. On one side of this sheet only oxidizer is found, and on the other side only fuel. The exact position of the flame sheet can be determined by finding the location of points where both reactant mass fractions Y_F and Y_O meet in stoichiometric proportions, that is, the points where the mixture fraction $z = z_{st}$, with

$$z_{st} = \frac{Y_O^0}{Y_O^0 + s Y_F^0}, \quad (2.31)$$

where Y_O^0 is the mass fraction of oxidizer in the oxidizer inlet stream, and Y_F^0 is the mass fraction of fuel in the fuel inlet stream. The Burke-Schumann solution provides analytical expressions for

temperature and mass fraction fields on either side of the flame sheet as function of the mixture fraction z (see for example the textbook from **poinsoTheoreticalNumericalCombustion2005** or the work from **keyesFlameSheetStarting1987**).

$$T(z) = \begin{cases} zT_F^0 + (1-z)T_O^0 + \frac{QY_F^0}{c_p}z_{st}\frac{1-z}{1-z_{st}} & \text{if } z \geq z_{st} \\ zT_F^0 + (1-z)T_O^0 + \frac{QY_F^0}{c_p}z & \text{if } z < z_{st} \end{cases} \quad (2.32)$$

The mass fraction field of fuel and oxidizer species at either side of the flame are given by:

$$Y_F(z) = \begin{cases} Y_F^0 \frac{z - z_{st}}{1 - z_{st}} & \text{if } z \geq z_{st} \\ 0 & \text{if } z < z_{st} \end{cases} \quad (2.33)$$

$$Y_O(z) = \begin{cases} 0 & \text{if } z \geq z_{st} \\ Y_O^0 \left(1 - \frac{z}{z_{st}}\right) & \text{if } z < z_{st} \end{cases} \quad (2.34)$$

and finally, the mass fraction field of product species P is:

$$Y_P(z) = \begin{cases} Y_O^0 \frac{W_P \nu_P}{W_O \nu_O} (1 - z) & \text{if } z \geq z_{st} \\ Y_F^0 \frac{W_P \nu_P}{W_F \nu_F} z & \text{if } z < z_{st} \end{cases} \quad (2.35)$$

Once the mixture fraction field z is obtained, the temperature and mass fraction fields are uniquely defined by Equations (2.32) to (2.35), which are used to evaluate the density and the transport properties. This coupling between variables and the associated nonlinear system leads to the need for an iterative solution scheme.

The main idea of introducing this additional system (Equations (2.30a) to (2.30c)) is to find an approximate solution to the system where a finite reaction-rate is used (Equations (2.22a) to (2.22d)). In Figure 2.1 temperature and fuel mass fraction fields across the center-line of a counterflow flame configuration is shown. Clearly, both solutions are very similar, differing only in the area near the flame. However, this similarity is only valid under the assumptions made to derive Equation (2.30c). In the case that the Lewis number is not equal to one, or that the heat capacities are not equal for each species, the finite-rate solution will differ slightly from that obtained with the infinite-reaction rate.

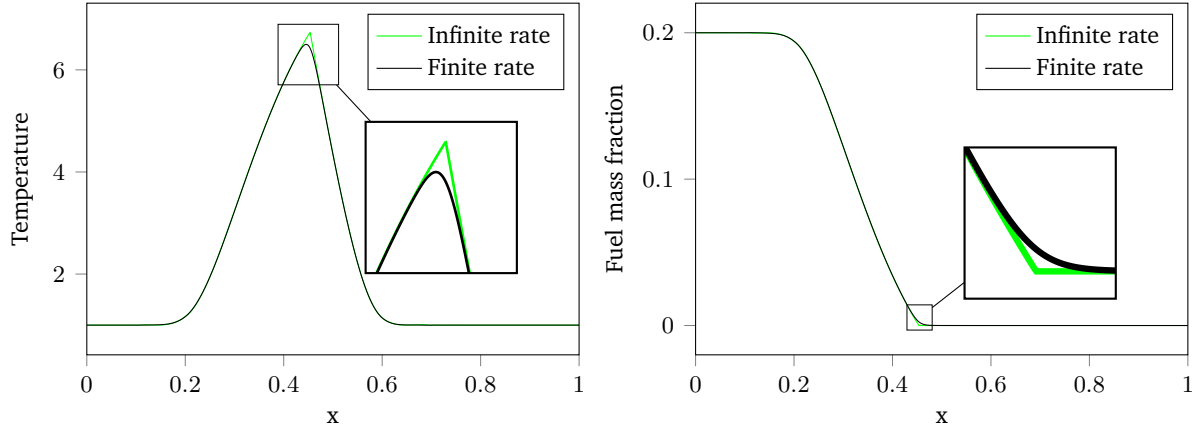


Figure 2.1: Temperature and fuel mass fraction profiles calculated in the center-line of a counter-flow flame configuration using finite chemistry (black) and the flame sheet approximation (green).

2.3 Boundary conditions

The following boundary conditions are imposed for the resolution of the finite reaction rate system (Equations (2.22a) to (2.22d)) and for the flame sheet problem (Equations (2.30a) to (2.30c)).

$$\Gamma_D : \quad \mathbf{u} = \mathbf{u}_D, \quad T = T_D, \quad Y_k = Y_{k,D}, \quad z = z_D, \quad (2.36a)$$

$$\Gamma_{DW} : \quad \mathbf{u} = \mathbf{u}_D, \quad \nabla T \cdot \mathbf{n}_{\partial\Omega} = 0, \quad \nabla Y_k \cdot \mathbf{n}_{\partial\Omega} = 0, \quad \nabla z \cdot \mathbf{n}_{\partial\Omega} = 0, \quad (2.36b)$$

$$\Gamma_N : \quad \left(-p\mathbf{I} + \left(\frac{\mu}{\text{Re}} (\nabla \mathbf{u} + (\nabla \mathbf{u})^T) - \frac{2}{3}\mu(\nabla \cdot \mathbf{u})\mathbf{I} \right) \right) \cdot \mathbf{n}_{\partial\Omega} = 0, \\ \nabla T \cdot \mathbf{n}_{\partial\Omega} = 0, \quad \nabla Y_k \cdot \mathbf{n}_{\partial\Omega} = 0, \quad \nabla z \cdot \mathbf{n}_{\partial\Omega} = 0, \quad (2.36c)$$

$$\Gamma_{ND} : \quad \left(-p\mathbf{I} + \left(\frac{\mu}{\text{Re}} (\nabla \mathbf{u} + (\nabla \mathbf{u})^T) - \frac{2}{3}\mu(\nabla \cdot \mathbf{u})\mathbf{I} \right) \right) \cdot \mathbf{n}_{\partial\Omega} = 0, \\ T = T_D, \quad Y_k = Y_{k,D}, \quad z = z_D \quad (2.36d)$$

$$\Gamma_P : \quad \mathbf{u}(\mathbf{x}) = \mathbf{u}(\mathbf{x}'), \quad T(\mathbf{x}) = T(\mathbf{x}'), \quad Y_k(\mathbf{x}) = Y_k(\mathbf{x}'), \quad z(\mathbf{x}) = z(\mathbf{x}'), \quad (2.36e)$$

where k denotes the index from mass fractions $k = (1, \dots, N-1)$. The boundary Γ_D represents conditions for inlets and walls, with velocity, temperature, mass fractions and mixture fraction defined as Dirichlet boundary conditions. Boundaries Γ_{DW} are used to represent adiabatic walls, where velocity is given as a Dirichlet boundary condition, but with the gradients perpendicular to the wall of the transported scalars set to zero. The boundary Γ_N represent an outflow of the domain with homogeneous Neumann condition for all scalars. The boundary Γ_{ND} also represents an outlet boundary condition, but with Dirichlet boundary conditions for the scalars. Finally the boundaries Γ_P are periodic boundaries, where \mathbf{x} and \mathbf{x}' are periodic pairs in the domain.

3 Numerical methods

3.1 The Discontinuous Galerkin method

3.1.1 Spatial discretization

We start by introducing some standard definitions and notations in the context of DG methods: **kummerExtendedDiscontinuousGalerkin2017** **kikkerFullyCoupledHighorder** We define a computational domain $\Omega \subset \mathbb{R}^2$ with a polygonal and simply connected boundary $\partial\Omega$. Our numerical grid is then defined by the set of non-overlapping elements $\mathcal{K} = \{K_1, \dots, K_N\}$ with a characteristic mesh size h , so that Ω is the union of all elements, i.e. $\Omega = \bigcup_{i=1}^N K_i$. We define $\Gamma = \bigcup_j \partial K_j$ as the union of all edges (internal edges and boundary edges) and $\Gamma_I = \Gamma \setminus \partial\Omega$ as the union of all interior edges. For each edge of Γ a normal field \mathbf{n}_Γ is defined. Particularly on $\partial\Omega$ is defined as an outer normal and $\mathbf{n}_\Gamma = \mathbf{n}_{\partial\Omega}$. For each field $\mathbf{u} \in C^0(\Omega \setminus \Gamma_I)$ we define \mathbf{u}^- and \mathbf{u}^+ , which describe the information in the interior and exterior sides of the cell:

$$\mathbf{u}^- = \lim_{\xi \searrow 0} \mathbf{u}(\mathbf{x} - \xi \mathbf{n}_\Gamma) \quad \text{for } \mathbf{x} \in \Gamma \quad (3.1)$$

$$\mathbf{u}^+ = \lim_{\xi \searrow 0} \mathbf{u}(\mathbf{x} + \xi \mathbf{n}_\Gamma) \quad \text{for } \mathbf{x} \in \Gamma_I \quad (3.2)$$

The jump and mean values of \mathbf{u} on inner edges Γ_I are defined as:

$$[\![\mathbf{u}]\!] = \mathbf{u}^+ - \mathbf{u}^- \quad (3.3)$$

$$\{\mathbf{u}\} = \frac{1}{2} (\mathbf{u}^- + \mathbf{u}^+). \quad (3.4)$$

while the jump and mean values on boundary edges $\partial\Omega$ are:

$$[\![\mathbf{u}]\!] = \mathbf{u}^- \quad (3.5)$$

$$\{\mathbf{u}\} = \mathbf{u}^-. \quad (3.6)$$

We define the broken polynomial space of total degree k as

$$\mathbb{P}_k(\mathcal{K}_h) = \{f \in L^2(\Omega) ; \forall K \in \mathcal{K} : f|_K \text{ is polynomial and } \deg(f|_K) \leq k\}. \quad (3.7)$$

Additionally for $u \in C^1(\Omega \setminus \Gamma)$ the broken gradient $\nabla_h u$ is defined as:

$$\nabla_h u = \begin{cases} 0 & \text{on } \Gamma \\ \nabla u & \text{elsewhere} \end{cases} \quad (3.8)$$

The broken divergence $\nabla_h \cdot u$ is defined analogously. Finally, we define the function space for test and trial functions for D_v dependent variables:

$$\mathbb{V}_{\mathbf{k}} = \prod_{i=1}^{D_v} \mathbb{P}_{k_i}(K_h) \quad (3.9)$$

where $\mathbf{k} = (k_1, \dots, k_{D_v})$.

3.1.2 Discretization for a DG Method

As an introductory example, following [hesthaven_nodal_2008](#), we are considering the discretization of a general conservation law with a non-linear flux function $\mathbf{f}(\psi)$ for a scalar quantity $\psi = \psi(\mathbf{x}, t)$ in Ω and suitable Dirichlet boundary condition on $\partial\Omega = \partial\Omega_D$ and a compatible initial condition ψ_0 . The problem statement reads

$$\frac{\partial\psi}{\partial t} + \nabla \cdot \mathbf{f}(\psi) = 0, \quad \mathbf{x} \in \Omega, \quad (3.10a)$$

$$\psi = \psi_D, \quad \mathbf{x} \in \partial\Omega_D, \quad (3.10b)$$

$$\psi(\mathbf{x}, 0) = \psi_0(\mathbf{x}), \quad \mathbf{x} \in \Omega. \quad (3.10c)$$

The goal is to find an approximate solution $\psi = \psi(\mathbf{x}, t)$ to ψ that fulfils the problem (3.10). Therefore, the problem domain Ω is discretized by a numerical mesh \mathfrak{R}_h and for each numerical cell K_j we introduce the approximation by a local polynomial basis $\phi_j = (\phi_{j,l})_{l=1,\dots,N_k} \in \mathbb{P}_k(\{K_j\})$ with a cell-local support $\text{supp}(\phi_j) = \overline{K_j}$ as

$$\psi_j(\mathbf{x}, t) = \sum_{l=1}^{N_k} \tilde{\psi}_{j,l}(t) \phi_{j,l}(\mathbf{x}) = \tilde{\psi}_j(t) \cdot \phi_j(\mathbf{x}), \quad \mathbf{x} \in K_j, \quad (3.11)$$

where the coefficients $\tilde{\psi}_j = (\tilde{\psi}_{j,l})_{l=1,\dots,N_k}$ denote the unknowns or degrees of freedom (DOF) of the local solution in cell K_j . In this work a modal polynomial basis is used, which fulfils the orthogonality condition

$$\int_{K_j} \phi_{j,m} \phi_{j,n} \, dV = \delta_{mn} \quad (3.12)$$

with the Kronecker delta δ_{mn} . Inserting the local approximation (3.11) into the conservation law (3.10a) results in a cell-wise residual

$$R_j(\mathbf{x}, t) = \frac{\partial\psi_j}{\partial t} + \nabla \cdot \mathbf{f}(\psi_j), \quad \mathbf{x} \in K_j. \quad (3.13)$$

For a Galerkin method, the residual (3.13) is minimized with respect to the same space as the ansatz functions, i.e. $\mathbb{P}_k(\{K_j\})$. Thus, we demand for the test functions $\vartheta_{j,l} = \phi_{j,l}$ in each cell $K_j \in \mathfrak{R}_h$ that

$$\int_{K_j} R_j \vartheta_{j,l} \, dV = \int_{K_j} \frac{\partial\psi_j}{\partial t} \phi_{j,l} + \nabla \cdot \mathbf{f}(\psi_j) \phi_{j,l} \, dV \stackrel{!}{=} 0, \quad \forall \phi_{j,l}. \quad (3.14)$$

So, for each cell we end up with a linear system of N_k equations. However so far, no approximate global solution $\psi \in \Omega$ can be regained from the minimization in (3.14). The global solution is assumed to be a piecewise polynomial approximation

$$\psi(\mathbf{x}, t) \approx \psi(\mathbf{x}, t) = \bigoplus_{j=1}^J \psi_j(\mathbf{x}, t) = \sum_{j=1}^J \sum_{l=1}^{N_k} \tilde{\psi}_{j,l}(t) \phi_{j,l}(\mathbf{x}) \in \mathbb{P}_k(\mathfrak{R}_h) \quad (3.15)$$

defined as the direct sum of the J local solutions ψ_j in (3.11). Here, $\tilde{\psi}_{j,l}$, with $j = 1, \dots, J$ and $l = 1, \dots, N_k$, denote the total DOF, with $N = J \cdot N_k$, of the global approximate solution ψ . In

order to formulate a global DG method, the spatial term on the right-hand side of equation (3.14) is rewritten in terms of boundary edge integrals $\forall K_j \in \mathfrak{K}_h$ using partial integration

$$\int_{K_j} \frac{\partial \psi_j}{\partial t} \phi_{j,l} dV - \int_{K_j} \mathbf{f}(\psi_j) \cdot \nabla_h \phi_{j,l} dV + \oint_{\partial K_j} (\mathbf{f}(\psi_j) \cdot \mathbf{n}_j) \phi_{j,l} dS = 0, \quad \forall \phi_{j,l}, \quad (3.16)$$

where \mathbf{n}_j represents the local outward pointing normal for cell K_j . Note that on the internal edges Γ_{int} the value of $\mathbf{f}(\psi_j)$ is multiply defined. Therefore, a numerical flux \hat{F} is introduced

$$\hat{F}(\psi_j^{\text{in}}, \psi_j^{\text{out}}, \mathbf{n}_j) \approx \mathbf{f}(\psi_j) \cdot \mathbf{n}_j, \quad (3.17)$$

that uniquely defines the resulting value of both neighbouring values, i.e. ψ_j^{in} and ψ_j^{out} at internal edges Γ_{int} . Summing over all cells K_j , the global minimization problem for $\psi(\mathbf{x}, t)$, $\mathbf{x} \in \Omega$ reads: Find $\psi \in \mathbb{P}_k(\mathfrak{K}_h)$, such that $\forall \vartheta = \phi \in \mathbb{P}_k(\mathfrak{K}_h)$

$$\int_{\Omega} \frac{\partial \psi}{\partial t} \phi dV - \int_{\Omega} \mathbf{f}(\psi) \cdot \nabla_h \phi dV + \oint_{\Gamma} \hat{F}(\psi^{\text{in}}, \psi^{\text{out}}, \mathbf{n}_j) [\![\phi]\!] dS = 0, \quad (3.18)$$

where at Γ_D the outer value $\psi^{\text{out}} = \psi_D$ is given by the Dirichlet boundary condition (3.10b). In order to fully discretize the initial boundary value problem (3.10), one further needs to discretize the temporal term. This issue is skipped at this point and is discussed in Section ?? . Thus, the current form of (3.18) is referred to as the semi-discrete weak formulation of (3.10).

Considering the spatial discretization, the numerical flux \hat{F} needs to satisfy certain mathematical and physical properties to ensure stability and convergence of the DG method. In this work the stability is defined in the continuous setting via the energy estimate

$$\|\psi(\mathbf{x}, t)\|_{\Omega}^2 \leq \|\psi(\mathbf{x}, 0)\|_{\Omega}^2, \quad \forall t \geq 0, \quad (3.19)$$

where homogenous Dirichlet conditions are assumed. Thus, stability is given, if the energy $\|\psi(\mathbf{x}, t)\|_{\Omega}^2$ only decreases in the absence of an inflow. Two properties need to be fulfilled in order to proof that the discrete problem (3.18) satisfies the discrete equivalent of the energy estimate in (3.19). The numerical flux \hat{F} is required to be a function that is Lipschitz continuous and monotonic, see **di_pietro_mathematical_2012** for the proof. Furthermore, it is obvious that the DG method needs to regain a unique approximate solution to the underlying problem. Thus, \hat{F} satisfies the following consistency property

$$\hat{F}(a, a, \mathbf{n}) = \mathbf{f}(a) \cdot \mathbf{n}, \quad \forall a \in \mathbb{R}. \quad (3.20)$$

A direct consequence of (3.20) is that the weak formulation (3.18) is directly fulfilled for $\psi = \psi$. Since considering a general conservation law in its conservative form, one further requires that \hat{F} regains the global conservation property, i.e. the total amount of ψ only changes due to fluxes across the domain boundary $\partial\Omega$, by satisfying

$$\hat{F}(a, b, \mathbf{n}) = -\hat{F}(a, b, -\mathbf{n}), \quad \forall a, b \in \mathbb{R}. \quad (3.21)$$

The specific form of a suitable numerical flux \hat{F} is presented in Section ?? , where the spatial discretization of the two-phase flow problem is discussed.

Note that the system (3.18) can be written in a shorten matrix formulation as

$$\mathbf{M} \frac{d\tilde{\psi}}{dt} + \mathbf{Op}(\tilde{\psi}) = \mathbf{b}, \quad (3.22)$$

where the sought-after coefficients are given as the solution vector $\tilde{\psi} = \{\tilde{\psi}_{1,1}, \tilde{\psi}_{1,2}, \dots, \tilde{\psi}_{j,n}, \dots, \tilde{\psi}_{J,N_k}\} \in \mathbb{R}^N$. The mass matrix $\mathbf{M} \in \mathbb{R}^{N \times N}$ has a block-diagonal structure with

$$\mathbf{M} = \begin{bmatrix} \mathbf{M}_1 & 0 & \cdots & 0 \\ 0 & \mathbf{M}_2 & \cdots & 0 \\ \vdots & \vdots & \ddots & \vdots \\ 0 & 0 & \cdots & \mathbf{M}_J \end{bmatrix}, \quad (3.23)$$

where the cell-local mass matrix \mathbf{M}_j is defined by

$$(\mathbf{M}_j)_{m,n} = \int_{K_j} \phi_{j,m} \phi_{j,n} \, dV = \int_{K_j} \phi_j \otimes \phi_j \, dV. \quad (3.24)$$

The cell-local Operator matrix \mathbf{Op}_j is given by

$$(\mathbf{Op}_j)_{m,n} = - \int_{K_j} \mathbf{f}(\tilde{\psi}_{j,n} \phi_{j,n}) \cdot \nabla_h \phi_{j,m} \, dV + \oint_{\partial K_j} \hat{F}(\tilde{\psi}_{j,n}, \tilde{\psi}_{j^*,n}, \mathbf{n}_j) \phi_{j,m} \, dS, \quad (3.25)$$

where j^* denotes the index of a neighbouring cell to K_j . Like the mass matrix, the operator matrix exhibits a block-diagonal structure, but including secondary diagonals due to the coupling with neighbouring cells over the numerical fluxes \hat{F} . The right-hand side \mathbf{b} incorporates the given Dirichlet boundary condition value ψ_D .

Discontinuous Galerkin discretization of the finite reaction rate problem

We start by presenting the DG discretization of the finite reaction system defined by ??–2.22d. We define $\mathbf{Y}' = (Y_1, \dots, Y_{n_s-1})$ as the vector containing the first $(n_s - 1)$ mass fractions and $\mathbf{s} = (s_1, \dots, s_{n_s-1})$ as the vector containing the test functions for the first $(n_s - 1)$ mass fraction equations. The discretized form of ??? and Equations (2.22c) and (2.22d) is obtained by multiplying each equation by a test function, integrating it over an element K , applying integration by parts and finally using an adequate numerical flux for each term. Note that the convective and diffusive terms of the temperature scalars T , mass fraction Y_α and mixture fraction z have the same form, so they share the same expression in their discretized form. In order to ensure the validity of the Ladyzenskaja-Babuška-Brezzi (or inf-sup) condition, **babuskaFiniteElementMethod1973** we use a mixed order formulation, where polynomials of order k for velocity, temperature and mass fractions, and of degree $k' = k - 1$ for pressure are used. Finally the discretized problem can be written as: find the numerical solution $(p_h, \mathbf{u}_h, T_h, \mathbf{Y}'_h) \in \mathbb{V}_k$ such that for all test functions $(q_h, \mathbf{v}_h, r_h, \mathbf{s}_h) \in \mathbb{V}_k$ we have:

$$\mathcal{C}(\mathbf{u}_h, q_h, \rho(T_h, \mathbf{Y}_h)) = \mathcal{B}^1(q_h), \quad (3.26a)$$

$$\mathcal{U}^C(\mathbf{u}_h, \mathbf{u}_h, \mathbf{v}_h, \rho(T_h, \mathbf{Y}_h)) + \mathcal{U}^P(p_h, \mathbf{v}_h) + \frac{1}{\text{Re}} \mathcal{U}^D(\mathbf{u}_h, \mathbf{v}_h, \mu(T_h)) + \frac{1}{\text{Fr}^2} \mathcal{U}^S(\rho(T_h, \mathbf{Y}_h), \mathbf{v}_h) = \mathcal{B}^2(\mathbf{v}_h), \quad (3.26b)$$

$$\mathcal{S}^C(\mathbf{u}_h, T_h, r_h, \rho(T_h, \mathbf{Y}_h)) + \frac{1}{\text{Re Pr}} \mathcal{S}^D(T_h, r_h, k/c_p(T_h)) + \text{H Da} \mathcal{S}^S(r_h, Q(T_h, \mathbf{Y}_h), \omega(T_h, \mathbf{Y}_h), c_p(T_h, \mathbf{Y}_h)) = \mathcal{B}^3(r_h) \quad (3.26c)$$

$$\mathcal{S}^C(\mathbf{u}_h, Y_{\alpha h}, s_{\alpha h}, \rho(T_h, \mathbf{Y}_h)) + \frac{1}{\text{Re Pr Le}_\alpha} \mathcal{S}^D(Y_{\alpha h}, s_{\alpha h}, \rho D_\alpha(T_h)) + \text{Da} \mathcal{M}_\alpha^S(s_{\alpha h}, \omega(T_h, \mathbf{Y}_h)) = \mathcal{B}^3(s_{\alpha h}). \quad (3.26d)$$

where the index α takes values $\alpha = 1, \dots, (n_s - 1)$. The n_s -th component mass fraction Y_{n_s} is calculated using Equation (2.23).

Discontinuous Galerkin discretization of the flame sheet problem

Discretizing the flame sheet problem given by Equations (2.30a) to (2.30c) proceeds in a similar way. Due to the similarity of the mass fraction equation and the mixture fraction equation the discretization is analogous. Again, we use a mixed order formulation of polynomials of degree k for velocity and mixture fraction, and of degree $k - 1$ for pressure. The resulting problem reads: find the numerical solution $(p_h, \mathbf{u}_h, z_h) \in \mathbb{V}_k$ such that for all test functions $(q_h, \mathbf{v}_h, r_h) \in \mathbb{V}_k$ we have:

$$\mathcal{C}(\mathbf{u}_h, q_h, \rho(z_h)) = \mathcal{B}^1(q_h), \quad (3.27a)$$

$$\mathcal{U}^C(\mathbf{w}_h, \mathbf{u}_h, \mathbf{v}_h, \rho(z_h)) + \mathcal{U}^P(p_h, \mathbf{v}_h) + \frac{1}{\text{Re}} \mathcal{U}^D(\mathbf{u}_h, \mathbf{v}_h, \mu(z_h)) + \frac{1}{\text{Fr}^2} \mathcal{U}^S(\rho(z), \mathbf{v}_h) = \mathcal{B}^2(\mathbf{v}_h), \quad (3.27b)$$

$$\mathcal{S}^C(\mathbf{u}_h, z_h, r_h, \rho(z_h)) + \frac{1}{\text{Re Pr}} \mathcal{S}^D(z_h, r_h, \rho D(z_h)) = \mathcal{B}^3(r_h). \quad (3.27c)$$

Note that density and transport parameters are dependent on the mixture fraction z . The evaluation of those parameters is done as mentioned in ?? and solved iteratively using a Newton-Dogleg type method as shown later in Section 3.2.1

Definitions of nonlinear forms

We show in the following the nonlinear forms used in this work. Regarding the choice of fluxes, we follow the "best practices" known in literature for the incompressible Navier-Stokes equation. It is known [pietroMathematicalAspectsDiscontinuous2012](#); [giraultDiscontinuousGalerkinMethod2004](#) that central difference fluxes for the pressure gradient and velocity divergence, combined with a coercive form for the viscous terms, e.g. symmetric interior penalty, gives a stable discretization for the Stokes equation. Furthermore, it is known that for all kinds of convective terms, a numerical flux which transports information in characteristic direction, e.g. Upwind, Lax-Friedrichs or Local-Lax-Friedrichs, must be used. We opted for the last one in our implementation, as it offers a good compromise between accuracy and stability.

Continuity equation We use a central difference flux for the discretization of the continuity equation:

$$\mathcal{C}(\mathbf{u}, q, \rho) = \oint_{\Gamma_I \cup \Gamma_N \cup \Gamma_{ND} \cup \Gamma_P} \{\rho \mathbf{u}\} \cdot \mathbf{n}_\Gamma [q] \, dS - \int_{\Omega} \rho \mathbf{u} \cdot \nabla_h q \, dV. \quad (3.28)$$

The density in Equation (3.28) is evaluated as a function of the temperature and mass fractions using the equation of state (Equation (2.26)). The term \mathcal{B}^1 on the right hand sides of Equation (3.26a) and Equation (3.27a) contains the Dirichlet boundary conditions:

$$\mathcal{B}^1(q) = - \oint_{\Gamma_D \cup \Gamma_{DW}} q(\rho_D \mathbf{u}_D \cdot \mathbf{n}_\Gamma) \cdot dS \quad (3.29)$$

The density at the boundary ρ_D is evaluated with Equation (2.26) using the corresponding Dirichlet values of temperature and mass fractions.

Momentum equations The convective term of the momentum equations is discretized using a Lax-Friedrichs flux

$$\mathcal{U}^C(\mathbf{w}, \mathbf{u}, \mathbf{v}, \rho) = \oint_{\Gamma} \left(\{\rho \mathbf{u} \otimes \mathbf{w}\} \mathbf{n}_{\Gamma} + \frac{\gamma_1}{2} [\![\mathbf{u}]\!] \right) \cdot [\![\mathbf{v}]\!] \, dS - \int_{\Omega} (\rho \mathbf{u} \otimes \mathbf{w}) : \nabla_h \mathbf{v} \, dV. \quad (3.30)$$

The Lax-Friedrichs parameter γ_1 is calculated as **kleinHighorderDiscontinuousGalerkin2016**

$$\gamma_1 = \max \left\{ 2\overline{\rho^+} |\overline{\mathbf{u}^+} \cdot \mathbf{n}^+|, 2\overline{\rho^-} |\overline{\mathbf{u}^-} \cdot \mathbf{n}^-| \right\}, \quad (3.31)$$

where $\overline{\rho_h^{\pm}}$ and $\overline{\mathbf{u}^{\pm}}$ are the mean values of ρ^{\pm} and \mathbf{u}^{\pm} in K^{\pm} , respectively.

The pressure term is discretized by using a central difference flux

$$\mathcal{U}^P(p, \mathbf{v}) = \oint_{\Gamma \setminus \Gamma_N \setminus \Gamma_{ND}} \{p\} ([\![\mathbf{v}]\!] \cdot \mathbf{n}) \, dS - \int_{\Omega} p \nabla_h \cdot \mathbf{v} \, dV. \quad (3.32)$$

The diffusive term of the momentum equations is discretized using an Symmetric Interior Penalty (SIP) formulation **shahbaziExplicitExpressionPenalty2005**

$$\begin{aligned} \mathcal{U}^D(\mathbf{u}, \mathbf{v}, \mu) = & \int_{\Omega} \left(\mu \left((\nabla_h \mathbf{u}) + (\nabla_h \mathbf{u})^T - \frac{2}{3} (\nabla_h \cdot \mathbf{u}) \mathbf{I} \right) \right) : \nabla_h \mathbf{v} \, dV \\ & - \oint_{\Gamma \setminus \Gamma_N \setminus \Gamma_{ND}} \left(\left\{ \mu (\nabla_h \mathbf{u} + \nabla_h \mathbf{u}^T - \frac{2}{3} (\nabla_h \cdot \mathbf{u}) \mathbf{I}) \right\} \mathbf{n}_{\Gamma} \right) \cdot [\![\mathbf{v}]\!] \, dS \\ & - \oint_{\Gamma \setminus \Gamma_N \setminus \Gamma_{ND}} \left(\left\{ \mu (\nabla_h \mathbf{v} + \nabla_h \mathbf{v}^T - \frac{2}{3} (\nabla_h \cdot \mathbf{v}) \mathbf{I}) \right\} \mathbf{n}_{\Gamma} \right) \cdot [\![\mathbf{u}]\!] \, dS \\ & + \oint_{\Gamma \setminus \Gamma_N \setminus \Gamma_{ND}} \eta \mu_{max} [\![\mathbf{u}]\!] [\![\mathbf{v}]\!] \, dS. \end{aligned} \quad (3.33)$$

The viscosity μ is evaluated as a function of temperature according to Equation (2.29) and $\mu_{max} = \max(\mu^+, \mu^-)$. Additionally η is the penalty term of the SIP formulation, which has to be chosen big enough to ensure coercivity of the form, but also as small as possible in order to not increase the condition number of the problem. The estimation of the penalty term is based on an expression of the form

$$\eta = \eta_0 \frac{A(\partial K)}{V(K)}, \quad (3.34)$$

where for a two-dimensional problem A is the perimeter and V the area of the element. Parameter η_0 is a safety factor and is set $\eta_0 = 4$ in all calculations. Further information on the determination of the penalty term can be found in **hillewaertDevelopmentDiscontinuousGalerkin2013b**. The source term arising due to body forces is:

$$\mathcal{U}^S(\rho, \mathbf{v}) = \int_{\Omega} \rho \frac{\mathbf{g}}{\|\mathbf{g}\|} \cdot \mathbf{v} \, dV. \quad (3.35)$$

The right hand sides of Equation (3.26b) and Equation (3.27b) contain the information from Dirichlet boundary conditions:

$$\mathcal{B}^2(\mathbf{v}) = - \oint_{\Gamma_D} \left((\rho \mathbf{u}_D \otimes \mathbf{u}_D) \mathbf{n}_{\Gamma} + \frac{\gamma_1}{2} \mathbf{u}_D \right) \cdot \mathbf{v} \, dS + \oint_{\Gamma_D} \mu_D \mathbf{u}_D \cdot (\nabla_h \mathbf{v} \mathbf{n}_{\Gamma} + \nabla_h \mathbf{v}^T \mathbf{n}_{\Gamma} - \eta \mathbf{v}) \, dS. \quad (3.36)$$

The Dirichlet viscosity value μ_D is calculated from Equation (2.29) using the Dirichlet values of the temperature at the boundary.

Scalar equations Since the convective and diffusive term for the temperature, mass fractions and mixture fraction share a similar form, we summarize here their discretized expressions in terms of an arbitrary scalar X (corresponding to T in the energy equation, Y_α in the equation for species α and z for the mixture fraction equation) and transport parameter ξ (i.e. k/c_p in the energy equation, and (ρD) for the mass fraction and mixture fraction equations). The convective term of the scalars is discretized using a Lax-Friedrichs flux

$$\mathcal{S}^C(\mathbf{u}, X, r, \rho) = \oint_{\Gamma} \left(\{\rho \mathbf{u} X\} \cdot \mathbf{n} + \frac{\gamma_2}{2} \llbracket X \rrbracket \right) \llbracket r \rrbracket \, dS - \int_{\Omega} (\rho \mathbf{u} X \cdot \nabla_h r) \, dV. \quad (3.37)$$

The Lax-Friedrichs parameter γ_2 is calculated as **kleinHighorderDiscontinuousGalerkin2016**

$$\gamma_2 = \max \left\{ \overline{\rho^+} |\overline{\mathbf{u}^+} \cdot \mathbf{n}^+|, \overline{\rho^-} |\overline{\mathbf{u}^-} \cdot \mathbf{n}^-| \right\}. \quad (3.38)$$

The diffusion term of scalars is discretized again with a SIP formulation:

$$\mathcal{S}^D(X, r, \xi) = \int_{\Omega} (\xi \nabla_h X \cdot \nabla_h r) \, dV - \oint_{\Gamma \setminus \Gamma_N \setminus \Gamma_{ND}} \left(\{\xi \nabla_h X\} \cdot \mathbf{n} \llbracket r \rrbracket + \{\xi \nabla_h r\} \cdot \mathbf{n} \llbracket X \rrbracket - \eta \xi_{\max} \llbracket X \rrbracket \llbracket r \rrbracket \right) \, dS. \quad (3.39)$$

The transport parameter ξ is calculated as a function of temperature using Equation (2.29) and $\xi_{\max} = \max(\xi^+, \xi^-)$. The boundary condition term of the corresponding scalar equation is:

$$\mathcal{B}^3(r) = - \oint_{\Gamma_D \cup \Gamma_{ND}} \left((\rho_D \mathbf{u}_D X_D) \cdot \mathbf{n}_\Gamma + \frac{\gamma_2}{2} X_D \right) r \, dS + \oint_{\Gamma_D \cup \Gamma_{ND}} \xi_D X_D (\nabla_h r \cdot \mathbf{n}_\Gamma - \eta r) \, dS. \quad (3.40)$$

Here, X_D is the Dirichlet value of the scalar X on boundaries and ξ_D is the corresponding transport parameter calculated, which is calculated with Equation (2.29) using the Dirichlet values of the temperature at the boundary. Finally, the volumetric source term of the energy and mass fraction equations are defined as follows:

$$\mathcal{S}^S(r, Q, \omega, c_p) = \int_{\Omega} \frac{Q \omega}{c_p} r \, dV, \quad (3.41)$$

$$\mathcal{M}_\alpha^S(s_\alpha, \omega) = \int_{\Omega} \nu_\alpha M_\alpha \omega s_\alpha \, dV. \quad (3.42)$$

The heat release Q is calculated with Equation (2.25), the reaction rate ω is evaluated using Equation (2.24) and the mixture heat capacity with Equation (2.28).

3.1.3 Temporal discretization

Dies hier ist ein Blindtext zum Testen von Textausgaben. Wer diesen Text liest, ist selbst schuld. Der Text gibt lediglich den Grauwert der Schrift an. Ist das wirklich so? Ist es gleichgültig, ob ich schreibe: „Dies ist ein Blindtext“ oder „Huardest gefburn“? Kjift – mitnichten! Ein Blindtext bietet mir wichtige Informationen. An ihm messe ich die Lesbarkeit einer Schrift, ihre Anmutung, wie harmonisch die Figuren zueinander stehen und prüfe, wie breit oder schmal sie läuft. Ein Blindtext sollte möglichst viele verschiedene Buchstaben enthalten und in der Originalsprache gesetzt sein. Er muss keinen Sinn ergeben, sollte aber lesbar sein. Fremdsprachige Texte wie „Lorem ipsum“ dienen nicht dem eigentlichen Zweck, da sie eine falsche Anmutung vermitteln. Dies hier ist ein Blindtext zum Testen von Textausgaben. Wer diesen Text liest, ist selbst schuld. Der Text gibt lediglich den Grauwert der Schrift an. Ist

nicht dem eigentlichen Zweck, da sie eine falsche Anmutung vermitteln.

3.2 Computational methodology

The presented solver is embedded in the *BoSSS* (Bounded Support Spectral Solver) code, which is under development at the chair of fluid dynamics of the Technical University of Darmstadt, and is available under <https://github.com/FDYdarmstadt/BoSSS>. *BoSSS* is a general framework for the discretization of conservation laws using the DG method and uses a modal DG approach with orthonormal Legendre polynomials as basis functions. The *BoSSS* code features a variety of applications in the context of computational fluid dynamics, such as a solver for multiphase flows with a sharp interface approach, **kummerExtendedDiscontinuousGalerkin2017** an incompressible Immersed Boundary Method solver for particle laden flows, **krauseIncompressibleImmersedBounda** a solver for viscoelastic fluid flows, **kikkerFullyCoupledHighorder** and a solver for compressible flows, **geisenhoferDiscontinuousGalerkinImmersed2019** among others.

The variational problem for the finite chemistry rate case described by Equations (3.26a) to (3.26d) and for the flame sheet problem, Equations (3.27a) to (3.27c), are linearised and solved using a Newton method with a Dogleg-type globalization **pawlowskiGlobalizationTechniquesNewton2** **pawlowskiInexactNewtonDogleg2008**. The *BoSSS* framework provides an efficient algorithm for the evaluation of the Jacobian based on perturbations of the forms presented in the last section. The relatively large linear system of equations for each Newton iteration is solved by means of the in *BoSSS* integrated orthonormalization multigrid algorithm **kummerBoSSSPackageMultigrid2021**, which at the lowest multigrid levels makes use of the sparse direct solver PARDISO, originally developed by Schenk et al. **schenkEfficientSparseLU2000**; **schenkTwolevelDynamicScheduling2002**; **schenkSolvingUnsymmetricSparse2004a**, from the “Intel(R) Parallel Studio XE 2018 Update 3 Cluster Edition for Windows” library collection to solve the linear system.

BoSSS also features a method for solving highly nonlinear problems with a homotopy strategy. Further details on the used Newton method solver, the homotopy strategy and its implementation are given in the next sections, which are adapted from Kikker et al. **kikkerFullyCoupledHighorder** and are included for the sake of completeness. For information on the mentioned orthonormalization multigrid algorithm we refer the interested reader to the work of Kummer et al. **kummerBoSSSPackageMultigrid2021**

Calculation of the Jacobian matrix

We start by introducing a few new elements to be able to describe the implemented Newton method. The discussion for the variational problem using the mixture fraction variable (Equations (3.27a) to (3.27c)) is completely analogous, and will not be mentioned in this discussions. Find $\mathbf{U}_h \in \mathbb{V}_k$

$$\mathcal{N}(\mathbf{U}_h, \mathbf{V}_h) = 0 \quad \forall \mathbf{V}_h \in \mathbb{V}_k, \quad (3.43)$$

for $\mathbf{U}_h = (p_h, \mathbf{u}_h, T_h, \mathbf{Y}'_h)$ and $\mathbf{V}_h = (q_h, \mathbf{v}_h, r_h, \mathbf{s}_h)$. We assume a basis $\underline{\Phi} = (\Phi_1, \dots, \Phi_L)$ of \mathbb{V}_k , written as a row vector, with $L := \dim(\mathbb{V}_k)$. Then \mathbf{U}_h can be represented as $\mathbf{U}_h = \underline{\Phi} \cdot \mathbf{U}$. The nonlinear problem (3.43) can then be written as

$$\mathcal{A}(\mathbf{U}) = 0, \quad (3.44)$$

with the nonlinear function $\mathbb{R}^L \ni \mathbf{U} \mapsto \mathcal{A}(\mathbf{U}) \in \mathbb{R}^L$. The i -th component of $\mathcal{A}(\mathbf{U})$, can be defined by $\mathcal{N}(-, -)$ through the relation $[\mathcal{A}(\mathbf{U})]_i = \mathcal{N}(\underline{\Phi} \cdot \mathbf{U}, \Phi_i)$.

The formulation of the Newton method requires the Jacobian matrix $\partial\mathcal{A}$ of \mathcal{A} , defined as

$$\partial\mathcal{A}_{ij}(\mathbf{U}) := \frac{\partial\mathcal{A}_i}{\partial U_j}(\mathbf{U}). \quad (3.45)$$

Its computation is quite straightforward, but lengthy. The *BoSSS* code is capable of evaluating the Jacobian matrix automatically from the expressions given in Section 3.1.1. We note that one could write $\mathcal{A}(\mathbf{U})$ as

$$[\mathcal{A}(\mathbf{U})]_i = \mathcal{N}(\mathbf{U}_h, \Phi_i) = \int_{\Omega_h} N_1(\mathbf{x}, \mathbf{U}_h, \nabla\mathbf{U}_h) \cdot \Phi_i + N_2(\mathbf{x}, \mathbf{U}_h, \nabla\mathbf{U}_h) \cdot \nabla\Phi_i dV + \oint_{\Gamma} \dots dS. \quad (3.46)$$

The edge integral, which is left out in Equation (3.46), can be written in analogous fashion as the volume integral, i.e. as a sum over four nonlinear functions, multiplied by Φ_i^+ , Φ_i^- , $\nabla\Phi_i^+$ and $\nabla\Phi_i^-$, respectively. These functions themselves may depend on \mathbf{x} , \mathbf{U}_h^+ , \mathbf{U}_h^- , $\nabla\mathbf{U}_h^+$ and $\nabla\mathbf{U}_h^-$. For sake of compactness, this part is skipped. Realizing that $\frac{\partial\mathbf{U}_h}{\partial U_j} = \Phi_j$ and by application of the chain rule, one derives

$$\partial\mathcal{A}_{ij}(\mathbf{U}) = \int_{\Omega_h} (\partial_{\mathbf{U}_h} N_1(\mathbf{x}, \mathbf{U}_h, \nabla\mathbf{U}_h) \Phi_j + \partial_{\nabla\mathbf{U}_h} N_1(\mathbf{x}, \mathbf{U}_h, \nabla\mathbf{U}_h) \nabla\Phi_j) \cdot \Phi_i + \dots dV + \oint_{\Gamma} \dots dS. \quad (3.47)$$

All skipped terms in Equation (3.47) can be derived in an analogous fashion as the contributions for N_1 . In the *BoSSS* code, derivatives $\partial_{\mathbf{U}_h} N_1(\dots)$ and $\partial_{\nabla\mathbf{U}_h} N_1(\dots)$ are approximated by a finite difference, using a perturbation by $\sqrt{\text{eps}}$ in the respective argument, where $\text{eps} = 2.22044604925031 \cdot 10^{-16}$ is the floating point accuracy for double precision.

The notation introduced here allows us to describe the Newton-Dogleg method used in this work. We note however that this globalization strategy is still not sufficient to ensure convergence for some of the test cases presented, namely for high Rayleigh numbers for the differentially heated cavity problem. For those cases we use a homotopy strategy, where we start with a low homotopy-parameter, a parameter for which the solution of the problem is not hard to find, which is gradually and carefully increased until convergence for the desired value of the homotopy-parameter is reached (cf. Section 3.2.4).

3.2.1 Dogleg Method

We consider a linearization of Equation (3.44) around \mathbf{U}_n ,

$$\mathcal{A}(\mathbf{U}_n) + \partial\mathcal{A}(\mathbf{U}_n) \underbrace{(\mathbf{U}_{n+1} - \mathbf{U}_n)}_{=: \mathbf{s}'_n} = 0. \quad (3.48)$$

By repeatedly solving this system one obtains a standard Newton scheme for Equation (3.44), yielding a sequence of approximate solutions $\mathbf{U}_0, \mathbf{U}_1, \mathbf{U}_2, \dots$ obtained from an initial guess \mathbf{U}_0 through the iteration scheme $\mathbf{U}_{n+1} = \mathbf{U}_n + \mathbf{s}'_n$. In the classical un-damped Newton method, the correction step \mathbf{s}'_n is set to be the whole Newton-step, i.e. $\mathbf{s}'_n = \mathbf{s}_n$ with

$$\mathbf{s}_n := -\partial\mathcal{A}(\mathbf{U}_n)^{-1} \mathcal{A}(\mathbf{U}_n), \quad (3.49)$$

which is computed using a direct solver. Unfortunately, convergence of the Newton method for any starting value \mathbf{U}_0 is not guaranteed. In order to increase robustness when the distance between \mathbf{U}_0 and the exact solution \mathbf{U} is large, we employ a globalization approach, presented by

Pawlowski et al. **pawlowskiGlobalizationTechniquesNewton2006; pawlowskiInexactNewtonDogleg2008** known as the Dogleg-method, or Newton-Dogleg method. Here, we intend to give only the central ideas of method and refer to the original works for further details. Obviously, the exact solution of Equation (3.44) is also a minimum of the functional

$$f(\mathbf{U}) := \frac{1}{2} \|\mathcal{A}(\mathbf{U})\|_2^2. \quad (3.50)$$

One observes that $\nabla f(\mathbf{U}) = \partial \mathcal{A}(\mathbf{U})^T \mathcal{A}(\mathbf{U})$. For \mathbf{U}_n , the approximate Cauchy point with respect to the 2-norm, is defined as the minimizer \mathbf{g}_n of $\|\mathcal{A}(\mathbf{U}_n) + \partial \mathcal{A}(\mathbf{U}_n) \mathbf{g}_n\|_2$ in the direction of steepest decent, i.e. $\mathbf{g}_n = \lambda \nabla f(\mathbf{U}_n)$, $\lambda \in \mathbb{R}$. Substituting $\mathbf{w} := -\partial \mathcal{A}(\mathbf{U}_n) \nabla f(\mathbf{U}_n)$, \mathbf{g}_n is given by

$$\mathbf{g}_n = \frac{\mathcal{A}(\mathbf{U}_n) \cdot \mathbf{w}}{\mathbf{w} \cdot \mathbf{w}} \nabla f(\mathbf{U}_n). \quad (3.51)$$

For the Newton-Dogleg method, the correction step \mathbf{s}'_n is chosen along the so-called Dogleg curve, which is the piece-wise linear curve from the origin to \mathbf{g}_n and further to \mathbf{s}_n . The selection of \mathbf{s}'_n on this curve is determined by the trust-region diameter $\delta > 0$:

- If $\|\mathbf{s}_n\|_2 \leq \delta$, $\mathbf{s}'_n = \mathbf{s}_n$.
- If $\|\mathbf{g}_n\|_2 \leq \delta$ and $\|\mathbf{s}_n\|_2 > \delta$, \mathbf{s}'_n is chosen on the linear interpolation from \mathbf{g}_n to \mathbf{s}_n so that $\|\mathbf{s}'_n\|_2 = \delta$: For the ansatz $\mathbf{s}'_n = \tau \mathbf{s}_n + (1 - \tau) \mathbf{g}_n$, the interpolation factor τ is given as $\tau = (a^2 - c + \sqrt{(a^2 + b^2 - 2c)\delta^2 - a^2b^2 + c^2}) / (a^2 + b^2 - 2c)$ with $a = \|\mathbf{g}_n\|_2$, $b = \|\mathbf{s}_n\|_2$ and $c = \mathbf{g}_n \cdot \mathbf{s}_n$.
- If $\|\mathbf{g}_n\|_2 > \delta$, $\mathbf{g}_n = (\delta / \|\mathbf{g}_n\|_2) \mathbf{g}_n$.

The choice and adaptation of the trust region diameter δ throughout the Newton-Dogleg procedure follows a sophisticated heuristic, mainly based on comparing the actual residual reduction $\text{ared}_n := \|\mathcal{A}(\mathbf{U}_n)\|_2 - \|\mathcal{A}(\mathbf{U}_n + \mathbf{s}'_n)\|_2$ with the predicted residual reduction $\text{pred}_n := \|\mathcal{A}(\mathbf{U}_n)\|_2 - \|\mathcal{A}(\mathbf{U}_n) + \partial \mathcal{A}(\mathbf{U}_n) \mathbf{s}'_n\|_2$; For the direct solver used in this work pred_n simplifies to $\text{pred}_n := \|\mathcal{A}(\mathbf{U}_n)\|_2$. We replicate the algorithm here, for the sake of completeness:

- (1) Set $n = 0$, $\delta_n = \min(10^{10}, \max(2 \cdot 10^{-6}, \|\mathbf{s}_0\|_2))$.
- (2) Compute the Newton step \mathbf{s}_n and the Cauchy point \mathbf{g}_n and find \mathbf{s}'_n on the Dogleg curve with respect to the recent δ_n .
- (3) While $\text{ared}_n \leq \text{pred}_n$ do: Update trust region diameter $\delta_n \leftarrow 0.5 \delta_n$ and re-compute \mathbf{s}'_n . If $\delta_n < 10^{-6}$ terminate abnormally and mark the computation as failed.
- (4) If the convergence criterion (see below) is fulfilled, terminate and mark the computation as success.
- (5) Perform a final update of the trust region: Set

$$\delta_{n+1} = \begin{cases} \max(10^{-6}, \|\mathbf{s}_n\|_2) & \text{if } \text{ared}_n / \text{pred}_n < 0.1 \text{ and } \|\mathbf{s}_n\|_2 \delta_n \\ \max(10^{-6}, 0.25 \cdot \delta_n) & \text{else, if } \text{ared}_n / \text{pred}_n < 0.1 \\ \min(10^{10}, 4 \cdot \delta_n) & \text{else, if } \text{ared}_n / \text{pred}_n > 0.75 \\ \delta_n & \text{otherwise} \end{cases}$$

Set $\mathbf{U}_{n+1} = \mathbf{U}_n + \mathbf{s}'_n$, update $n \leftarrow n + 1$ and return to step (2).

All constants used in the algorithm above have been taken from the work of Pawlowski et al. **pawlowskiGlobalizationTechniquesNewton2006** For a detailed description of the underlying ideas we also refer to these works, which in turn are based on algorithms from Dennis and Schnabel's textbook. **dennisNumericalMethodsUnconstrained1996**

3.2.2 Termination criterion

A simple approach to determine that a Newton-Dogleg loop can be terminated is to check whether the residual norm has fallen below a certain threshold, i.e. $\|\mathcal{A}(U_n)\| \leq \text{tol}$. A universal choice for the tolerance is indeed difficult, especially for investigations of convergence properties (cf. Section 4.2.3 and Section 4.3.3). If it is chosen too low, the algorithm may never terminate, because of dominating numerical round-off errors. On the other hand, if it is chosen too high, the error of the premature termination may dominate the error of the spatial discretization and one cannot take the full advantage of the high-order method. Therefore the goal is to continue the Newton-Dogleg method until the lowest possible limit dictated by floating point accuracy is reached. To identify the limit in a robust way, we first define the residual-norm skyline as

$$\text{sr}_n := \min_{j \leq n} \|\mathcal{A}(\mathbf{U}_j)\| \quad (3.52)$$

and, for $n \geq 2$, the averaged reduction factor

$$\text{arf}_n := \frac{1}{2} \left(\frac{\text{sr}_{n-2}}{\max\{\text{sr}_{n-1}, 10^{-100}\}} + \frac{\text{sr}_{n-1}}{\max\{\text{sr}_n, 10^{-100}\}} \right). \quad (3.53)$$

The Newton-Dogleg method is terminated if

$$n \geq 2 \text{ and } \text{sr}_n \leq 10^{-5} + 10^{-5} \|\mathbf{U}_n\|_2 \text{ and } \text{arf}_n < 1.5. \quad (3.54)$$

For the computations in this work, this choice guarantees that the nonlinear system is solved as accurately as possible. It secures that the numerical error is dominated by the error of the spatial or temporal discretization and not by the termination criterion of the Newton-Dogleg method. The skyline approach ensures robustness against oscillations close to the lower limit.

3.2.3 Solver safeguard

3.2.4 Homotopy method

Although the Newton-Dogleg method works well for a variety of cases, we experienced convergence problems for some of the test cases presented in next section. In particular, for the differentially heated cavity test case, the method was not successful on finding a convergent solution for a Rayleigh number $Ra \geq 10^5$ within 60 Newton iterations. In such cases we used a homotopy strategy, which is loosely based on ideas from the textbook of Deuflhard, **deuflhardNewtonMethodsNonlinear2011** Chapter 5.

We start by identifying a parameter that makes the solution of the nonlinear problem difficult to solve. In the following we will refer to this variable as the homotopy parameter. The main idea of the homotopy strategy consists of solving a series of simpler problems, starting with a parameter where the problem is easy to solve, and carefully increasing it until the desired value is reached. Let Hp denote the value of the homotopy parameter for which a solution is being sought. Let

$$\mathcal{A}_{\text{hp}^*}(\mathbf{U}) = 0 \quad (3.55)$$

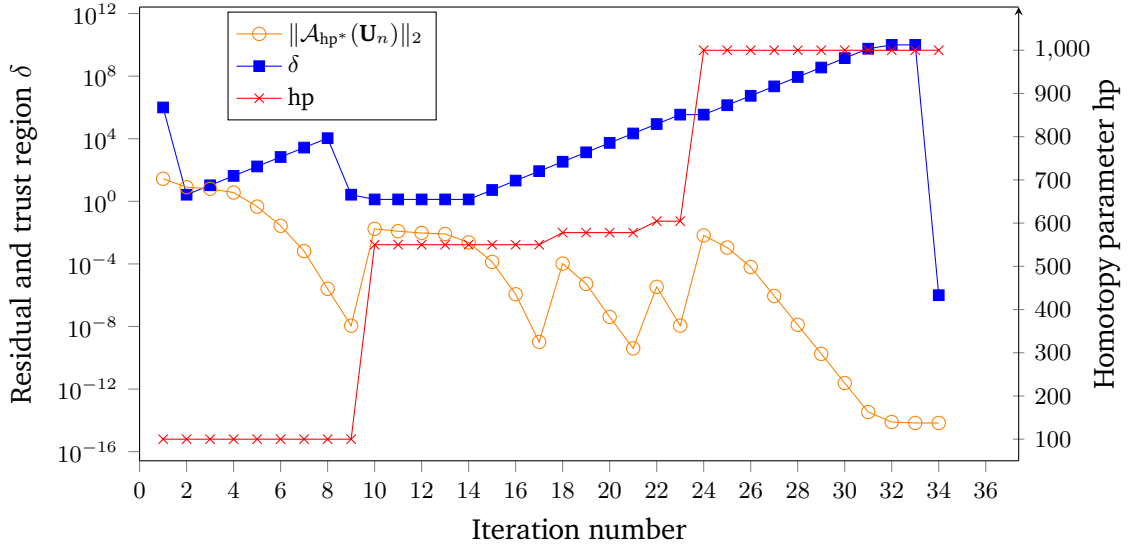


Figure 3.1: Behaviour of the homotopy method for the differentially heated cavity test case. The homotopy parameter hp in this case is the Reynolds number.

be the discretized system for a certain intermediate homotopy-parameter hp^* , between 0 and the ‘target’ homotopy-parameter Hp , i.e. $0 \leq hp^* \leq Hp$. Furthermore, let $\mathbf{U}_{hp,\epsilon}$ be an approximate solution to the problem (3.55) with $hp^* = hp$, up to a tolerance ϵ , i.e.

$$\|\mathcal{A}_{hp}(\mathbf{U}_{hp,\epsilon})\|_2 \leq \epsilon. \quad (3.56)$$

For the sake of clarity when discussing the algorithm which follows below, we distinguish between the intermediate homotopy-parameter hp for which we assume to already have found an acceptable solution and the next homotopy-parameter hp^* that we are currently trying to find a solution for. For any $hp^* > hp$ we set $\epsilon = 10^{-5} \|\mathcal{A}_{hp^*}(\mathbf{U}_{hp,\epsilon})\|_2$, i.e. we aim for a residual norm reduction of at least five orders of magnitude with respect to the initial residual norm. If $hp^* = Hp$, the termination criterion presented in section 3.2.2 is applied. An approximate solution for the target homotopy-parameter is found by the following recipe:

- (1) Set $hp = 0$, i.e. start by obtaining an (approximate) solution $\mathbf{U}_{0,\epsilon}$.
- (2) Search for a an increased homotopy-parameter hp^* : Find the minimal $i \geq 0$ so that for $hp^* = \frac{1}{2^i}(Hp - hp) + hp$ one has $\|\mathcal{A}_{hp^*}(\mathbf{U}_{hp,\epsilon})\|_2 \leq \delta_{\max} \|\mathcal{A}_{hp}(\mathbf{U}_{hp,\epsilon})\|_2$. Here, δ_{\max} is the maximal allowed increase of the residual for an increased homotopy-parameter hp^* ; δ_{\max} is adapted in the following steps, as an initial guess we use $\delta_{\max} = 10^6$.
- (3) Use the Newton-Dogleg method to compute an approximate solution to the problem (3.55), for the homotopy-parameter hp^* , using the solution $\mathbf{U}_{hp,\epsilon}$ as an initial guess.
 - If the Newton-Dogleg method did not converge successfully within ten steps, the homotopy-parameter increase from hp to hp^* was probably too large. Set $\delta_{\max} \leftarrow 0.2\delta_{\max}$ and go to step (2).
 - If the Newton-Dogleg method reached its convergence criterion and if the target homotopy-parameter is reached, i.e. $hp^* = Hp$, the algorithm has successfully found an approximate solution for $\mathcal{A}_{Hp}(\mathbf{U}) = 0$ and can terminate.

- Otherwise, if the Newton-Dogleg method converged successfully, but is below the target homotopy-parameter: Accept the solution and set $hp \leftarrow hp^*$. If the Newton-Dogleg method took less than three iterations to reach the convergence criterion, set $\delta_{\max} \leftarrow 8\delta_{\max}$. Return to step (2).

An exemplary run of the method is shown in Figure 3.1. The homotopy parameter hp in this particular case is the Reynolds number. The homotopy-parameter hp was increased for iterations 10, 18, 22 and 24, causing an increase of the residuals $\|\mathcal{A}_{hp^*}(\mathbf{U}_n)\|_2$, leading to a convergent solution after 34 Newton iterations. The presented algorithm offers a robust method for finding steady-state solutions of highly nonlinear systems.

3.2.5 Initialization of combustion applications

Cases involving combustion are initialized with the solution of the flame sheet problem, Equations (3.27a) to (3.27c). This idea has been already employed in various works. **smookeNumericalSolutionTwoD** **smookeNumericalModelingAxisymmetric1992** The reason for the use of this pre-step is twofold:

- Solving ??? and Equations (2.22c) and (2.22d) using a Newton-type method requires adequate starting estimates in order to converge. Using the flame sheet solution as initial estimate improves the convergence properties of the method.
- The system of ??? and Equations (2.22c) and (2.22d) possesses multiple solutions. One is the pure mixing (frozen) solution, where no chemical reaction has taken place, and the other one is the ignited solution, where the flame is present. Using the flame sheet solution as initial estimate ensures that the path taken by Newton's algorithm will tend towards the ignited solution.

We remark at this point that although for the solution of the flame sheet system the mixture heat capacity has been assumed to be constant, it remains an adequate estimate for the finite reaction-rate problem, where the heat capacity is a function of temperature and local concentration. In a similar fashion, the assumption of unity Lewis number in the flame sheet system delivers a solution that slightly deviates from the solution of the finite chemistry rate problem with non-unity Lewis numbers. Nevertheless, this small deviation does not preclude the use of the flame sheet solution as an adequate initial estimate for Newton's method.

Regarding the solution of the flame sheet problem (cf. Section 2.2), it should be noted that the sharp change in the primitive variables around $z = z_{st}$ could be problematic. In particular, the non-smoothness of the derived variables could lead to Gibbs phenomenon-type problems. This inconvenient can be remedied by using a regularized form of the equations. We define the smoothing function \mathcal{H}

$$\mathcal{H}(z) \approx \frac{1}{2} \left(1 + \tanh\left(\frac{z - z_{st}}{\sigma}\right) \right), \quad (3.57)$$

The parameter σ dictates the sharpness of the transition at $z = z_{st}$. In Figure 3.2 the effect of the smoothing factor σ on calculations of a flame in a counter-flow configuration are shown. It can be clearly observed how for increasing σ the solution becomes smoother. Using Equation (3.57) the temperature and mass fraction fields can be written as

$$T(z) = zT_F^0 + (1 - z)T_O^0 + \frac{QY_F^0}{c_p} z_{st} \frac{1 - z}{1 - z_{st}} \mathcal{H}(z) + \frac{QY_F^0}{c_p} z (1 - \mathcal{H}(z)), \quad (3.58)$$

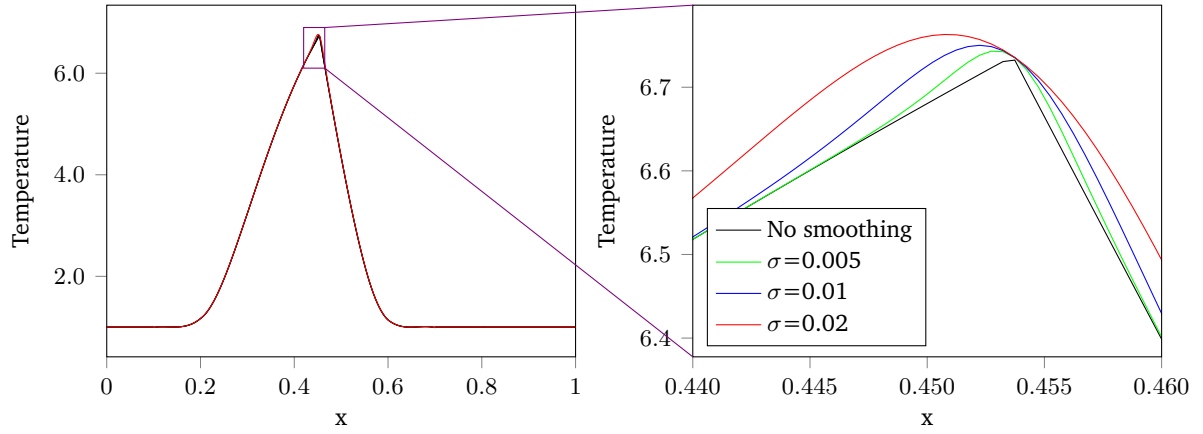


Figure 3.2: Temperature profile calculated in the center-line of a counter-flow flame configuration for different smoothing parameters σ .

$$Y_F(z) = Y_F^0 \frac{z - z_{st}}{1 - z_{st}} \mathcal{H}(z), \quad (3.59)$$

$$Y_O(z) = Y_O^0 \frac{z_{st} - z}{z_{st}} (1 - \mathcal{H}(z)), \quad (3.60)$$

$$Y_P(z) = Y_O^0 \frac{M_P \nu_P}{M_O \nu_O} (1 - z) \mathcal{H}(z) + Y_F^0 \frac{M_P \nu_P}{M_F \nu_F} z (1 - \mathcal{H}(z)). \quad (3.61)$$

$$Y_N(z) = (1 - Y_F^0)z + (1 - Y_O^0)(1 - z). \quad (3.62)$$

The use of this regularized form of the equations results in practice on a spreading of the flame front, which eases the numerical calculation (**braackAdaptiveFiniteElement1997**).

We note at this point that Equation (2.20) yields unphysical values of \hat{Q} for large values of ϕ . This problem can be avoided by setting an upper boundary value for ϕ in Equation (2.20) (we use $\phi = 1.2$). In practice however, this should not have a significant effect, because the unphysical values of \hat{Q} appear at zones where the reaction rate $\hat{\omega}$ is very close to zero, making the factor $\hat{Q}\hat{\omega}$ in the temperature equation negligible. Nevertheless, setting an upper bound for ϕ is helpful to avoid possible numerical instabilities.

Adaptive Mesh Refinement

4 Results

The following sections will present the results obtained using the previously exposed solver in a variety of benchmark cases. The chosen test cases will be presented incrementally in complexity. In section Section 4.2.2 a Couette flow presenting a temperature gradient in the vertical direction is studied. (Subsequently in section XX the temporal discretization is studied using the traditional Taylor-Green vortex.) In Section 4.2.3 a heated square cavity configuration is studied in order to assess the capability of the solver for variable density flows in closed systems. Later in in Section 4.3.2 and ?? two different configurations for reactive flows are presented.

All calculations shown here where performed on AMD EPYC 7543 32-Core Processor, DDR4

4.1 Single-component isothermal cases

4.1.1 Transpiring Channel?

Dies hier ist ein Blindtext zum Testen von Textausgaben. Wer diesen Text liest, ist selbst schuld. Der Text gibt lediglich den Grauwert der Schrift an. Ist das wirklich so? Ist es gleichgültig, ob ich schreibe: „Dies ist ein Blindtext“ oder „Huardest gefburn“? Kjift – mitnichten! Ein Blindtext bietet mir wichtige Informationen. An ihm messe ich die Lesbarkeit einer Schrift, ihre Anmutung, wie harmonisch die Figuren zueinander stehen und prüfe, wie breit oder schmal sie läuft. Ein Blindtext sollte möglichst viele verschiedene Buchstaben enthalten und in der Originalsprache gesetzt sein. Er muss keinen Sinn ergeben, sollte aber lesbar sein. Fremdsprachige Texte wie „Lorem ipsum“ dienen nicht dem eigentlichen Zweck, da sie eine falsche Anmutung vermitteln. Dies hier ist ein Blindtext zum Testen von Textausgaben. Wer diesen Text liest, ist selbst schuld. Der Text gibt lediglich den Grauwert der Schrift an. Ist das wirklich so? Ist es gleichgültig, ob ich schreibe: „Dies ist ein Blindtext“ oder „Huardest gefburn“? Kjift – mitnichten! Ein Blindtext bietet mir wichtige Informationen. An ihm messe ich die Lesbarkeit einer Schrift, ihre Anmutung, wie harmonisch die Figuren zueinander stehen und prüfe, wie breit oder schmal sie läuft. Ein Blindtext sollte möglichst viele verschiedene Buchstaben enthalten und in der Originalsprache gesetzt sein. Er muss keinen Sinn ergeben, sollte aber lesbar sein. Fremdsprachige Texte wie „Lorem ipsum“ dienen nicht dem eigentlichen Zweck, da sie eine falsche Anmutung vermitteln. Dies hier ist ein Blindtext zum Testen von Textausgaben. Wer diesen Text liest, ist selbst schuld. Der Text gibt lediglich den Grauwert der Schrift an. Ist das wirklich so? Ist es gleichgültig, ob ich schreibe: „Dies ist ein Blindtext“ oder „Huardest gefburn“? Kjift – mitnichten! Ein Blindtext bietet mir wichtige Informationen. An ihm messe ich die Lesbarkeit einer Schrift, ihre Anmutung, wie harmonisch die Figuren zueinander stehen und prüfe, wie breit oder schmal sie läuft. Ein Blindtext sollte möglichst viele verschiedene Buchstaben enthalten und in der Originalsprache gesetzt sein. Er muss keinen Sinn ergeben, sollte aber lesbar sein. Fremdsprachige Texte wie „Lorem ipsum“ dienen nicht dem eigentlichen Zweck, da sie eine falsche Anmutung vermitteln. Dies hier ist ein Blindtext

4.1.2 Taylor-Green vortex

32

Informationen. An ihm messe ich die Lesbarkeit einer Schrift, ihre Anmutung, wie harmonisch die Figuren zueinander stehen und prüfe, wie breit oder schmal sie läuft. Ein Blindtext sollte möglichst viele verschiedene Buchstaben enthalten und in der Originalsprache gesetzt sein. Er muss keinen Sinn ergeben, sollte aber lesbar sein. Fremdsprachige Texte wie „Lorem ipsum“ dienen nicht dem eigentlichen Zweck, da sie eine falsche Anmutung vermitteln. Dies hier ist ein Blindtext zum Testen von Textausgaben. Wer diesen Text liest, ist selbst schuld. Der Text gibt lediglich den Grauwert der Schrift an. Ist das wirklich so? Ist es gleichgültig, ob ich schreibe: „Dies ist ein Blindtext“ oder „Huardest gefburn“? Kjift – mitnichten! Ein Blindtext bietet mir wichtige Informationen. An ihm messe ich die Lesbarkeit einer Schrift, ihre Anmutung, wie harmonisch die Figuren zueinander stehen und prüfe, wie breit oder schmal sie läuft. Ein Blindtext sollte möglichst viele verschiedene Buchstaben enthalten und in der Originalsprache gesetzt sein. Er muss keinen Sinn ergeben, sollte aber lesbar sein. Fremdsprachige Texte wie „Lorem ipsum“ dienen nicht dem eigentlichen Zweck, da sie eine falsche Anmutung vermitteln.

4.1.3 Backward-facing step

The backward-facing step problem is a classical configuration widely used for validation of CFD codes. In this section we shall present the results that intend to reproduce the conclusions of the numerical experiments presented in **biswasBackwardFacingStepFlows2004**.

In Figure 5.1 a schematic representation of the problem is shown.

Although The backward-facing step problem is known to be inherently three-dimensional, it has been shown that it can be studied as a two-dimensional configuration along the symmetry plane for moderate Reynolds numbers (**barkleyThreedimensionalInstabilityFlow2000**; **biswasBackwardFacingStepFlows2004**). For the range of Reynolds numbers used in our calculations the two-dimensional assumption is justified. The origin of the coordinate system is set at the bottom part of the step. The step height S and channel height h characterize the system. The results on the literature are often reported as a function of the expansion ratio, defined as $ER = (h + S)/h$. We conduct a series of simulations with the objective of reproducing the results reported in **biswasBackwardFacingStepFlows2004**, where the backward-facing step was calculated for Reynolds numbers up to 400 and for an expansion ratio of 1.9423. The Reynolds number for the backward-facing step configuration is defined in the literature in many forms. We adopt here the definition based on the step height S and mean inlet velocity U_{mean} as reference values, resulting in

$$Re = \frac{SU_{\text{mean}}}{\nu} \quad (4.1)$$

The system is isothermic and the fluid is assumed to be air. The inlet profile is parabolic and is given by

$$u(y) = -6U_{\text{mean}} \frac{(y - S)(y - (h + S))}{h^2} \quad (4.2)$$

In order to minimize the effects of the outlet boundary condition in the system, the length L of the domain was set to $L = 70S$. Additionally $L_0 = S$. For all calculations in this section a structured grid with 88400 elements is used. To better resolve the complex structures that occur in this configuration, smaller elements are used in the vicinity of the step, as seen in figure Figure 4.2.

The backward-facing step configuration exhibits varying behaviour as the number of Reynolds changes. At small Reynolds number, a single vortex, usually called the primary vortex, appears

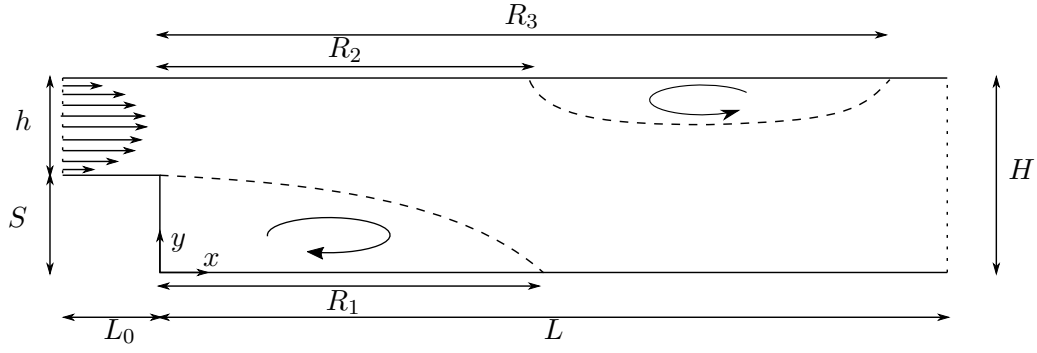


Figure 4.1: Schematic representation of the backward-facing step. Both primary and secondary vortices are shown. Sketch is not to scale.

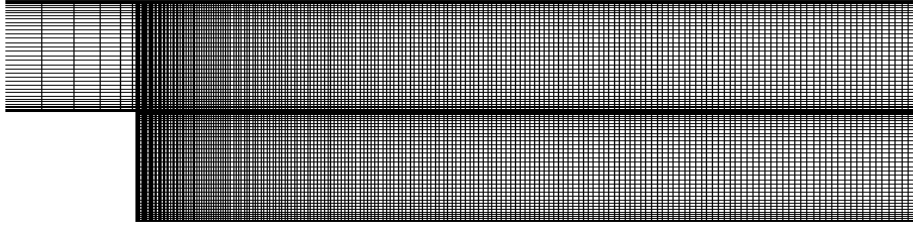


Figure 4.2: Structured mesh used in all calculations.

in the vicinity of the step. In addition, as the Reynolds number increases, a second vortex eventually appears on the top wall, as is shown schematically in Figure Figure 5.1. The deattachment and reattachment lengths of the vortices are values usually reported in the literature. It is possible to determine the position of deattachment by finding the point along the wall where the velocity gradient u acquires a value equal to zero. Figure Figure 4.3 shows the deattachment and reattachment lengths of the primary and secondary vortices obtained with our code for different Reynolds numbers, which are also compared with the results presented in the reference **biswasBackwardFacingStepFlows2004**. It can be observed how the results for the deattachment lengths of the primary vortex present very good agreement with those of the reference. In the case of the secondary vortex it is possible to see a very minimal deviation for the reattachment lengths. It is interesting to note that despite the fact that the reference does not report the existence of a secondary vortex for $Re = 200$, with our code it was possible to observe it. The results allow us to conclude that it is possible to study flows with complex behavior for high Reynolds numbers, at least in the isothermal case. In the next section we will discuss what happens for the non-isothermal case.

4.2 Single-component non-isothermal cases

4.2.1 Heated backward-facing step

As an extension to the previous case, we seek to recreate the results presented in **xieFluidFlowHeat2016**, where the same backward-facing step configuration as presented above is studied, but with the particularity that in this case the bottom wall is heated to a constant temperature, thus featuring

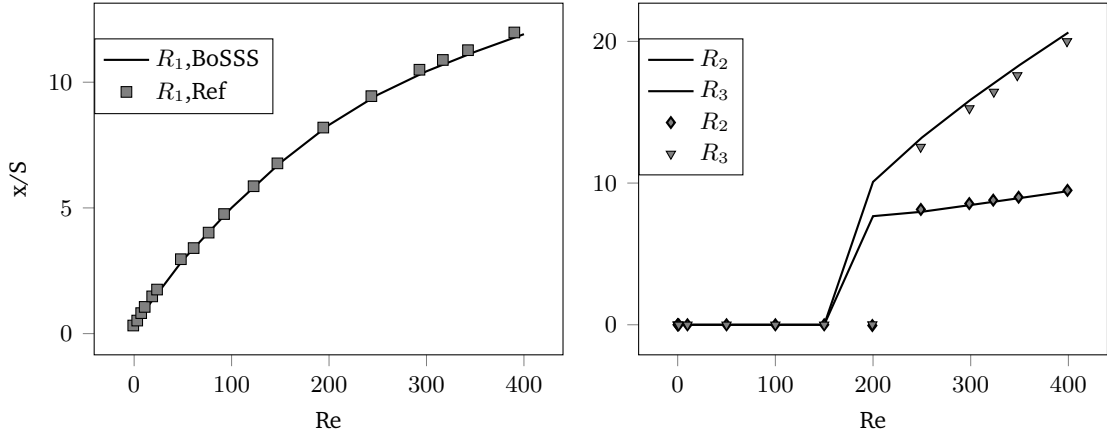


Figure 4.3: Detachment and reattachment lengths of the primary (left figure) and secondary (right figure) recirculation zones after the backward-facing step. Solid lines correspond to the results obtained with BoSSS and the marks to the reference solution (biswasBackwardFacingStepFlows2004).

a non-isothermal system. The fluid entering the system has a temperature equal to $T_0 = 10^\circ C$ and the bottom wall is set to a constant temperature of $T_1 = 40^\circ C$. In **xieFluidFlowHeat2016** results are reported for the local Nusselt numbers and local friction coefficients f_d along the bottom wall for different expansion ratios and Reynolds numbers. The local Nusselt number is defined as

$$Nu = \frac{S}{T_0 - T_1} \nabla T \cdot \mathbf{n} \quad (4.3)$$

On the other hand, and by recognizing that the wall shear stress along the bottom wall $\tau_w = -\mu \nabla u \cdot \mathbf{n}$, the local friction factor can be written as

$$f_d = \frac{8\nu}{(U_{\text{mean}})^2} \nabla u \cdot \mathbf{n} \quad (4.4)$$

A series of simulations for varying Reynolds numbers and expansion ratios were conducted. In Figure 4.4 the temperature field and streamlines corresponding to a calculation with $Re = 700$ is shown. Here the apparition of the secondary vortex is appreciated. We point out here that the results obtained by us are substantially different from those reported in **xieFluidFlowHeat2016**, and will not be shown here. Nevertheless, in the work of **henninkLowMachNumberFlow2022** the same is also pointed out, saying that with his method it was not possible to reproduce the results presented by **xieFluidFlowHeat2016**. Comparing our results with those of Hennink we can see that the same results are obtained, as demonstrated in Figure 4.5.

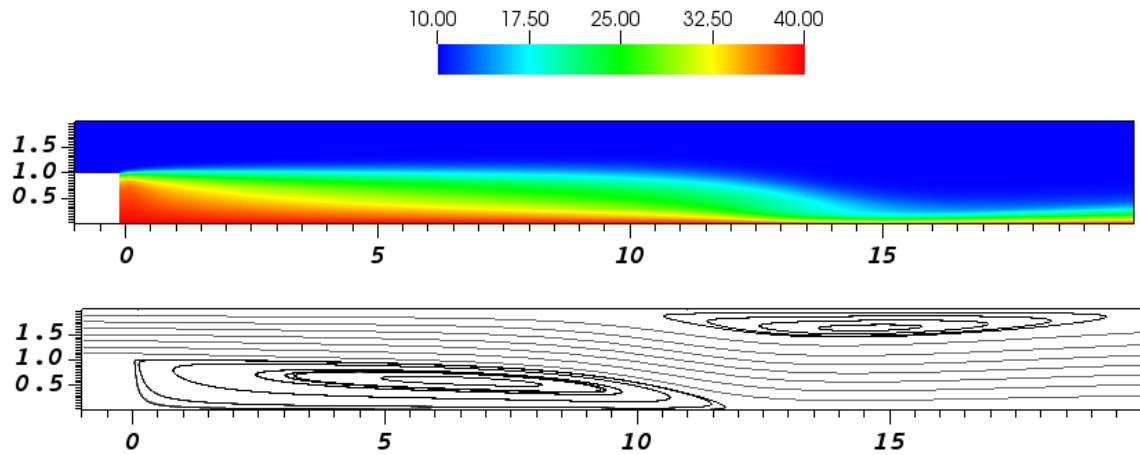


Figure 4.4: Temperature profile (top) and streamlines (bottom) corresponding to the backward-facing Step configuration for $Re = 400$ and an expansion ratio of two.

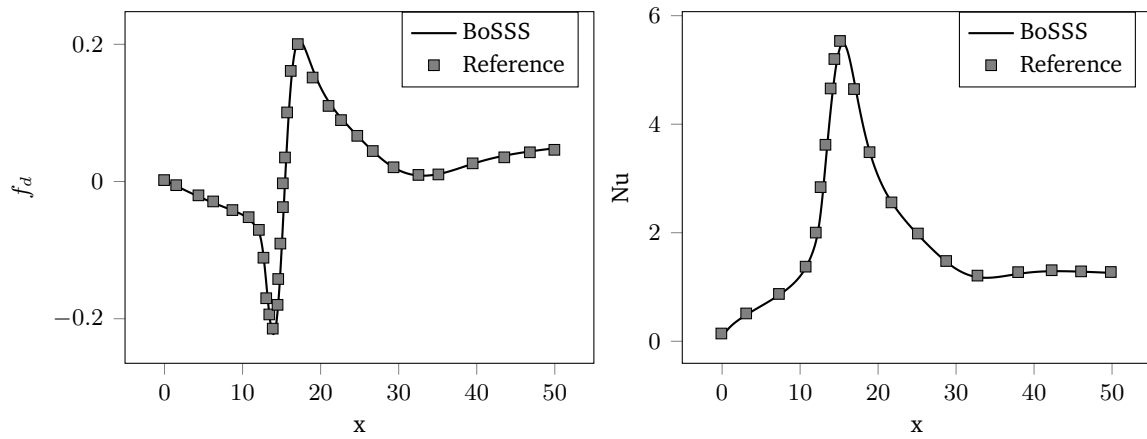


Figure 4.5: Local friction factor and local Nusselt number along the bottom wall for $Re = 700$ and an expansion ratio of two. The solid lines corresponds to our solution and the marks to the reference `henninkLowMachNumberFlow2022`

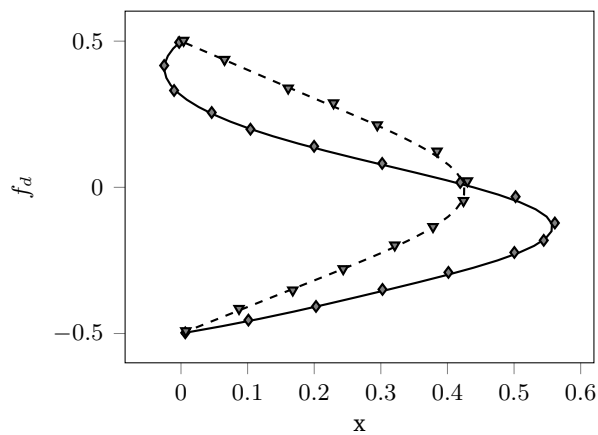


Figure 4.6: bla

4.2.2 Couette flow with vertical temperature gradient

As a first benchmark case to test the implemented low-Mach solver we analyse the Couette flow with a vertical temperature gradient. This configuration was already studied in (kleinHighorderDiscontinuousGalerkin2016), where the SIMPLE algorithm in a DG framework was used. We intend in this section to reproduce their results by using our fully coupled solver. We also show later how our implemented solver performs in relation to the SIMPLE based solver.

In Figure 4.7 a schematic representation of the testcase is shown. The top wall corresponds to a moving wall ($u = 1$) with a fixed temperature $T = T_h$. The bottom wall is a static one ($u = 0$), and has a constant temperature $T = T_c$. The domain is chosen as $\Omega = [0, 1] \times [0, 1]$, and Dirichlet boundary conditions are used for all boundaries. It is assumed that the fluid is composed of only one component, thus $N = 1$ and we can prescribe $Y_0 = 1.0$ everywhere in the domain. Additionally, the system is subjected to a gravitational field, where the gravity vector only has a component in the y direction. Under this conditions, the x-velocity, pressure and temperature are only dependent on the y coordinate, i.e. $u = u(y)$, $T = T(y)$ and $p = p(y)$. Thus, the governing equations (Equation (2.1)) reduce to

$$\frac{1}{\text{Re}} \frac{\partial}{\partial y} \left(\mu \frac{\partial u}{\partial y} \right) = 0, \quad (4.5)$$

$$\frac{\partial p}{\partial y} = -\frac{\rho}{\text{Fr}^2}, \quad (4.6)$$

$$\frac{1}{\text{Re Pr}} \frac{\partial}{\partial y} \left(\lambda \frac{\partial T}{\partial y} \right) = 0. \quad (4.7)$$

It is possible to find an analytical solution for this problem. By assuming a temperature dependence of the transport properties according a Power Law ($\mu = \lambda = T^{2/3}$) a solution is

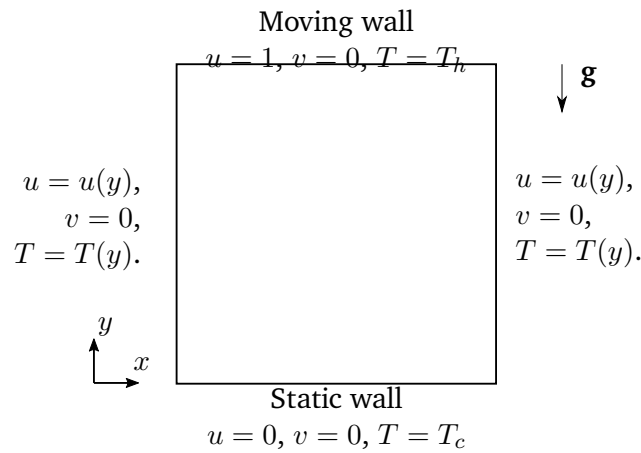


Figure 4.7: Schematic representation of the couette flow with temperature difference test case.

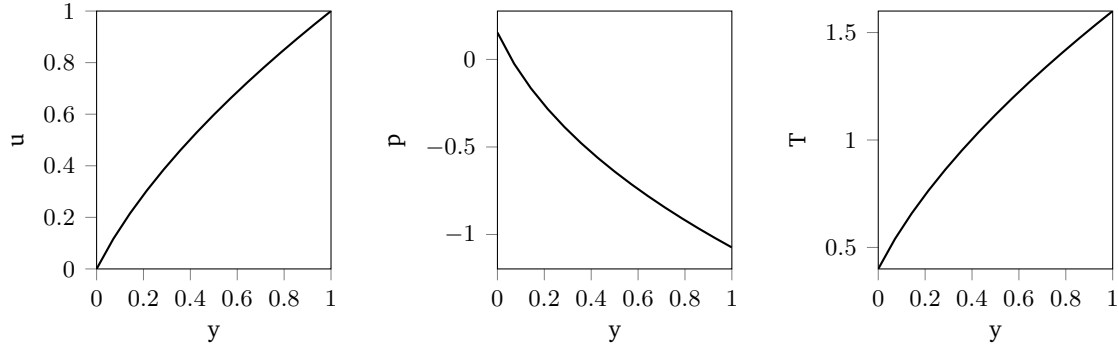


Table 4.1: Solution of the Couette flow with vertical temperature gradient. Viscosity and heat conductivity are calculated with a Power-Law.

obtained as

$$u(y) = C_1 + C_2 \left(y + \frac{T_c^{5/3}}{T_h^{5/3} - T_c^{5/3}} \right)^{3/5}, \quad (4.8)$$

$$p(y) = -\frac{5p_0}{2\text{Fr}^2} \frac{\left(y \left(T_h^{5/3} - T_c^{5/3} \right) + T_c^{5/3} \right)^{2/5}}{\left(T_h^{5/3} - T_c^{5/3} \right)} + C, \quad (4.9)$$

$$T(y) = \left(C_3 - \frac{5}{3} C_4 y \right)^{3/5}. \quad (4.10)$$

Where the constants C_1 , C_2 , C_3 and C_4 are determined by using the boundary conditions on the top and bottom walls, and are given by

$$C_1 = \frac{\left(\frac{T_c^{5/3}}{T_h^{5/3} - T_c^{5/3}} \right)^{3/5}}{\left(\frac{T_c^{5/3}}{T_h^{5/3} - T_c^{5/3}} \right)^{3/5} - \left(\frac{T_h^{5/3}}{T_h^{5/3} - T_c^{5/3}} \right)^{3/5}} \quad (4.11)$$

$$C_2 = \frac{1}{\left(\frac{T_h^{5/3}}{T_h^{5/3} - T_c^{5/3}} \right)^{3/5} - \left(\frac{T_c^{5/3}}{T_h^{5/3} - T_c^{5/3}} \right)^{3/5}} \quad (4.12)$$

$$C_3 = T_c^{5/3}, \quad (4.13)$$

$$C_4 = \frac{3}{5} \left(T_c^{5/3} - T_h^{5/3} \right) \quad (4.14)$$

and again C is a real-valued arbitrary constant for the pressure.

For all calculations of this configuration shown in the following sections the dimensionless parameters are set as $\text{Re} = 10$ and $\text{Pr} = 0.71$, $T_h = 1.6$ and $T_c = 0.4$. Since we are dealing with an open system we set $p_0 = 1.0$. The Froude number is calculated as

$$\text{Fr} = \left(\frac{2\text{Pr}(T_h - T_c)}{(T_h + T_c)} \right)^{1/2} \quad (4.15)$$

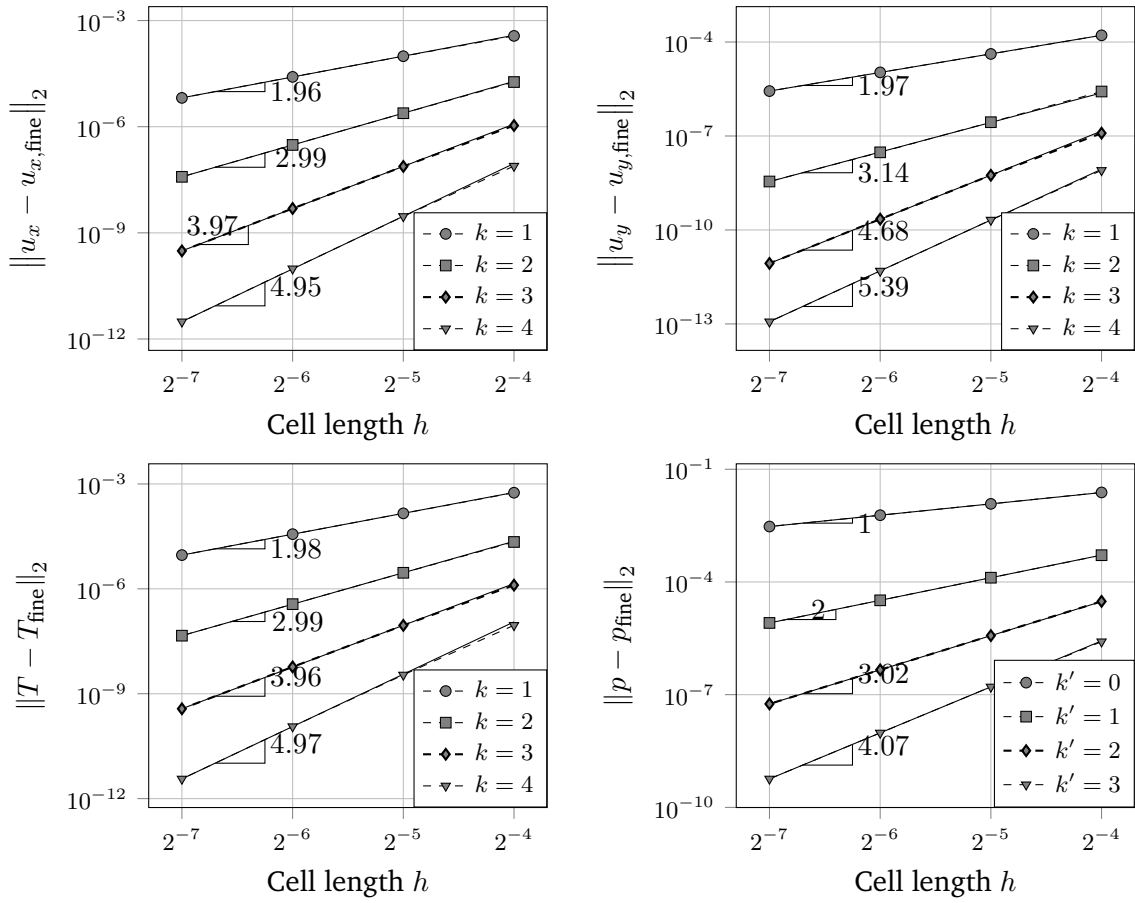


Figure 4.8: Convergence study of the differentially heated cavity problem for $Ra = 10^3$.

In Table 4.1 the solution for the velocity, pressure and temperature are shown. The results are for a mesh with 26×26 elements and a polynomial degree of three for u and T , and a polynomial degree of two for p .

h-convergence study

The convergence properties of the DG method for this non-isothermic system was studied using the analytical solution described before. The domain is discretized and solved in uniform Cartesian meshes with 16×16 , 32×32 , 64×64 and 128×128 elements. The polynomial degrees for the velocity and temperature are changed from 1 to 4 and for the pressure from 0 to 3. The convergence criteria described in Section 3.2.2 was used for all calculations. The analytical solution given by Equations (4.8) to (4.10) are as Dirichlet boundary conditions on all boundaries of the domain. The error is calculated against the analytical solution using the L^2 norm In Figure 4.15 the results of the h-convergence study are shown. We observe how the expected convergence rates are reached for all variables, namely a slope of the order $k + 1$ for both velocity components and the temperature, and a slope of $k' + 1$ for the pressure.

Comparison with SIMPLE

As mentioned before, a solver for solving low-Mach flows based on the SIMPLE algorithm (presented in **kleinHighorderDiscontinuousGalerkin2016**) has been already developed and implemented within the BoSSS framework. Though the solver was validated and shown to be useful for a wide variety of test cases, there were also disadvantages inherently associated with the SIMPLE algorithm. Within the solution algorithm, Picard-type iterations are used to search for a solution. This requires some prior knowledge from the user in order to select suitable relaxation factor values that provide stability to the algorithm, but at the same time do not slow down the computation substantially. It was also observed that the calculation times were prohibitively high for some test cases. This point motivated the development of the solver presented in the present work, where the system is solved in a monolytic way and the Newton method globalized with a Dogleg-type method is used to solve the system. We intend to show in this section a comparison of runtimes of the calculation of the Couette flow with vertical temperature gradient between the DG-SIMPLE algorithm (**kleinHighorderDiscontinuousGalerkin2016**) and the present solver (denoted here as XNSEC). Calculations were performed on uniform Cartesian meshes with 16×16 , 32×32 , 64×64 and 128×128 elements, and with varying polynomial degrees between 1 and 3 for the velocity and temperature, and between 0 and 2 for the pressure. All calculations were initialized with a zero velocity and pressure field, and with a temperature equal to one in the whole domain. All calculations were performed single-core and the convergence criteria is set to 10^{-8} for both solvers. The under-relaxation factors for the SIMPLE algorithm were set for all calculations to 0.8, 0.5 and 1.0 for the velocity, pressure and temperature, respectively.

In figure Table 4.2 a comparison of the runtimes from both solvers is shown. It is clearly appreciated how the runtimes of the SIMPLE algorithm are higher for almost all of the cases studied. Obviously the under-relaxation parameters of the SIMPLE algorithm have an influence on the calculation times and an appropriate selection of them could decrease the runtimes. This is a clear disadvantage, because the selection of adequate factors is highly problem dependent and requires some previous expertise from the user. On the other hand, the globalized Newton method used by the XNSEC avoids this problem by using a more sophisticated method and heuristics in order to find a better path to the solution.

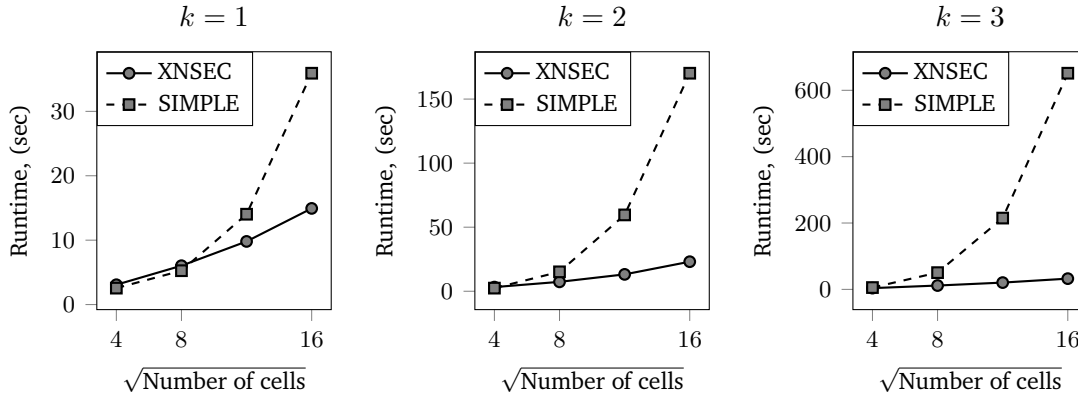


Table 4.2: Runtime comparison of the DG-SIMPLE algorithm (kleinHighorderDiscontinuousGalerkin2016) and the present solver (XNSEC) for the Couette flow with vertical temperature gradient configuration

4.2.3 Differentially heated cavity problem

The differentially heated cavity problem corresponds to a classical benchmark case often used to assess the capability of numerical codes to simulate variable density flows. paillereComparisonLowMach2000; vierendeelsBenchmarkSolutionsNatural2003; tyliszczakProjectionMethodHighorder2014 In this section, we show the basic set-up and compare our results with the ones presented in the work of Vierendeels et al. vierendeelsBenchmarkSolutionsNatural2003 where benchmark solutions for the differentially heated cavity are presented. They solve the fully compressible Navier-Stokes equations on a 1024×1024 stretched grid using a Finite Volume Method with quadratic convergence.

The differentially heated cavity problem consists of a two-dimensional fully enclosed square cavity filled with fluid. A sketch of the problem is shown in Figure 4.9. The left and right walls of the cavity have a constant temperature \hat{T}_h and \hat{T}_c respectively, with $\hat{T}_h > \hat{T}_c$, and the top and bottom walls are adiabatic. A gravity field induces fluid movement due to the density differences caused by the difference of temperature between the hot and cold walls.

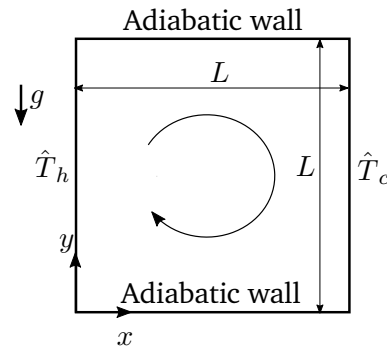


Figure 4.9: Schematic representation of the differentially heated cavity problem.

The natural convection phenomenon is characterized by the Rayleigh number, defined as

$$\text{Ra} = \text{Pr} \frac{\hat{g} \hat{\rho}_{\text{ref}}^2 (\hat{T}_h - \hat{T}_c) \hat{L}_{\text{ref}}^3}{\hat{T}_{\text{ref}} \hat{\mu}_{\text{ref}}^2}, \quad (4.16)$$

For small values of Ra, conduction dominates the heat transfer process, and a boundary layer covers the whole domain. On the other hand large values of Ra represent a convection dominated flow. For increasing Ra number, a thinner boundary layer is formed.

Set-up A reference velocity for buoyancy driven flows can be defined as **vierendeelsBenchmarkSolutionsNatural2003**

$$\hat{u}_{\text{ref}} = \frac{\sqrt{\text{Ra}} \hat{\mu}_{\text{ref}}}{\hat{\rho}_{\text{ref}} \hat{L}_{\text{ref}}}. \quad (4.17)$$

The Rayleigh number is then related to the Reynolds number according to

$$\text{Re} = \sqrt{\text{Ra}}. \quad (4.18)$$

Thus it is sufficient to select a Re number in our simulation, fixing the value of the Ra number. The driving temperature difference $(\hat{T}_h - \hat{T}_c)$ appearing in Equation (4.16) can be represented as an non-dimensional parameter:

$$\varepsilon = \frac{\hat{T}_h - \hat{T}_c}{2\hat{T}_{\text{ref}}}. \quad (4.19)$$

Using these definitions, the Froude number can be calculated as

$$\text{Fr} = \sqrt{\text{Pr} 2\varepsilon}. \quad (4.20)$$

All calculations assume a constant Prandtl number equal to 0.71. The viscosity and heat conductivity dependence on temperature is calculated using Equation (2.29). Our results are calculated and compared with those of the reference solution for $\hat{T}_{\text{ref}} = 600\text{K}$ and $\varepsilon = 0.6$. The non-dimensional length of the cavity is $L = 1$. The non-dimensional temperatures T_h and T_c are set to 1.6 and 0.4, respectively. Since the cavity contains a single species, it is governed by the equations for continuity, momentum and temperature (??–2.22c) and no equation for species transport is needed. Thus $n_s = 1$ and $Y_1 = 1$ in the whole domain. Moreover, the non-dimensional equation of state (Equation (2.26)) only depends on the temperature and reduces to

$$\rho = \frac{p_0}{T}. \quad (4.21)$$

The thermodynamic pressure p_0 in a closed system and has to be adapted in order to ensure mass conservation. If m_0 is the initial total mass of the system, the thermodynamic pressure is given by

$$p_0 = \frac{m_0}{\int_{\Omega} \frac{1}{T} dV}, \quad (4.22)$$

where Ω represents the complete closed domain. The initial mass of the system m_0 is constant and we set $m_0 = 1.0$. Within the solution algorithm, Equation (4.22) is used to update the value of the thermodynamic pressure after each Newton-Dogleg iteration. Moreover, the benchmark solution **vierendeelsBenchmarkSolutionsNatural2003** also reports the Nusselt number and thermodynamic pressure associated with a given Rayleigh number. The Nusselt number is defined for a given wall Γ in its averaged form as

$$\text{Nu}_{\Gamma} = \frac{1}{T_h - T_c} \int_{\Gamma} k \frac{\partial T}{\partial x} dy. \quad (4.23)$$

Rayleigh	p_0	$p_{0,\text{ref}}$	Nu_h	Nu_c	Nu_{ref}
10^2	0.9574	0.9573	0.9787	0.9787	0.9787
10^3	0.9381	0.9381	1.1077	1.1077	1.1077
10^4	0.9146	0.9146	2.2180	2.2174	2.2180
10^5	0.9220	0.9220	4.4801	4.4796	4.4800
10^6	0.9245	0.9245	8.6866	8.6791	8.6870
10^7	0.9225	0.9226	16.2411	16.1700	16.2400

Table 4.3: Comparison of calculated Nusselt numbers of the hot and cold wall and Thermodynamic pressure p_0 reported values **vierendeelsBenchmarkSolutionsNatural2003** for the differentially heated cavity. Results are obtained for polynomial degree of four for the velocities and temperature, three for the pressure in an equidistant 128×128 mesh.

Comparison of results with benchmark solution The benchmark results **vierendeelsBenchmarkSolutionsNatural2003** are presented for $\text{Ra} = \{10^2, 10^3, 10^4, 10^5, 10^6, 10^7\}$. In this range of Rayleigh numbers the problem has a steady-state solution, thus we are able to use our steady formulation of the problem. The cavity is represented by the domain $[0, 1] \times [0, 1]$. We use an equidistant Cartesian mesh with 30×30 elements for each simulation. A polynomial degree of five is used for the velocities and temperature, and a degree of four for the pressure. It is observed that for cases until $\text{Ra} = 10^5$ the solution of the system using Newton’s method is possible without further modifications, while for higher values the algorithm diverges. The homotopy strategy mentioned in Section 3.2 is used to overcome this problem and obtain solutions for higher Rayleigh (and equivalently higher Reynolds) numbers. Here, the Reynolds number is selected as the homotopy parameter and continuously increased until the desired value is reached. In Figures 4.11 to 4.13 temperature and velocity profiles for different Rayleigh numbers are shown. The profiles calculated with *BoSSS* agree closely to the benchmark solution. As expected we observe an increase of the acceleration of the fluid in the vicinity of the walls for increasing Rayleigh numbers, forming a thin boundary layer.

We also compare the thermodynamic pressure and the Nusselt numbers to the benchmark solution. The results are shown in Table 4.3. The thermodynamic pressure is obtained from Equation (4.22), and the Nusselt number is calculated with Equation (4.23). We observe that our results are in very good agreement with the reference results, and the thermodynamic pressure differ at most in the fourth decimal place. Note that the Nusselt number of the heated wall (Nu_h) and the Nusselt number of the cold wall (Nu_c) are different. As the Rayleigh number grows, this discrepancy becomes bigger, hinting that at such Rayleigh numbers the used mesh is not refined enough to represent adequately the thin boundary layer and more complex flow structures appearing at high-Rayleigh cases. While for an energy conservative system Nu_h and Nu_c should be equal, for our formulation this is not the case and the values differ slightly. This discrepancy can be seen as a measure of the discretization error from the DG formulation. **kleinHighorderDiscontinuousGalerkin2016** This hints that the discrepancy between Nusselt numbers should decrease when increasing the mesh resolution, which will be discussed in the next section.

Convergence study An h –convergence study of the differentially heated cavity configuration was conducted. Calculations were done for polynomial degrees $k = 1, 2, 3, 4$ and equidistant regular meshes with respectively 8, 16, 32, 64, 128 and 256 elements in each spatial coordinate.

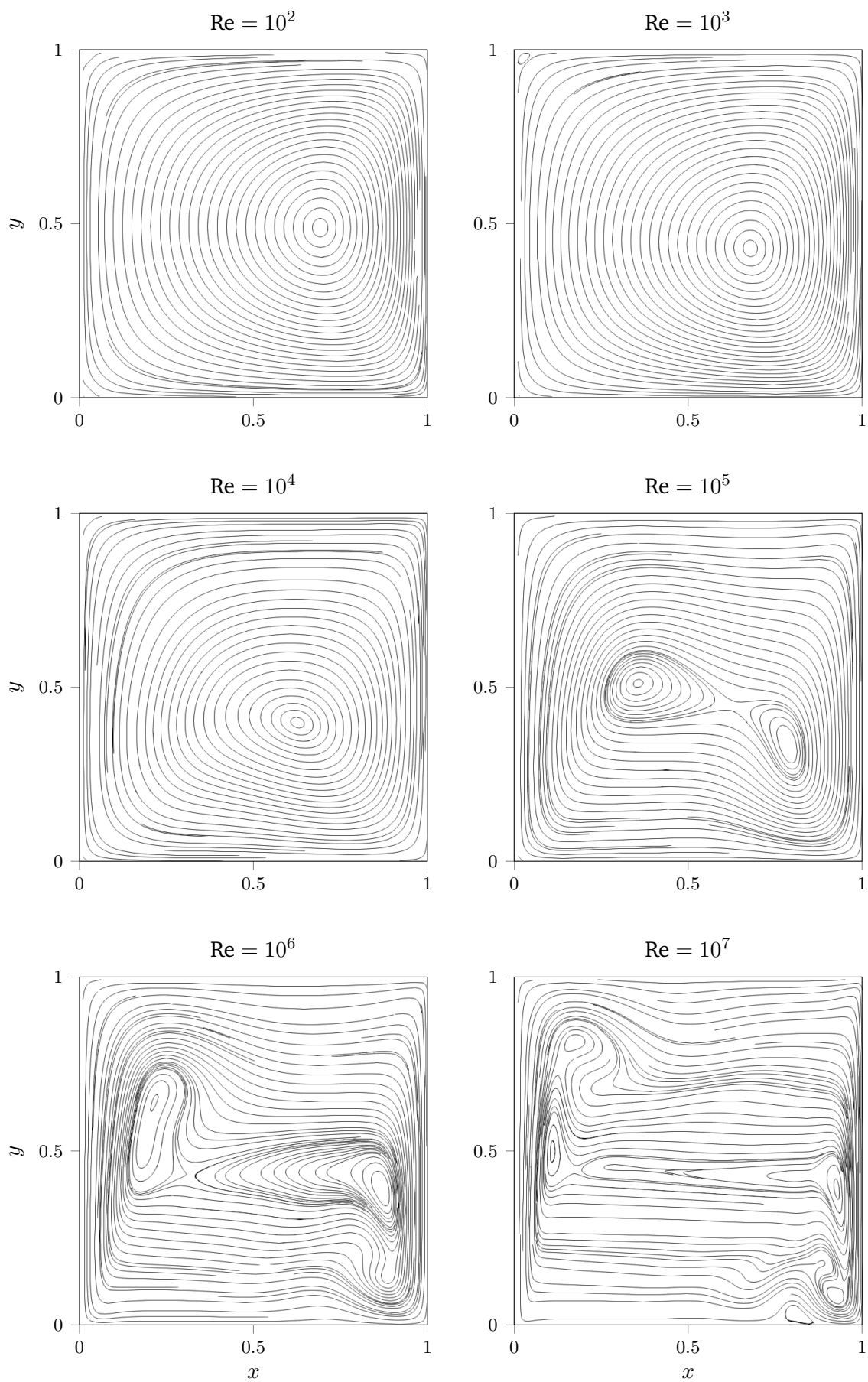


Figure 4.10: Streamlines of the heated cavity configuration with $\epsilon = 0.6$.

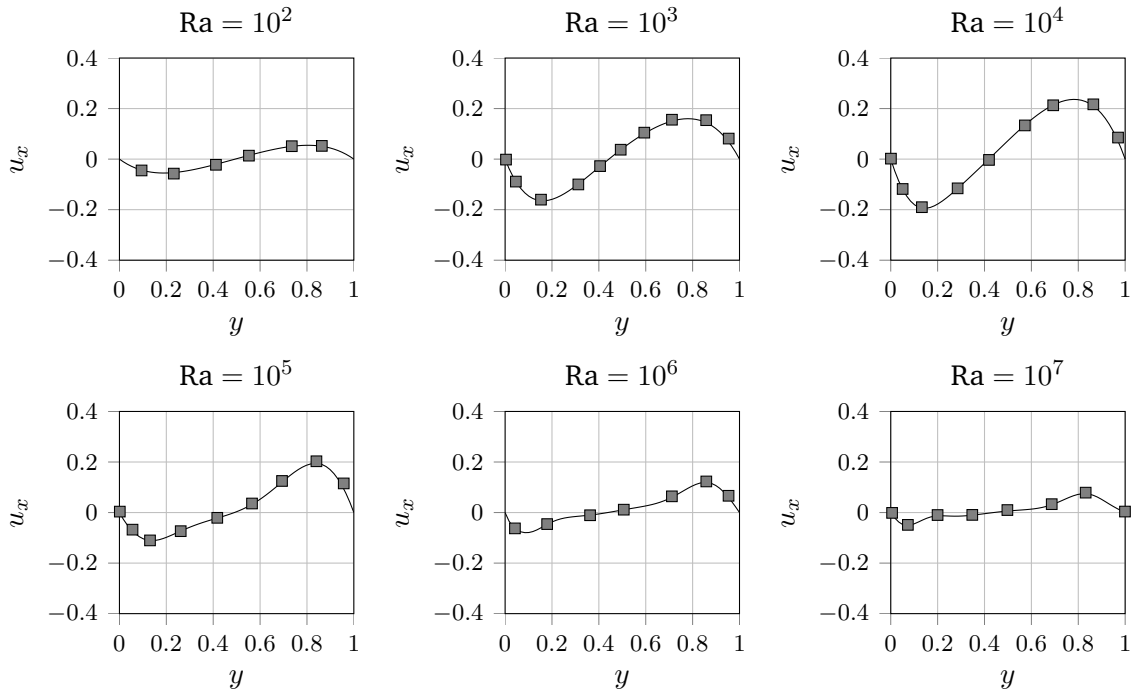


Figure 4.11: Profiles of the x-velocity component along the vertical line $x = 0.5$. Solid lines represents our solution and the marks the benchmark solution. **vierendeelsBenchmarkSolutionsNatural2003**

The L^2 -Norm was used for the calculation of the errors against the solution on the finest mesh. Results of the h -convergence study for varying polynomial orders k are shown in Figure 4.15. Recall that for increasing polynomial order, the expected order of convergence is given by the slope of the line curve when cell length and errors are presented in a log-log plot. Because we are using a mixed order formulation the slopes should be equal to k for the pressure and equal to $k + 1$ for all other variables. It is observed how convergence rates scale approximately as $k + 1$. Interestingly, for $k = 2$ the rates are higher than expected. On the other hand, some degeneration on the convergence rates is observed for $k = 4$.

As discussed in the last section, the difference on values of the Nusselt number on the hot wall Nu_h and the cold wall Nu_c is a consequence of spatial discretization error. In Figure 4.14 the convergence behaviour of the Nusselt number for different polynomial degrees k , different number of elements and for two different Ra numbers is presented. As expected, it can be observed that this discrepancy is smaller when a higher number of elements is used.

4.2.4 Poiseuille–Rayleigh–Bénard instability in a channel

Dies hier ist ein Blindtext zum Testen von Textausgaben. Wer diesen Text liest, ist selbst schuld. Der Text gibt lediglich den Grauwert der Schrift an. Ist das wirklich so? Ist es gleichgültig, ob ich schreibe: „Dies ist ein Blindtext“ oder „Huardest gefburn“? Kjift – mitnichten! Ein Blindtext bietet mir wichtige Informationen. An ihm messe ich die Lesbarkeit einer Schrift, ihre Anmutung, wie harmonisch die Figuren zueinander stehen und prüfe, wie breit oder schmal sie läuft. Ein Blindtext sollte möglichst viele verschiedene Buchstaben enthalten und in der Originalsprache gesetzt sein. Er muss keinen Sinn ergeben, sollte aber lesbar sein.

Fremdsprachige Texte wie „Lorem ipsum“ dienen nicht dem eigentlichen Zweck, da sie eine falsche Anmutung vermitteln. Dies hier ist ein Blindtext zum Testen von Textausgaben. Wer diesen Text liest, ist selbst schuld. Der Text gibt lediglich den Grauwert der Schrift an. Ist das wirklich so? Ist es gleichgültig, ob ich schreibe: „Dies ist ein Blindtext“ oder „Huardest gefburn“? Kjift – mitnichten! Ein Blindtext bietet mir wichtige Informationen. An ihm messe ich die Lesbarkeit einer Schrift, ihre Anmutung, wie harmonisch die Figuren zueinander stehen und prüfe, wie breit oder schmal sie läuft. Ein Blindtext sollte möglichst viele verschiedene Buchstaben enthalten und in der Originalsprache gesetzt sein. Er muss keinen Sinn ergeben, sollte aber lesbar sein. Fremdsprachige Texte wie „Lorem ipsum“ dienen nicht dem eigentlichen Zweck, da sie eine falsche Anmutung vermitteln. Dies hier ist ein Blindtext zum Testen von Textausgaben. Wer diesen Text liest, ist selbst schuld. Der Text gibt lediglich den Grauwert der Schrift an. Ist das wirklich so? Ist es gleichgültig, ob ich schreibe: „Dies ist ein Blindtext“ oder „Huardest gefburn“? Kjift – mitnichten! Ein Blindtext bietet mir wichtige Informationen. An ihm messe ich die Lesbarkeit einer Schrift, ihre Anmutung, wie harmonisch die Figuren zueinander stehen und prüfe, wie breit oder schmal sie läuft. Ein Blindtext sollte möglichst viele verschiedene Buchstaben enthalten und in der Originalsprache gesetzt sein. Er muss keinen Sinn ergeben, sollte aber lesbar sein. Fremdsprachige Texte wie „Lorem ipsum“ dienen nicht dem eigentlichen Zweck, da sie eine falsche Anmutung vermitteln. Dies hier ist ein Blindtext zum Testen von Textausgaben. Wer diesen Text liest, ist selbst schuld. Der Text gibt lediglich den Grauwert der Schrift an. Ist das wirklich so? Ist es gleichgültig, ob ich schreibe: „Dies ist ein Blindtext“ oder „Huardest gefburn“? Kjift – mitnichten! Ein Blindtext bietet mir wichtige Informationen. An ihm messe ich die Lesbarkeit einer Schrift, ihre Anmutung, wie harmonisch die Figuren zueinander stehen und prüfe, wie breit oder schmal sie läuft. Ein Blindtext sollte

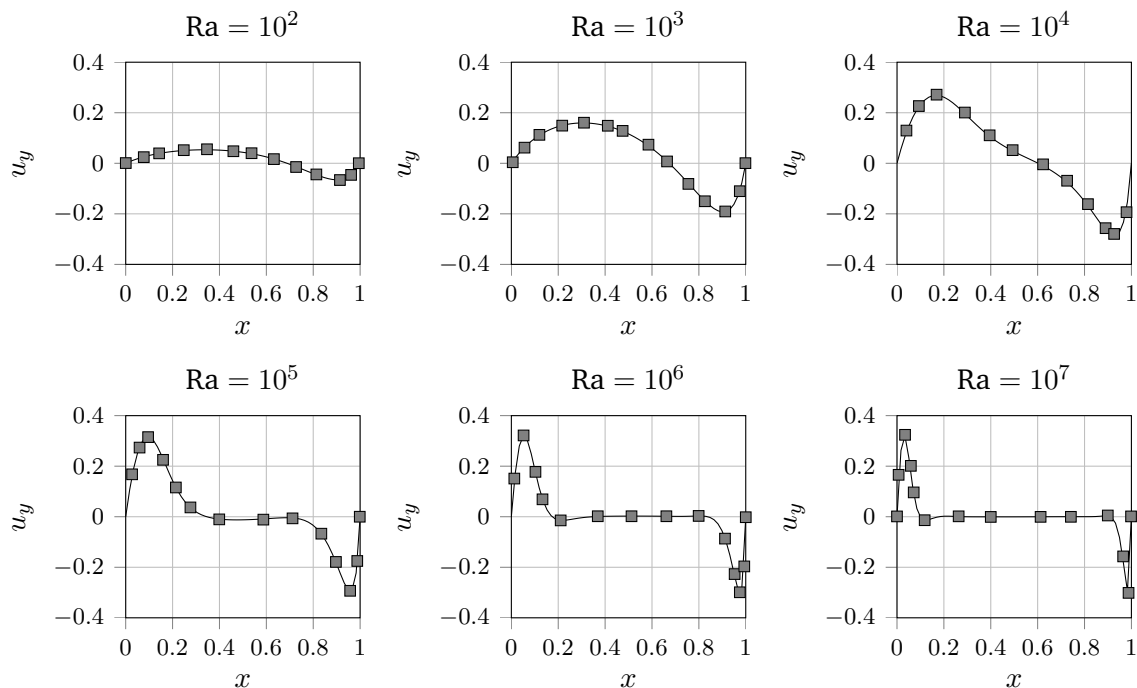


Figure 4.12: Profiles of the y-velocity component along the horizontal line $y = 0.5$. Solid lines represents our solution and marks the benchmark solution. vierendeelsBenchmarkSolutionsNatural2003

möglichst viele verschiedene Buchstaben enthalten und in der Originalsprache gesetzt sein. Er muss keinen Sinn ergeben, sollte aber lesbar sein. Fremdsprachige Texte wie „Lorem ipsum“ dienen nicht dem eigentlichen Zweck, da sie eine falsche Anmutung vermitteln. Dies hier ist ein Blindtext zum Testen von Textausgaben. Wer diesen Text liest, ist selbst schuld. Der Text gibt lediglich den Grauwert der Schrift an. Ist das wirklich so? Ist es gleichgültig, ob ich schreibe: „Dies ist ein Blindtext“ oder „Huardest gefburn“? Kjift – mitnichten! Ein Blindtext bietet mir wichtige Informationen. An ihm messe ich die Lesbarkeit einer Schrift, ihre Anmutung, wie harmonisch die Figuren zueinander stehen und prüfe, wie breit oder schmal sie läuft. Ein Blindtext sollte möglichst viele verschiedene Buchstaben enthalten und in der Originalsprache gesetzt sein. Er muss keinen Sinn ergeben, sollte aber lesbar sein. Fremdsprachige Texte wie „Lorem ipsum“ dienen nicht dem eigentlichen Zweck, da sie eine falsche Anmutung vermitteln.

4.2.5 Flow around a heated cylinder

Square cylinder

Dies hier ist ein Blindtext zum Testen von Textausgaben. Wer diesen Text liest, ist selbst schuld. Der Text gibt lediglich den Grauwert der Schrift an. Ist das wirklich so? Ist es gleichgültig, ob ich schreibe: „Dies ist ein Blindtext“ oder „Huardest gefburn“? Kjift – mitnichten! Ein Blindtext bietet mir wichtige Informationen. An ihm messe ich die Lesbarkeit einer Schrift, ihre Anmutung, wie harmonisch die Figuren zueinander stehen und prüfe, wie breit oder schmal sie läuft. Ein Blindtext sollte möglichst viele verschiedene Buchstaben enthalten und in der Originalsprache gesetzt sein. Er muss keinen Sinn ergeben, sollte aber lesbar sein. Fremdsprachige Texte wie „Lorem ipsum“ dienen nicht dem eigentlichen Zweck, da sie eine

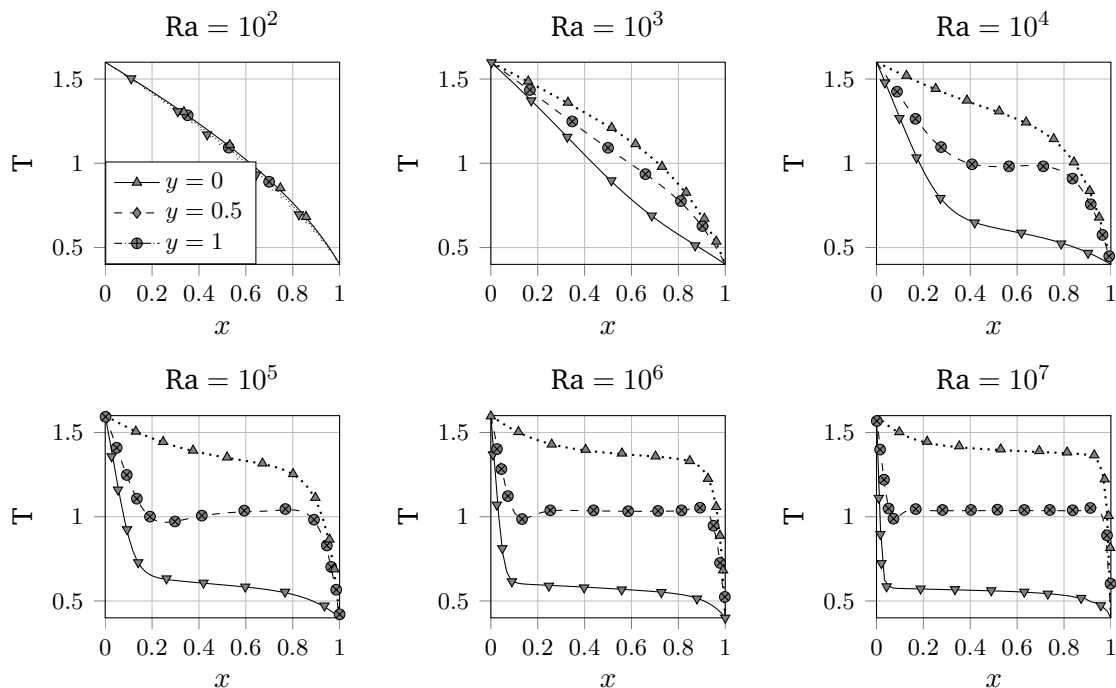


Figure 4.13: Temperature profiles for the differentially heated square cavity along different vertical levels. Solid lines represent our solution and marks the benchmark solution. [vierendeelsBenchmarkSolutionsNatural2003](#)

falsche Anmutung vermitteln. Dies hier ist ein Blindtext zum Testen von Textausgaben. Wer diesen Text liest, ist selbst schuld. Der Text gibt lediglich den Grauwert der Schrift an. Ist das wirklich so? Ist es gleichgültig, ob ich schreibe: „Dies ist ein Blindtext“ oder „Huardest gefburn“? Kjift – mitnichten! Ein Blindtext bietet mir wichtige Informationen. An ihm messe ich die Lesbarkeit einer Schrift, ihre Anmutung, wie harmonisch die Figuren zueinander stehen und prüfe, wie breit oder schmal sie läuft. Ein Blindtext sollte möglichst viele verschiedene Buchstaben enthalten und in der Originalsprache gesetzt sein. Er muss keinen Sinn ergeben, sollte aber lesbar sein. Fremdsprachige Texte wie „Lorem ipsum“ dienen nicht dem eigentlichen Zweck, da sie eine falsche Anmutung vermitteln. Dies hier ist ein Blindtext zum Testen von Textausgaben. Wer diesen Text liest, ist selbst schuld. Der Text gibt lediglich den Grauwert der Schrift an. Ist das wirklich so? Ist es gleichgültig, ob ich schreibe: „Dies ist ein Blindtext“ oder „Huardest gefburn“? Kjift – mitnichten! Ein Blindtext bietet mir wichtige Informationen. An ihm messe ich die Lesbarkeit einer Schrift, ihre Anmutung, wie harmonisch die Figuren zueinander stehen und prüfe, wie breit oder schmal sie läuft. Ein Blindtext sollte möglichst viele verschiedene Buchstaben enthalten und in der Originalsprache gesetzt sein. Er muss keinen Sinn ergeben, sollte aber lesbar sein. Fremdsprachige Texte wie „Lorem ipsum“ dienen nicht dem eigentlichen Zweck, da sie eine falsche Anmutung vermitteln. Dies hier ist ein Blindtext zum Testen von Textausgaben. Wer diesen Text liest, ist selbst schuld. Der Text gibt lediglich den Grauwert der Schrift an. Ist das wirklich so? Ist es gleichgültig, ob ich schreibe: „Dies ist ein Blindtext“ oder „Huardest gefburn“? Kjift – mitnichten! Ein Blindtext bietet mir wichtige

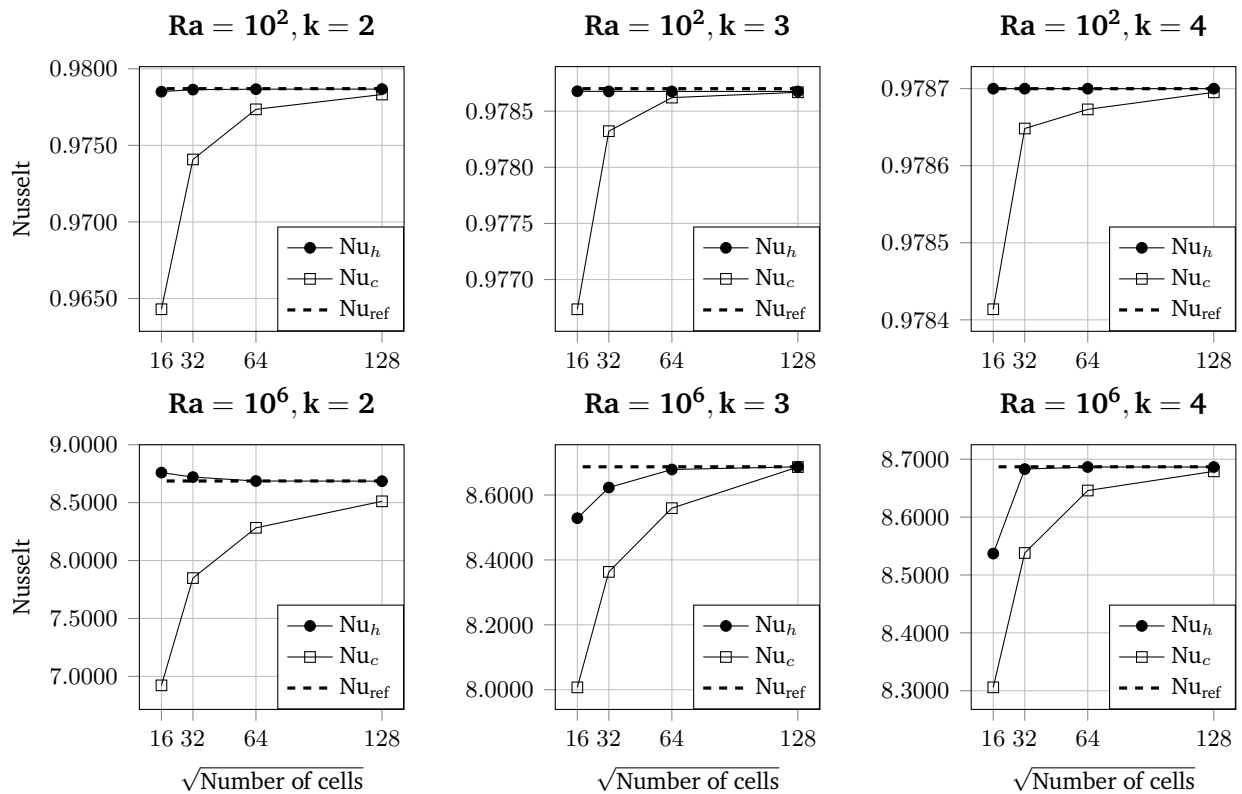


Figure 4.14: Nusselt numbers calculated with Equation (4.23) at the hot wall (Nu_h) and the cold wall (Nu_c) for different number of cells and polynomial order k . The reference values `vierendeelsBenchmarkSolutionsNatural2003` are shown with dashed lines.

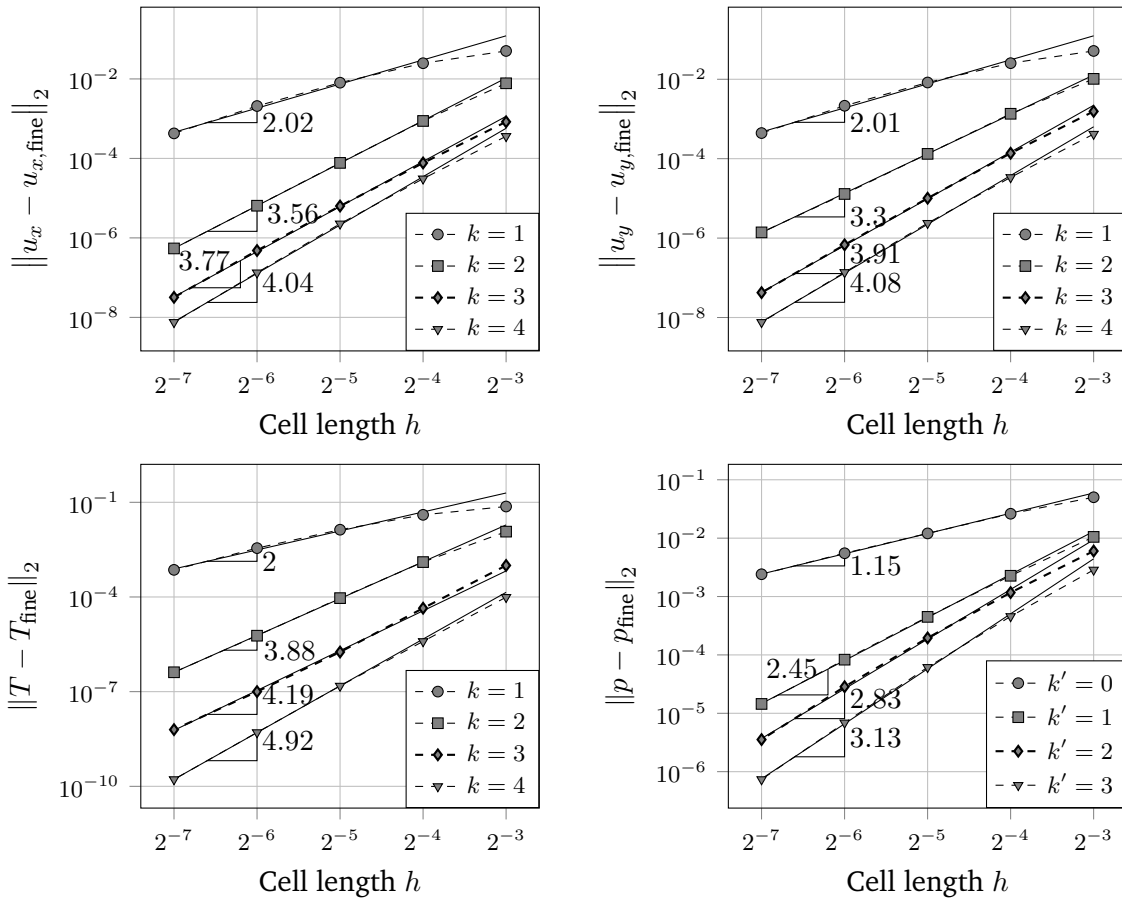


Figure 4.15: Convergence study of the differentially heated cavity problem for $Ra = 10^3$.

Informationen. An ihm messe ich die Lesbarkeit einer Schrift, ihre Anmutung, wie harmonisch die Figuren zueinander stehen und prüfe, wie breit oder schmal sie läuft. Ein Blindtext sollte möglichst viele verschiedene Buchstaben enthalten und in der Originalsprache gesetzt sein. Er muss keinen Sinn ergeben, sollte aber lesbar sein. Fremdsprachige Texte wie „Lorem ipsum“ dienen nicht dem eigentlichen Zweck, da sie eine falsche Anmutung vermitteln. Dies hier ist ein Blindtext zum Testen von Textausgaben. Wer diesen Text liest, ist selbst schuld. Der Text gibt lediglich den Grauwert der Schrift an. Ist das wirklich so? Ist es gleichgültig, ob ich schreibe: „Dies ist ein Blindtext“ oder „Huardest gefburn“? Kjift – mitnichten! Ein Blindtext bietet mir wichtige Informationen. An ihm messe ich die Lesbarkeit einer Schrift, ihre Anmutung, wie harmonisch die Figuren zueinander stehen und prüfe, wie breit oder schmal sie läuft. Ein Blindtext sollte möglichst viele verschiedene Buchstaben enthalten und in der Originalsprache gesetzt sein. Er muss keinen Sinn ergeben, sollte aber lesbar sein. Fremdsprachige Texte wie „Lorem ipsum“ dienen nicht dem eigentlichen Zweck, da sie eine falsche Anmutung vermitteln.

Circle? cylinder

Dies hier ist ein Blindtext zum Testen von Textausgaben. Wer diesen Text liest, ist selbst schuld. Der Text gibt lediglich den Grauwert der Schrift an. Ist das wirklich so? Ist es gleichgültig, ob ich schreibe: „Dies ist ein Blindtext“ oder „Huardest gefburn“? Kjift – mitnichten! Ein

Blindtext bietet mir wichtige Informationen. An ihm messe ich die Lesbarkeit einer Schrift, ihre Anmutung, wie harmonisch die Figuren zueinander stehen und prüfe, wie breit oder schmal sie läuft. Ein Blindtext sollte möglichst viele verschiedene Buchstaben enthalten und in der Originalsprache gesetzt sein. Er muss keinen Sinn ergeben, sollte aber lesbar sein. Fremdsprachige Texte wie „Lorem ipsum“ dienen nicht dem eigentlichen Zweck, da sie eine falsche Anmutung vermitteln. Dies hier ist ein Blindtext zum Testen von Textausgaben. Wer diesen Text liest, ist selbst schuld. Der Text gibt lediglich den Grauwert der Schrift an. Ist das wirklich so? Ist es gleichgültig, ob ich schreibe: „Dies ist ein Blindtext“ oder „Huardest gefburn“? Kjift – mitnichten! Ein Blindtext bietet mir wichtige Informationen. An ihm messe ich die Lesbarkeit einer Schrift, ihre Anmutung, wie harmonisch die Figuren zueinander stehen und prüfe, wie breit oder schmal sie läuft. Ein Blindtext sollte möglichst viele verschiedene Buchstaben enthalten und in der Originalsprache gesetzt sein. Er muss keinen Sinn ergeben, sollte aber lesbar sein. Fremdsprachige Texte wie „Lorem ipsum“ dienen nicht dem eigentlichen Zweck, da sie eine falsche Anmutung vermitteln. Dies hier ist ein Blindtext zum Testen von Textausgaben. Wer diesen Text liest, ist selbst schuld. Der Text gibt lediglich den Grauwert der Schrift an. Ist das wirklich so? Ist es gleichgültig, ob ich schreibe: „Dies ist ein Blindtext“ oder „Huardest gefburn“? Kjift – mitnichten! Ein Blindtext bietet mir wichtige Informationen. An ihm messe ich die Lesbarkeit einer Schrift, ihre Anmutung, wie harmonisch die Figuren zueinander stehen und prüfe, wie breit oder schmal sie läuft. Ein Blindtext sollte möglichst viele verschiedene Buchstaben enthalten und in der Originalsprache gesetzt sein. Er muss keinen Sinn ergeben, sollte aber lesbar sein. Fremdsprachige Texte wie „Lorem ipsum“ dienen nicht dem eigentlichen Zweck, da sie eine falsche Anmutung vermitteln. Dies hier ist ein Blindtext zum Testen von Textausgaben. Wer diesen Text liest, ist selbst schuld. Der Text gibt lediglich den Grauwert der Schrift an. Ist das wirklich so? Ist es gleichgültig, ob ich schreibe: „Dies ist ein Blindtext“ oder „Huardest gefburn“? Kjift – mitnichten! Ein Blindtext bietet mir wichtige Informationen. An ihm messe ich die Lesbarkeit einer Schrift, ihre Anmutung, wie harmonisch die Figuren zueinander stehen und prüfe, wie breit oder schmal sie läuft. Ein Blindtext sollte möglichst viele verschiedene Buchstaben enthalten und in der Originalsprache gesetzt sein. Er muss keinen Sinn ergeben, sollte aber lesbar sein. Fremdsprachige Texte wie „Lorem ipsum“ dienen nicht dem eigentlichen Zweck, da sie eine falsche Anmutung vermitteln. Dies hier ist ein Blindtext zum Testen von Textausgaben. Wer diesen Text liest, ist selbst schuld. Der Text gibt lediglich den Grauwert der Schrift an. Ist das wirklich so? Ist es gleichgültig, ob ich schreibe: „Dies ist ein Blindtext“ oder „Huardest gefburn“? Kjift – mitnichten! Ein Blindtext bietet mir wichtige Informationen. An ihm messe ich die Lesbarkeit einer Schrift, ihre Anmutung, wie harmonisch die Figuren zueinander stehen und prüfe, wie breit oder schmal sie läuft. Ein Blindtext sollte möglichst viele verschiedene Buchstaben enthalten und in der Originalsprache gesetzt sein. Er muss keinen Sinn ergeben, sollte aber lesbar sein. Fremdsprachige Texte wie „Lorem ipsum“ dienen nicht dem eigentlichen Zweck, da sie eine falsche Anmutung vermitteln.

4.3 Multi-component non-isothermal cases

In the following, we show results of the simulations of two test cases with combustion, namely the counterflow diffusion flame and the chambered diffusion flame. For both cases, the solution of the flame sheet problem described in ?? is calculated first. This solution is used subsequently as initial estimates for the solution of the finite chemistry rate problem (c.f. Section 2.1.2). In all test cases presented in this section, a smoothing parameter $\sigma = 50$ was used (c.f. ??). For all test cases methane combustion according to the one-step model shown in ?? is considered.

The mass fraction transport Equation (2.22d) is solved for the species CH_4 , O_2 , CO_2 and H_2O , thus $\mathbf{Y}' = (Y_{\text{CH}_4}, Y_{\text{O}_2}, Y_{\text{CO}_2}, Y_{\text{H}_2\text{O}})$. The nitrogen mass fraction Y_{N_2} is calculated according to Equation (2.23).

4.3.1 CoFlowing flame?

As a first test for assessing basic behaviour related to combustion, a coflowing flame configuration is used. This test case is the main prototype flame for diffusion regimes **poinotTheoreticalNumericalCombustion**. It is set up by sending a stream of fuel against a stream containing oxidizer. A diagram can be seen in X

The area where the chemical reaction takes place is usually a thin region, which thickness is defined by the availability of reactants, which at the same time are controlled by the velocity which the chemical reaction happens. This factor is governed by the Da number in the non-dimensional formulation (sure??). It is of critical importance for the numerical simulation that the flame is resolved accordingly, which can demand a very fine mesh. Not doing so can provoke non-physically effects to occur, as for example negative values of the reaction term ω (in the present formulation the reaction is irreversible, and thus only positive values of ω make sense).

For avoiding over-resolving in zones where actually no reaction is taking place (or very slowly), an adaptive mesh refinement strategy (see section X) within a pseudo-time-stepping framework was used. Here a suitable strategy for choosing cells to be refined is necessary. For reactive flows, this strategy is based on the variable ω . Before each refinement step the values of ω are normalized by the biggest value of the domain, and according to this normalized effects the cells are refined.

4.3.2 Counterflow diffusion flame

The counterflow diffusion flame is a canonical configuration used to study the structure of non-premixed flames. In its most basic configuration it consists of two oppositely situated jets. The fuel (possibly mixed with some inert component such as nitrogen) is fed into the system by one of the jets, while the other jet feeds air to the system, thereby establishing a stagnation point flow. Upon contact, the reactants produce a flame which is located in the vicinity of the stagnation plane. A diagram of the setup can be seen in Figure 4.17. This simple configuration has been subject of study for decades because it provides a simple way of creating a strained diffusion flame, which proves to be useful when studying the flame structure, extinction limits or production of pollutants of flames **pandyaStructureFlatCounterFlow1964 spaldingTheoryMixingChemical1961 keyesFlameSheetStarting1987**. By assuming an infinite injector diameter and self-similarity of the solution, it is possible to reduce the governing equations to a one-dimensional formulation (see e.g. the textbook of Kee **keeChemicallyReactingFlow2003**). As a means of validating our implementation we compare the results with the solution of the one-dimensional self-similar problem calculated with BVP4, a fourth order finite difference boundary value problem solver provided by MATLAB.

The combustion of a methane-nitrogen mixture with air was simulated using the *BoSSS* code. The mass composition of the fuel inlet was assumed to be $Y_{\text{CH}_4}^0 = 0.2$ and $Y_{\text{N}_2}^0 = 0.8$, and the oxidizer inlet corresponds to air with $Y_{\text{O}_2}^0 = 0.23$ and $Y_{\text{N}_2}^0 = 0.77$. Because we are dealing with an open system, the thermodynamic pressure \hat{p}_0 is constant and set to the ambient pressure of 101 325 Pa. As noted by Sung et al., **sungStructuralResponseCounterflow1995** although the

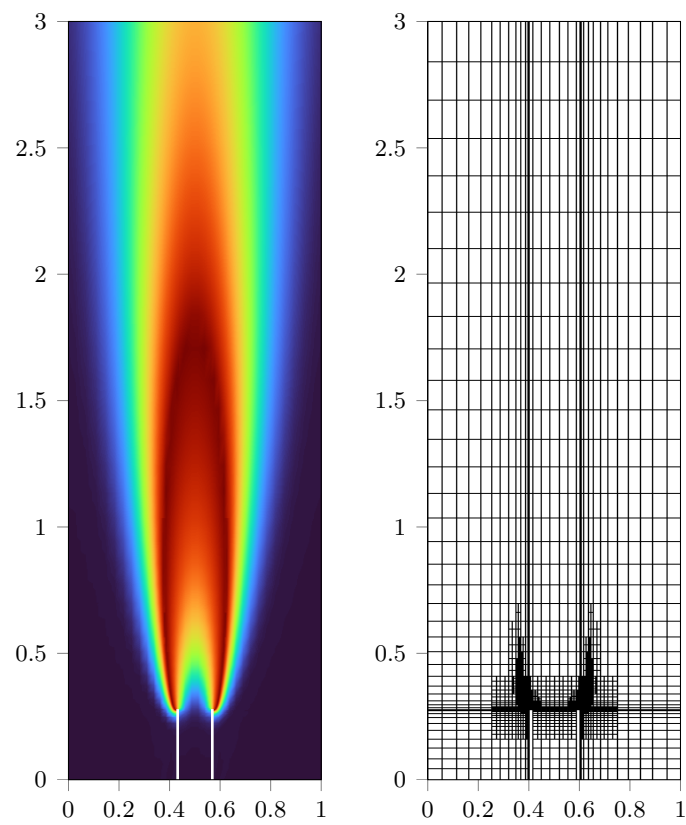


Figure 4.16: Coflowing Flame.

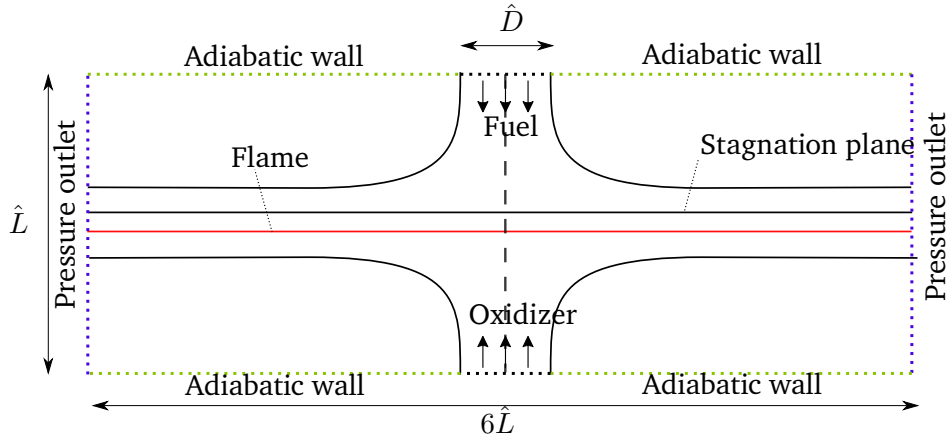


Figure 4.17: Schematic representation of the counterflow configuration.

form of the inlet velocity profiles does have an influence on the solution of the problem, its effect on the solution near the flame zone is rather small. Nevertheless, as mentioned before the solution of the self-similar one-dimensional problem assumed an infinite injector diameter, which implies that the upstream velocity field has to be constant. Based on this fact we set the velocity profile of both inlets as a plug flow. Following combinations of inlet velocities were calculated:

- Low inlet velocities: $u_{\text{fuel}}^0 = 0.048 \text{ m s}^{-1}$ and $u_{\text{oxidizer}}^0 = 0.144 \text{ m s}^{-1}$,
- Medium inlet velocities: $u_{\text{fuel}}^0 = 0.12 \text{ m s}^{-1}$ and $u_{\text{oxidizer}}^0 = 0.36 \text{ m s}^{-1}$
- High inlet velocities: $u_{\text{fuel}}^0 = 0.24 \text{ m s}^{-1}$ and $u_{\text{oxidizer}}^0 = 0.72 \text{ m s}^{-1}$

By using as definition of the strain rate the maximum axial velocity gradient, the calculated strains for the three cases mentioned above are 34 s^{-1} , 76 s^{-1} and 155 s^{-1} , respectively. The temperature of both inlets is 300 K . The separation between both jets \hat{L} is equal to 0.02 m , and the length of the inlet opening \hat{D} is 0.02 m . The left and right domain boundaries are selected to be at a distance $3\hat{L}$ of the center. A non-unity but constant Lewis number formulation is used, with $\text{Le}_{\text{CH}_4} = 0.97$, $\text{Le}_{\text{O}_2} = 1.11$, $\text{Le}_{\text{H}_2\text{O}} = 0.83$ and $\text{Le}_{\text{CO}_2} = 1.39$. **smookePremixedNonpremixedTest1991** The heat capacity of each component is evaluated locally from NASA polynomials, and the mixture heat capacity is calculated with Equation (2.28).

In Figure 4.18 the convergence history obtained for a typical calculation of the counter diffusion flame is presented. The solution of the flame sheet calculation requires 17 iterations until convergence is reached. The obtained solution is used as a starting value for the finite chemical rate calculation, which only needs 10 iterations until convergence is reached. We note that because the flame sheet calculation is only used as an approximation of the final solution, a low polynomial degree can be used. For the flame sheet calculation $k = 2$ was chosen, resulting in a rather small system with 26,880 degrees of freedom. For the finite rate calculation $k = 4$ was used, which resulted in a system with 174,110 degrees of freedom. With the above-mentioned another advantage of the approach of using the flame sheet calculation for two-dimensional simulations can be highlighted. The initial estimate can be found relatively easily for a system with few degrees of freedom. Using the solution found as the initial estimate has the consequence that Newton's algorithm for the complete problem (which has many more degrees of freedom) only needs a few iterations to find a solution.

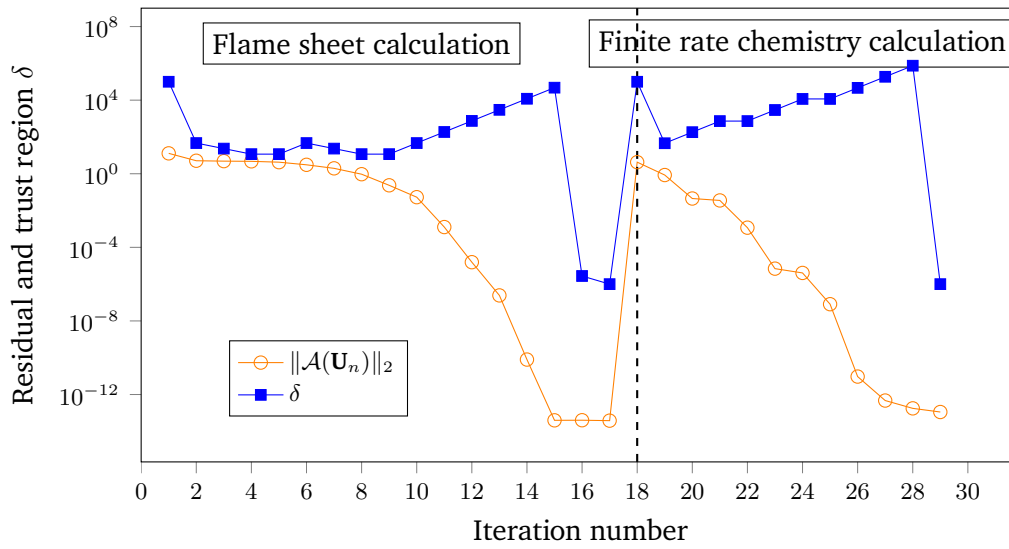


Figure 4.18: Convergence history of the diffusion flame in the counterflow configuration, with a maximum strain value of 165.1s^{-1}

Because we are solving a two-dimensional configuration, in order to be able to compare our results with the ones obtained from the one-dimensional representation, the temperature, mass fractions and velocity profiles are extracted along the centerline of the system shown as the dashed line in Figure 4.17. In Figure 4.19 a comparison of the axial velocities calculated with *BoSSS* and the one-dimensional solution is shown. While for the high strain case the results agree closely, for lower strains a discrepancy is observed. Recall that the derivation of the one-dimensional approximation assumes a constant velocity field incoming to the flame zone in order to obtain a self-similar solution. In the case of the two-dimensional configuration presented here, the border effects do have an influence on the centerline, which disrupts the self-similarity. This effect is more pronounced for low velocities, which explains the discrepancy between curves. Similarly, In Figure 4.20 the temperature and mass fraction fields are presented. Again, a discrepancy is observed for low strains, but results show a good agreement for higher inlet velocities. It can also be observed how, as expected, **fernandez-tarrazoSimpleOnestepChemistry2006** at higher strains a significant penetration (leakage) of oxygen across the flame is present. Finally, in Figure 4.21 the two-dimensional temperature, velocity and reaction rate fields for the case (a) are shown. We note that the solution of this configuration showed singularities in the boundary points where the inlet and wall meet. This fact made hard to realize an *h*-convergence study for the complete domain. Based on this we decided to analyze a flame configuration that does not exhibit this behaviour, as shown in the next section.

4.3.3 Chambered diffusion flame

The chambered diffusion flame configuration has served as a model for many theoretical studies related to diffusion flames **matalonEffectThermalExpansion2010**; **rameauNumericalBifurcationChambered1** **matalonDiffusionFlamesChamber1980** A scheme of the configuration can be seen in Figure 4.22. Fuel is injected at a constant rate into the bottom of a small insulated chamber, while oxidant diffuses into the system against the direction of flow. Constant conditions at the outlet

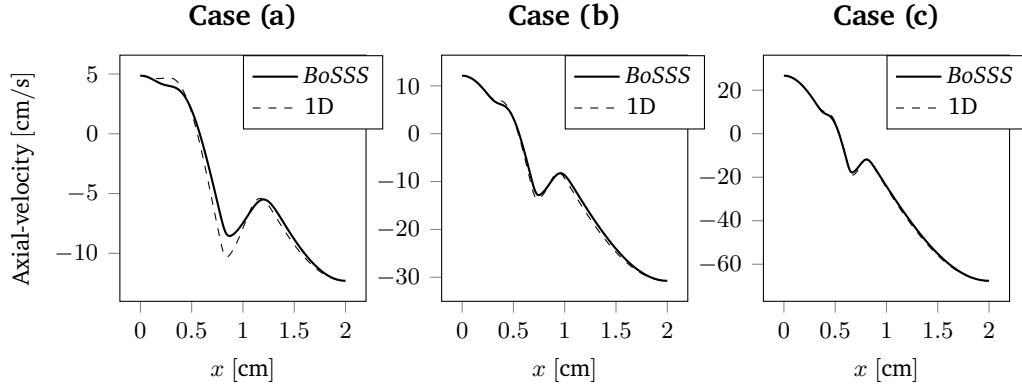


Figure 4.19: Comparison of the axial velocity calculated with BoSSS and the one-dimensional approximation.

of the chamber are achieved by a rapid renewal of the flow of oxidant. Under these conditions a planar flame forms far away from the walls, which allows a one-dimensional description of the flame structure. The fuel inlet into the chamber is modelled with a velocity inlet boundary condition Equation (2.36a), while the flow outlet at the top is considered an outlet as given by Equation (2.36d). Since we are interested in the flame in wall distance, it is sufficient to set the remaining boundary conditions as periodic boundaries. This effectively transforms the problem into a pseudo two-dimensional configuration.

In this test case we study the combustion of a $\text{CH}_4\text{-N}_2$ mixture with air. The thermodynamic pressure \hat{p}_0 is set equal to an ambient pressure of 101 325 Pa. The inlet velocity of the fuel jet is set to 0.025 m s^{-1} and its mass composition is $Y_{\text{CH}_4}^0 = 0.2$ and $Y_{\text{N}_2}^0 = 0.8$ while air has a composition $Y_{\text{O}_2}^0 = 0.23$ and $Y_{\text{N}_2}^0 = 0.77$. The temperature of the fuel and air feed streams is 300 K. The length of the system L is equal to 0.015 m. For this configuration an h -convergence study is conducted, where uniform Cartesian meshes with 5×2^6 , 5×2^7 , 5×2^8 , 5×2^9 and 5×2^{10} cells are used. The polynomial degrees are varied from 1 to 4 for velocity, temperature and mass fractions, and from 0 to 3 for pressure. Errors are calculated using the finest mesh as a reference solution. The results are shown in Figure 4.23 for variables u_x , T , Y_{CH_4} and p . The convergence results for other variables are similar and not shown here. We observe the expected slope increase with increasing polynomial degrees. For low polynomial degrees the orders of convergence are very close to the theoretical values. However for higher polynomial degrees we observe a slight deterioration of the convergence rate.

4.4 Conclusions

In the present work we have shown the discretization using the DG method for the reactive low-Mach equations. A mixed order formulation has been used, where velocity, temperature and mass fractions are represented by polynomials of degree k , and pressure by polynomials of degree $k - 1$. The system obtained from the discretization was solved by means of a Newton-Dogleg type method. Additionally, a homotopy strategy for solving highly nonlinear systems was introduced and used for some of the presented test cases. For the reactive test cases the concept of the flame sheet estimate was demonstrated to be a useful and computationally cheap way of initializing the finite reaction rate combustion calculations. The solver was used to calculate three different benchmark configurations, one without combustion and two cases with combus-

tion. The first of these is the differentially heated cavity. This benchmark case was solved for varying Rayleigh numbers, spanning from $Ra = 10^2$ to $Ra = 10^7$. It was observed that for cases with Rayleigh number larger than 10^5 the use of our homotopy strategy was necessary to ensure convergence. Velocity and temperature profiles as well as thermodynamic pressure and Nusselt number were compared with a reference solution, obtaining very satisfactory results, thus validating our implementation of the method for variable density systems. An h -convergence study was presented for the differentially heated cavity, obtaining the expected convergence rates up to $k = 4$, where some degeneration on the rates was observed. Furthermore the counterflow diffusion flame configuration was analyzed, with which we intended to test the implemented chemistry model in conjunction with our solver. The results obtained with *BoSSS* were compared with results obtained by solving the self-similar one-dimensional representation of the counter diffusion flame configuration for varying strain rates. While for low strains some discrepancies between results were observed, the difference narrowed for high strains, which can be explained by the influence of the border effects on the centerline results for a two-dimensional

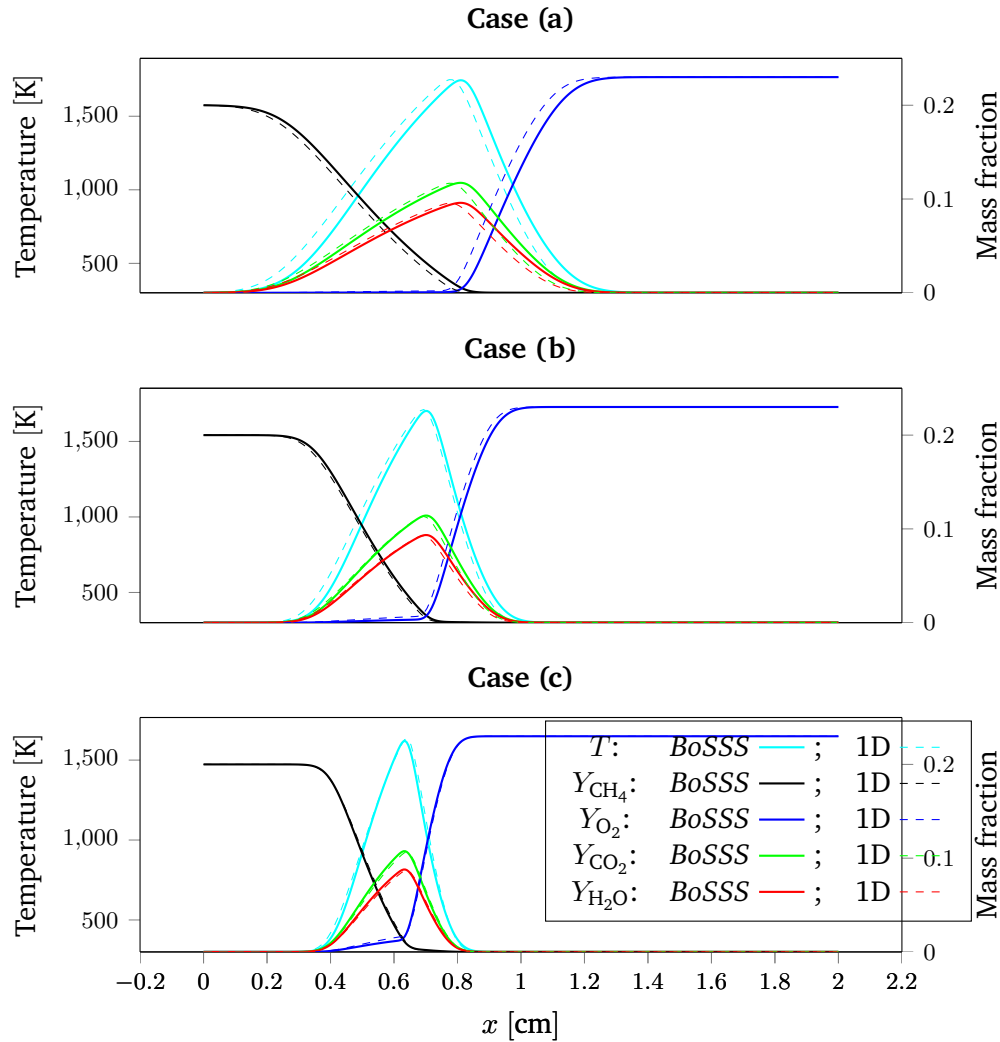


Figure 4.20: Comparison of temperature and mass fraction fields obtained with *BoSSS* and the one-dimensional approximation.

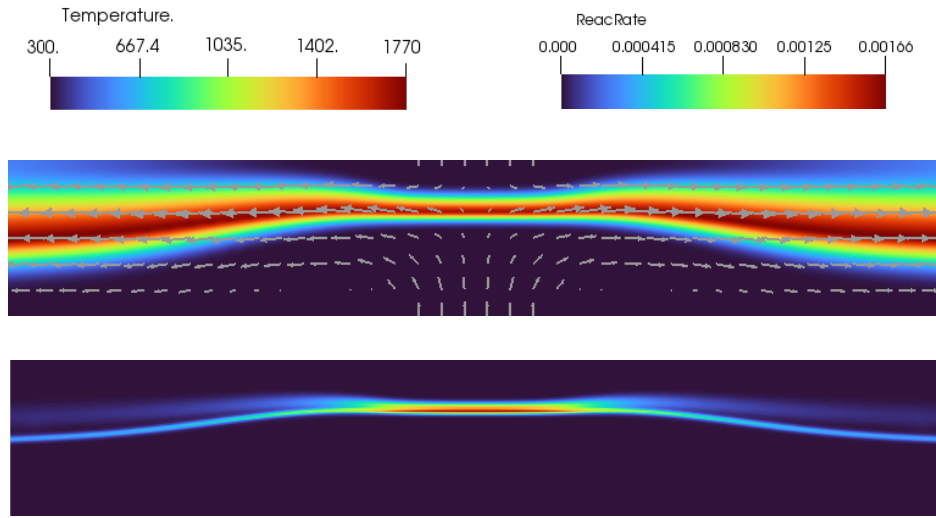


Figure 4.21: Calculated temperature and velocity fields (top picture) and reaction rate (second picture) of the counter diffusion flame configuration, case (a). The unit of the temperature is K and of the reaction rate $\text{kmol m}^{-3} \text{s}^{-1}$.

configuration. Finally, the chambered diffusion flame configuration was used to study the convergence rates of our method. It was shown that, as expected, the convergence rates increase when using higher degree polynomials, but with some deterioration compared to the theoretical expected convergence. In future work the implemented solver is intended to be used in conjunction with our extended-DG solver [kummerExtendedDiscontinuousGalerkin2017](#); [kummerBoSSSPackageMultigrid2021](#); [krauseIncompressibleImmersedBoundary2017](#) in order to study multiphase reactive systems such as droplets.

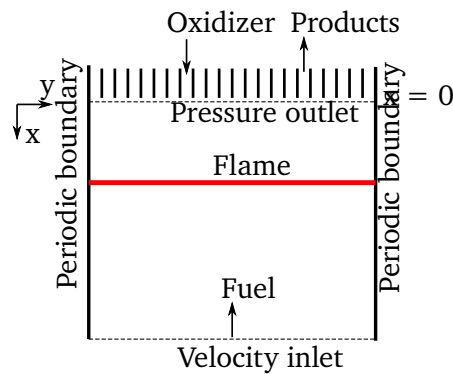


Figure 4.22: Schematic representation of the chambered diffusion flame configuration.

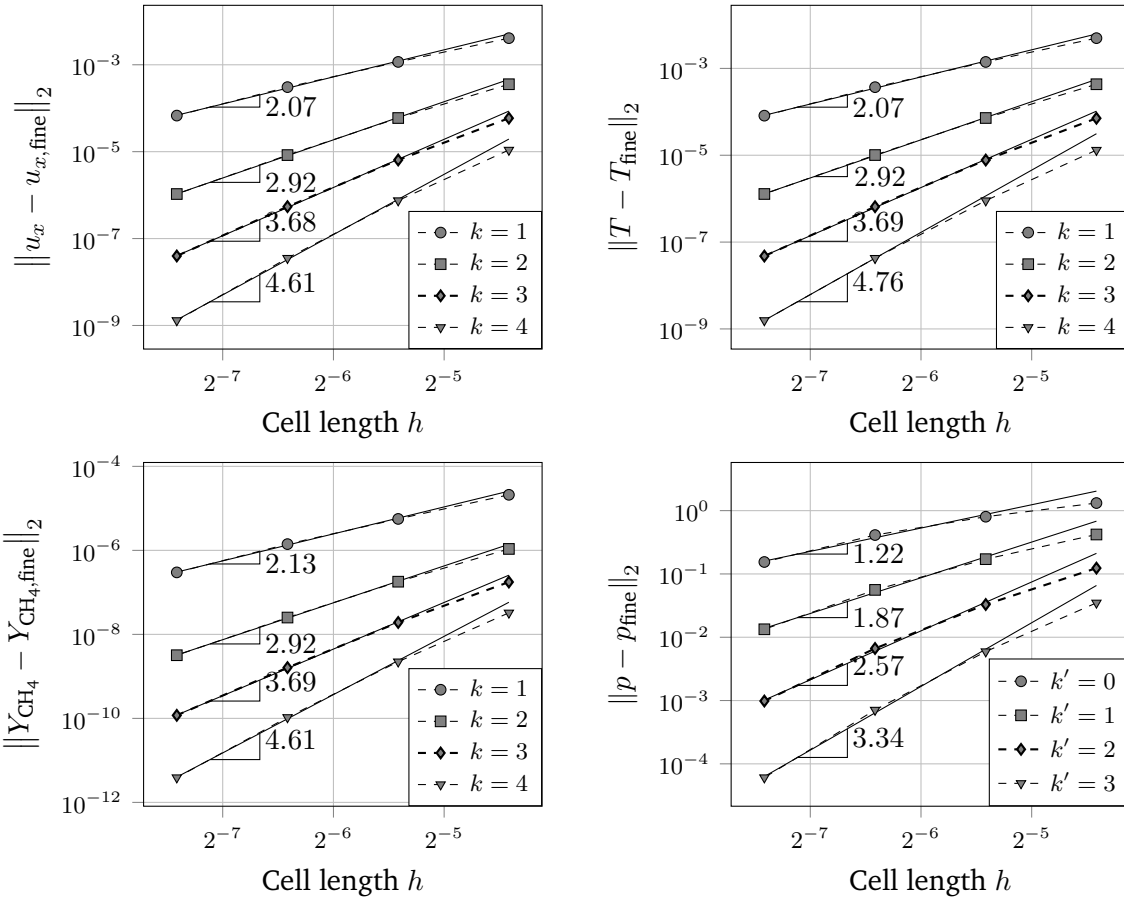


Figure 4.23: Convergence study for the chambered diffusion flame configuration.

5 Conclusion

lalala25

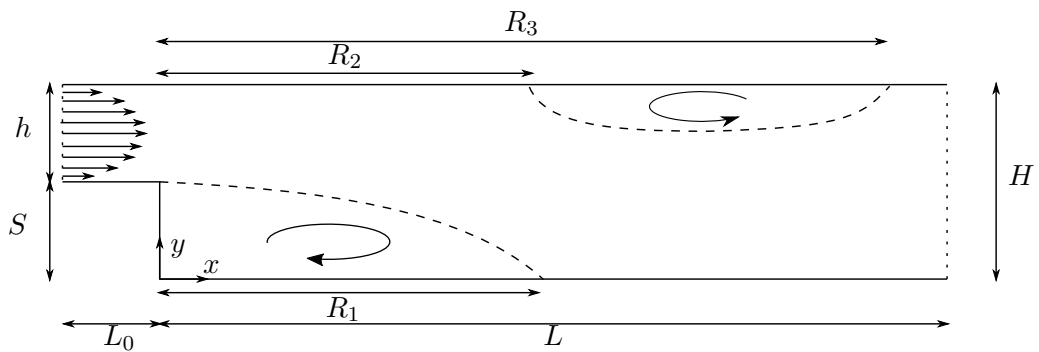


Figure 5.1: Schematic representation of the backward-facing step. Both primary and secondary vortices are shown. Sketch is not to scale.

Curriculum vitae

Vor- und Nachname

Persönliche Daten

Geburtsdatum: -
Geburtsort: -
Staatsangehörigkeit: -

Schulbildung

Jahr - Jahr -
Jahr - Jahr -

Studium

Jahr - Jahr -

**Wissenschaftliche
Tätigkeit**

Jahr - Jahr Wissenschaftlicher Mitarbeiter am Fachgebiet für Strömungs-
dynamik im Fachbereich Maschinenbau der TU Darmstadt,
Promotion und Lehrtätigkeit